AWARD NUMBER: W81XWH-15-1-0068

TITLE: Targeting Transcription Elongation Machinery for Breast Cancer Therapy

PRINCIPAL INVESTIGATOR: Kunxin Luo

CONTRACTING ORGANIZATION: University of California, Berkeley

REPORT DATE: July 2020

TYPE OF REPORT: Final technical Report

PREPARED FOR: U.S. Army Medical Research and Materiel Command
Fort Detrick, Maryland 21702-5012

REPORT DOCUMENTATION PAGE

Form Approved
OMB No. 0704-0188

1. REPORT DATE	2. REPORT TYPE	3. DATES COVERED
July 2020	Final Report	15APR2015 - 14APR2020

4. TITLE AND SUBTITLE
Targeting Transcription Elongation Machinery for Breast Cancer Therapy

5a. CONTRACT NUMBER

5b. GRANT NUMBER
W81XWH-15-1-0068

5c. PROGRAM ELEMENT NUMBER

6. AUTHOR(S)
Kunxin Luo

E-Mail: kluo@berkeley.edu

5d. PROJECT NUMBER

5e. TASK NUMBER

5f. WORK UNIT NUMBER

7. PERFORMING ORGANIZATION NAME(S) AND ADDRESS(ES)
University of California, Berkeley 41 Koshland

8. PERFORMING ORGANIZATION REPORT NUMBER

9. SPONSORING / MONITORING AGENCY NAME(S) AND ADDRESS(ES)
U.S. Army Medical Research and Materiel Command
Fort Detrick, Maryland 21702-5012

10. SPONSOR/MONITOR'S ACRONYM(S)
USAMRMC

11. SPONSOR/MONITOR'S REPORT NUMBER(S)

12. DISTRIBUTION / AVAILABILITY STATEMENT
Approved for Public Release; Distribution Unlimited

13. SUPPLEMENTARY NOTES

14. ABSTRACT:

This project focuses on the important but under-studied role of the P-TEFb-dependent transcription elongation machinery in human breast cancer progression. Our goal is to test the hypothesis that transcription elongation is a key regulatory step in breast cancer development, and that targeting P-TEFb can be an effective strategy to block breast cancer progression. The positive transcription elongation factor b (P-TEFb), composed of CDK9 and cyclin T, stimulates transcriptional elongation by RNA polymerase (Pol) II and regulates cell growth and differentiation. Recently, we demonstrated that P-TEFb also controls the expression of EMT regulators to promote breast cancer progression. In the nucleus, more than half of P-TEFb are sequestered in the inactive state 7SK snRNP complex. Our study supported by this grant shows that the assembly of the 7SK snRNP is preceded by an intermediate complex between HEXIM1 and P-TEFb that allows transfer of the kinase active P-TEFb from Hsp90 to 7SK snRNP for its suppression. Downregulation of HEXIM1 locks P-TEFb in the Hsp90 complex, keeping it in the active state to enhance breast cancer progression, but also rendering the cells highly sensitive to Hsp90 inhibition. Since HEXIM1 is often downregulated in human triple negative breast cancer (TNBC), these cells are particularly sensitive to Hsp90 inhibition. Our study provides a mechanistic explanation for the increased sensitivity of TNBC to Hsp90 inhibition and therefore may provide a novel anti-cancer strategy for triple negative breast cancer.

15. SUBJECT TERMS: NONE LISTED

16. SECURITY CLASSIFICATION OF:			17. LIMITATION OF ABSTRACT	18. NUMBER OF PAGES	19a. NAME OF RESPONSIBLE PERSON
a. REPORT	b. ABSTRACT	c. THIS PAGE			USAMRMC
Unclassified	Unclassified	Unclassified	Unclassified	18	19b. TELEPHONE NUMBER *(include area code)*

Standard Form 298 (Rev. 8-98)
Prescribed by ANSI Std. Z39.18

Table of Contents

1. INTRODUCTION:

Aberrant gene expression, caused by mutations in various signaling pathways, lie in the heart of breast cancer development and progression. Mammalian gene expression is controlled primarily at the level of transcription, which consists of several closely interlinked stages. During the past 30 years, the transcription field has been pre-occupied with the pre-initiation and initiation stages of transcription and ignored the subsequent elongation step, which in recent years has been shown to be extremely critical for the control of cell growth, embryonic development, as well as stem cell self-renewal and differentiation. This proposal focuses on the important but under-studied role of the transcription elongation machinery in human breast cancer progression and is designed to test the hypotheses that a network of P-TEFb-containing elongation complexes plays a key role in regulating breast cancer EMT, stemness, invasion and metastasis through controlling the expression of essential EMT and metastasis regulators, and that targeting P-TEFb is a viable therapeutic approach to halt breast cancer progression.

At the core of the elongation machinery is the CDK9 and cyclin T1 heterodimer termed P-TEFb that stimulates the transition of RNA Pol II from promoter-proximal pausing to productive elongation by phosphorylating Pol II and antagonizing negative elongation factors. In mammalian cells, P-TEFb is maintained in a functional equilibrium between the active and inactive states through reversible associations with distinct regulators that collectively form a network of P-TEFb complexes. Under normal growth conditions, more than half of nuclear P-TEFb are sequestered in a kinase-inactive complex called the 7SK snRNP that contains the 7SK snRNA as a structural scaffold, HEXIM1 as the kinase inhibitor, and LARP7 and MePCE as proteins that bind to and maintain the stability of 7SK snRNA. The 7SK snRNP represents the principle cellular reservoir of uncommitted P-TEFb and responds to demands for increased transcription and cell proliferation by releasing P-TEFb, which can subsequently be recruited by Brd4 to chromatin templates or integrated into the Super Elongation Complex (SEC) for transcriptional activation. The bromodomain protein Brd4 recruits P-TEFb to chromatin templates through interacting with acetylated histones and the mediator complex and is required for transcription of many primary response and signal-induced genes. In addition to P-TEFb, the SEC contains mostly fusion partners (e.g. AFF1, AFF4, ELL1, ELL2, ENL and AF9) of the mixed lineage leukemia (MLL) protein and promotes transcription of MLL-target genes, leading to some of the most severe forms of leukemia. Our working hypotheses is that P-TEFb activation as a result of shifting its functional equilibrium to the active side is a major driving force to promote breast cancer EMT, stemness and metastasis, and that the interference of this activation halts cancer progression and can thus be an effective therapy.

2. KEYWORDS:

Transcriptional elongation, P-TEFb, breast cancer, drug resistance, chemotherapy, phase separation, TAZ

3. ACCOMPLISHMENTS:

What were the major goals of the project?

Two specific aims have been proposed: 1) Determine whether the P-TEFb functional equilibrium can be perturbed to affect breast cancer EMT, invasion and metastasis, and whether a small molecule inhibitor of P-TEFb can be employed to halt breast cancer progression; 2) Determine why the EMT and metastasis-related genes are particularly sensitive to transcription elongation control and P-TEFb availability.

Research-Specific Tasks:

Major Task 1: Specific Aim 1: Determine whether the P-TEFb network can be manipulated to suppress breast cancer EMT, invasion and metastasis.	**Months**	**Researcher**	**Percentage completion**
Subtask 1: Determine the roles of P-TEFb complexes in breast cancer EMT, stemness and metastasis in vivo. Overexpression or shRNA-based knockdown of various components of the P-TEFb complexes will be performed in breast cancer cells, and the effects of these manipulations on breast cancer EMT and metastasis will be determined in vitro and in vivo.	1-30	H. Shao (Luo) H. Lu (Zhou)	100%
Subtask 2: Determine whether small molecule CDK9 inhibitors can be used to halt breast cancer metastasis. 8 experimental groups to test various drug dosage and frequency regimes will be tested in vivo. An additional 8 experimental groups for tumor maintenance experiment and 3 groups for orthotopic experiment will be included.	7-36	H. Shao (Luo) Q. Zhu (Luo)	100%
Major Task 2: Specific Aim 2: Determine whether and why the EMT and metastasis-related genes are particularly sensitive to transcription elongation control and P-TEFb availability.	**Months**	**Researcher**	**Percentage completion**
Subtask 1: Determine which SEC complex(es) mediates activation of EMT genes in breast cancer cells.	6-30	H. Lu (Zhou)	100%
Subtask 2: Determine the molecular basis underlying high sensitivity of EMT and metastasis-related genes to control at the transcription elongation stage.	12-36	Y. Lu (Luo)	100%

What was accomplished under these goals?

Specific Aim 1: Determine whether the P-TEFb network can be manipulated to suppress breast cancer EMT, invasion and metastasis.

Subtask 1: Determine the roles of P-TEFb complexes in breast cancer EMT, stemness and metastasis in vivo.

We have previously shown that the depletion of HEXIM1, which is a key component of the 7SK snRNP as well as an inhibitor of the P-TEFb kinase within the complex, in non-invasive breast cancer T47D cells promoted breast cancer EMT and progression. To validate the potential importance of HEXIM1 reduction in human breast cancer, we performed datamining of the TGCA human breast cancer database to determine the types of breast cancer that exhibits HEXIM1 reduction. As shown in Fig. 1, HEXIM1 reduction appears to enrich in the triple negative breast cancer (TNBC). This is potentially exciting because TNBC is the most aggressive human breast cancer that lacks effective targeted drug therapy.

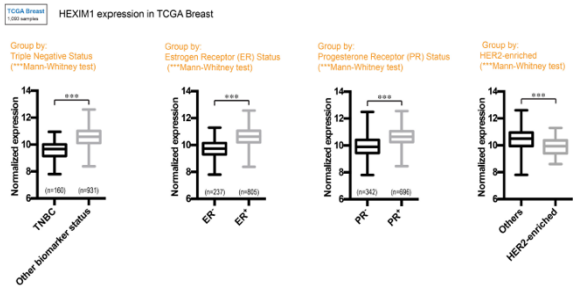

Fig. 1. Analysis of TCGA database showed that HEXIM1 downregulation is enriched in TNBC.

We next performed biochemical analysis to determine the consequence of HEXIM1 knockddown (KD). We have found that the HEXIM1 KD not only released P-TEFb from 7SK snRNP (Fig. 2A), but also reduced the interactions of P-TEFb with the SEC components as well as BRD4. Given that there is no free P-TEFb in the cells, the key question is what new protein partner(s) bind to these released P-TEFb in HEXIM1 KD cells. To answer this question, we performed affinity purification of proteins that associate with P-TEFb in HEXIM1 KD cells. Silver staining of the anti-CDK9 IP revealed a protein of approximately 90kDa that binds to P-TEFb specifically in the KD cells. Mass spec identified this protein as the molecular chaperone heat shock protein HSP90 (Fig. 2B-2C). HSP90 has been shown to facilitate the function of numerous oncoproteins in tumor cells that are said to be 'addicted' to this protein. Consistently, pharmacological inhibition of Hsp90 has demonstrated great promise in cancer treatment. The identification of Hsp90 as a novel partner of P-TEFb in HEXIM1 KD cells has opened a new unexpected direction for our research.

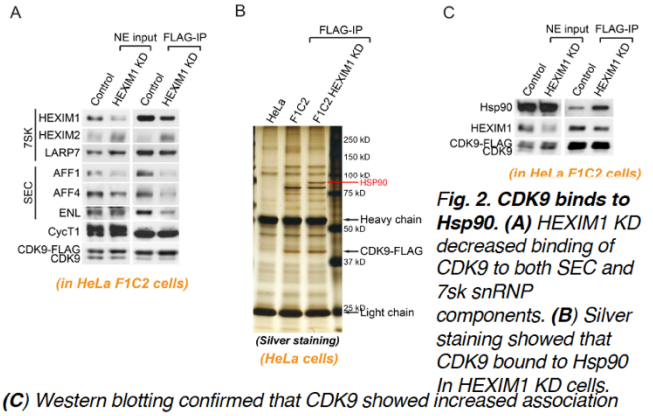

Fig. 2. CDK9 binds to Hsp90. (A) *HEXIM1 KD decreased binding of CDK9 to both SEC and 7sk snRNP components.* ***(B)*** *Silver staining showed that CDK9 bound to Hsp90 In HEXIM1 KD cells.* ***(C)*** *Western blotting confirmed that CDK9 showed increased association with Hsp90 in HEXIM1 KD cells.*

We next investigated how HEXIM1 KD impacts breast cancer proliferation and whether HSP90 plays a role in this process. Using the three-dimensional (3D) matrigel model, we found that HEXIM1 KD resulted in a marked increase in acini size (Fig. 3A). Interestingly, inhibition of HSP90 using a pharmacological inhibitor, geldanamycin (GA), reversed this increase in acini size. Moreover, GA also inhibited proliferation of HEXIM1 KD cells in the regulate 2D culture. Thus, HSP90 activity is required for the increased proliferation caused by HEXIM1 KD. This result also implies that breast cancer cells with reduced HEXIM1 expression may be particularly sensitive to HSP90

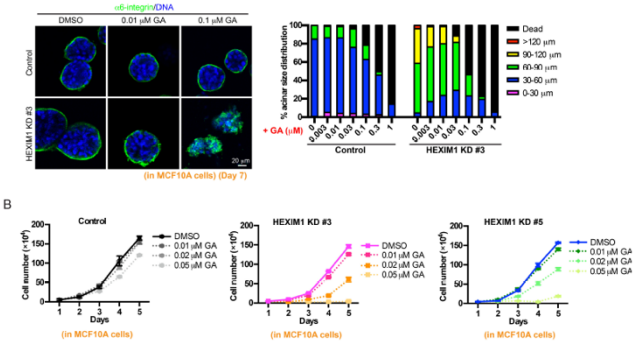

Fig. 3. Inhibition of Hsp90 reversed the increase in cell proliferation caused by HEXIM1 KD. (A) *HEXIM1 KD in MCF10A cells caused an increase in acini size in 3D culture. Hsp90 inhibitor geldanamycin (GA) reversed acini size increase and induced cell death. Quanitification of the acini sizes is shown in the graphs to the right.* ***(B)*** *GA also decreased proliferation of HEXIM1 KD cells in 2D.*

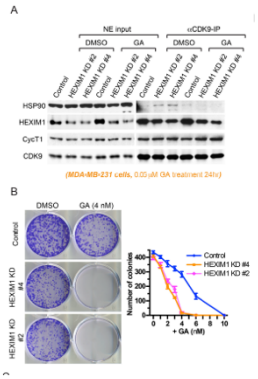

Fig. 4. HEXIM1 KD renders breast cancer cells highly sensitive to Hsp90 inhibitor. (A) *HEXIM1 KD in MDA-MB-231 cells caused an increase in CDK9-Hsp90 binding.* ***(B)*** *HEXIM1 KD cells were highly sensitive to GA inhibition in a colony formation assay.*

inhibition. Since HEXIM1 reduction is enriched in TNBC, it raises an interesting possibility that the TNBC cells might be highly sensitive to HSP90 inhibitors. To test this, we treated the TNBC MDA-MB-231 cells and those with a stable HEXIM1 KD with varying concentrations of GA. Results in Fig. 4 showed that the HEXIM1 KD cells were much more sensitive to GA than parental control cells, with fewer cells surviving the treatment. Furthermore, a combinatory treatment of HSP90 inhibitor and CDK9 inhibitor led to even greater inhibition of colony formation. These results are highly exciting as they provided a novel treatment strategy for TNBC by combining CDK9 and HSP90 inhibitors.

Next we tried to understand the nature of the Hsp90-CDK9 complex. In particular, we asked whether CycT1 is part of the CDK9-Hsp90 complex and whether this Hsp90-bound CDK9 is active as a kinase. The sequential immunoprecipitation assay confirmed that the CDK9-CycT1-Hsp90 complex existed in the HEXIM1 KD cells (Fig. 5A), suggesting that the P-TEFb complex is formed in the presence of Hsp90. Furthermore, in an *in vitro* kinase assay, the Hsp90-bound P-TEFb showed a comparable or higher kinase activity than the CDK9-CycT1 heterodimer, suggesting that the CDK9-CycT1-Hsp90 complex is an active form of P-TEFb (Fig. 5B). This explains why in the HEXIM1 KD cells, although the levels of the known P-TEFb complexes (SEC and BRD4 bound) are decreased, the cells still exhibit active transcription and moderately enhanced oncogenic transformation and invasion.

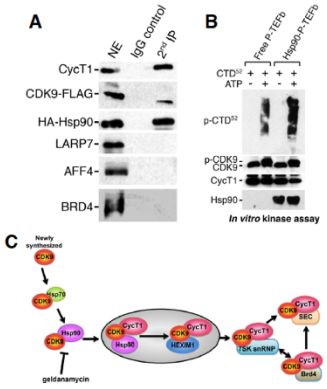

Fig. 5. *(**A**) Sequential immunoprecipitation with anti-FLAG and anti-HA followed by western blotting showed that Hsp90 associates with both CDK9 and Cyclin T1. (**B**) Hsp90-associated P-TEFb can phosphorylate Pol II CTD as well as free P-TEFb. (**C**) Model of P-TEFb maturation and processing.*

Our data suggest a new model that HEXIM1 is essential for the assembly of P-TEFb into the 7SK snRNP by forming an intermediate complex with P-TEFb that allows transfer of P-TEFb from Hsp90 to 7SK snRNP (Fig. 5C). Our data indicate that P-TEFb kinase activation occurs in the Hsp90 complex, and HEXIM1 acts at a step after this activation to enable the assembly of P-TEF into the 7SK snRNP to suppress its kinase activity. Depletion of HEXIM1 not only disrupted the 7SK snRNP, but more importantly, prevented P-TEFb from assembly into the 7SK snRNP and caused accumulation of active P-TEFb in the Hsp90 complex. These active P-TEFb-Hsp90 complexes can activate transcription to promote malignant progression of HEXIM1 KD breast cancer cells, as observed in triple negative breast cancer, and at the same time, render these cells more sensitive to the inhibitors of both Hsp90 and CDK9. This model explains well the observed different effects of the KD of LARP7 versus HEXIM1 on P-TEFb's kinase activity. LARP7 KD does not affect the earlier steps of P-TEFb maturation and processing, but releases P-TEFb from the 7SK snRNP to form more active SEC and BRD4 complexes[26]. In contrast, HEXIM1 KD prevented P-TEFb from incorporating into the 7SK snRNP and all the subsequent complexes (SEC and BRD4), and thus locked P-TEFb in the Hsp90 complex. While LARP7-low malignant breast cancer cells are sensitive to CDK9 and BRD4 inhibitors, HEXIM1-low TNBC are more prone to inhibition by Hsp90 and CDK9 inhibitors. Thus our studies have suggested different treatment options for the highly malignant breast cancer with different mutations in the P-TEFb pathway.

Subtask 2: Determine whether small molecule CDK9 inhibitors can be used to halt breast cancer metastasis.

Since HEXIM1 KD rendered MDA-MB-231 cells more sensitive to killing by the Hsp90 inhibitor Geldenamycin (GA), we predicted that GA might also inhibit the oncogenic potential of these triple negative breast cancer cells. Indeed, treatment of MDA-MB-231 HEXIM1 KD cells with GA led to a significant inhibition of the anchorage independent growth, whereas the same treatment only had a very minor effect on the parental MDA-MB-231 cells (Fig. 6A). To examine the effect of GA on tumor growth in a xenograft mouse

model *in vivo*, we injected control MDA-MB-231 cells and their HEXIM1 KD derivative subcutaneously into the nude mice. The HEXIM1 KD was found to markedly promote tumor development, resulting in bigger tumor sizes and an elevated tumor burden (Fig. 2b). This is consistent with the model that HEXIM1 has tumor suppressor activities. After the tumors reached a measurable size, the mice were administered GA or vehicle (PBS) for 3 additional weeks. While GA had little effect on the control tumors, it inhibited growth of the HEXIM1 KD tumors (Fig. 6B-D). Consistently, HEXIM1 KD tumors exhibited a significantly high level of apoptosis upon GA treatment than control tumors. Thus, similarly to the observations *in vitro*, downregulation of HEXIM1 increased the sensitivity of malignant MDA-MB-231 tumors to Hsp90 inhibition *in vivo*.

These results have been summarized in a paper that has been published recently in Molecular Biology of the Cell (1).

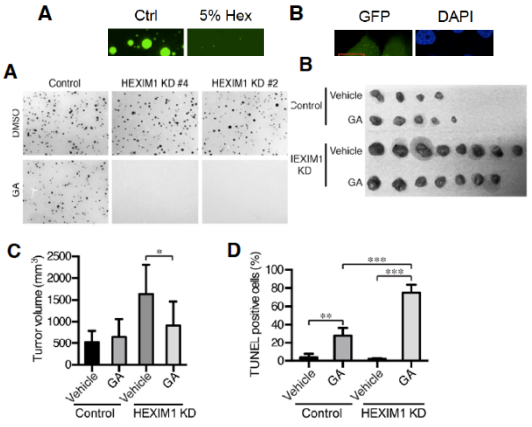

Fig. 6. TNBC can be inhibited by Hsp90 inhibitors. *(**A**) GA inhibits the transforming activity of MDA-MB231 cells with reduced HEXIM1 expression in a soft-agar assay. (**B**) Metastatic breast tumor growth in a xenograft mouse model. (**C**) Quantitation of the tumor volumes from xenograft models. (**D**) Tunnel staining showed an increased apoptosis in xenograft breast tumors in vivo.*

Fig. 3. TAZ forms phase separated condesates in vitro and in vivo. *(**A**) In vitro droplet formation assays showed that TAZ can form droplets that are inhibited by 5% Hex, a compound that disrupts weak hydrophobic interactions. (**B**) TAZ forms nuclear condensates in intact cells. (**C**) The TAZ condensates can fuse into large particles with time, confirming its liquid-like properties. (**D**) TAZ phase separation requires the coil-coil (CC) domain. (**E**) Transcription of TAZ target genes such as CTGF is dependent on its ability to phase separate.*

Specific Aim 2: Determine whether and why the EMT and metastasis-related genes are particularly sensitive to transcription elongation control and P-TEFb availability.

Subtask 1: Determine which SEC complex(es) mediates activation of EMT genes in breast cancer cells.

We have previously shown that the depletion of the 7SK snRNP component LARP7 causes the disruption of the snRNP and release of P-TEFb, which is then converted into two active P-TEFb complexes, the SEC and the BRD4-P-TEFb complex, resulting in the promotion of breast cancer progression. Previously we have determined that a key SEC component, ELL2, played a critical role in mediating the effects of P-TEFb in breast cancer EMT and invasion. During this funding cycle, we continued to examine the importance of the SEC components and its assembly in mediating activation of EMT in breast cancer cells. We disrupted SEC formation by knocking out (KO) a key SEC component AFF4 that is required for assembly of SEC components via CRISPR-Cas9 or by introducing a mutant cyclin T1, cyclin T2A or Cyclin T1-AAG, that blocks binding of SEC components to P-TEFb. Biochemical analysis confirmed the disruption of SEC-P-TEFb complex (Fig. 7A-5B). Interestingly, malignant breast cancer cells (MDA-MB-231 cells) expressing cyclin T2A or AFF4 KD showed greatly decreased cell migration as well as cancer stem cell self-renewal ability (Fig. 7C-5D). These data suggest that SEC plays a key role in mediating the activity of P-TEFb to promote EMT and cancer stem cell expansion in breast cancer cells.

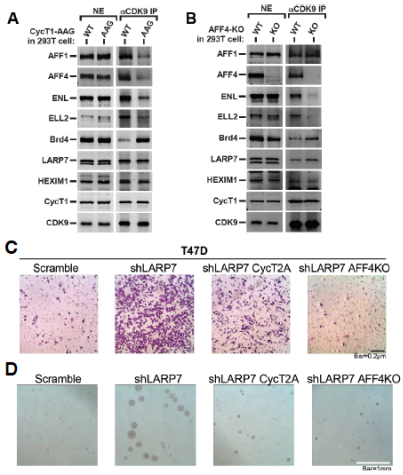

Fig. 7. *Expression of the Cyclin T2A mutant (Cyclin-T1-AAG) (**A**) or AFF1 KO (**B**) in breast cancer cells disrupted the interaction between CDK9 and SEC. The mutant cells also showed a significant reduction in cell migration (**C**) and mammosphere formation (**D**).*

Subtask 2: Determine the molecular basis underlying high sensitivity of EMT and metastasis-related genes to control at the transcription elongation stage.

We have developed a novel project to address the question why P-TEFb specifically affects the EMT and metastasis genes. We hypothesized that P-TEFb may be recruited to specific nuclear structures or

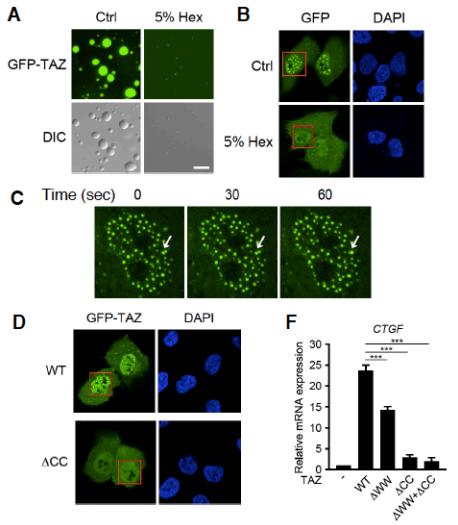

Fig. 8. TAZ forms phase separated condesates in vitro and in vivo. *(**A**) In vitro droplet formation assays showed that TAZ can form droplets that are inhibited by 5% Hex, a compound that disrupts weak hydrophobic interactions. (**B**) TAZ forms nuclear condensates in intact cells. (**C**) The TAZ condensates can fuse into large particles with time, confirming its liquid-like properties. (**D**) TAZ phase separation requires the coil-coil (CC) domain. (**E**) Transcription of TAZ target genes such as CTGF is dependent on its ability to phase separate.*

complexes by master EMT transcription factors to promote breast cancer progression. To this end, we have discovered that a known master EMT transcription factor, TAZ, that plays a critical role in promoting breast cancer EMT and invasion, and cancer stem cell expansion may recruit P-TEFb to phase separated nuclear condensates to regulate the expression of EMT genes. We showed that TAZ formed liquid-like phase separated nuclear condensates both in vitro and in vivo, and this activity is essential for its transcriptional activation activity (Fig. 8). Interestingly, we have previously found that P-TEFb also forms phase separated condensates that are critical for its transcription activity. In addition, Brd4 has been recently shown to bind to TAZ and its closely related YAP. These observations have raised an intriguing possibility that TAZ, P-TEFb and Brd4 may co-localize in the large transcription elongation complex to regulate gene expression. Indeed, we have detected Brd4 and CDK9 in the TAZ puncta in the nucleus, strongly supporting that TAZ may interact with P-TEFb and Brd4 in the nucleus and may recruit them to EMT gene promoters to activate their expression (Fig. 9). This could explain the functional specificity of P-TEFb in promoting breast cancer progression. This study has been summarized in a paper that has recently been published in Nature Cell Biology.

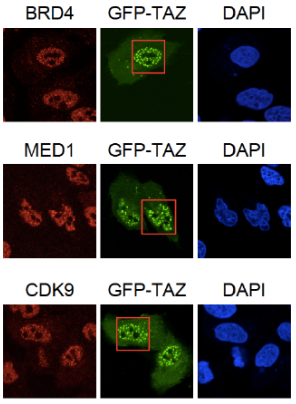

Fig. 9. TAZ nuclear condensates contain BRD4, CDK9 and the mediator complex.

What opportunities for training and professional development has the project provided?

This project represents a major focus of research conducted in both the Zhou and Luo laboratories. It applies the concepts and experimental techniques derived from multiple disciplines and thus offer Dr. Hengyi Shao and Dr. Huasong Lu, an excellent training opportunity to become exposed to and familiar with the languages and tools used in the areas of biochemistry, molecular cell biology, and bioinformatics. Through supervising, training, coordinating, recruiting, motivating, writing and defining research directions for all specific aims, Dr. Zhou and Dr. Luo, the principal investigators of these two partnering awards have been intimately involved in every aspect of the project. In addition, the two PIs have taught beginning graduate students to set up experiments, and used the weekly joint lab meetings and journal clubs as opportunities to train the students and postdoctoral researchers to better organize their data and thoughts and give more succinct and impressive presentations.

The scientific environment at UC Berkeley, where this project is being performed, also provides excellent opportunities for intellectual growth and collaboration for the researchers associated with this project. Many regularly scheduled seminars encompassing all areas of modern biology are available and can benefit this project. The MCB Department and the Division of Biochemistry and Structural Biology and Division of Cell and Developmental Biology, to which the Zhou and Luo laboratory belongs respectively, organize annual retreats where graduate students and postdoctoral researchers from the two laboratories have opportunities to present their latest findings and obtain valuable feedbacks. Additional interactions are frequent between our two labs and those of Drs James Hurley, Britt Glaunsinger, Robert Tjian, Jennifer Doudna, Michael Botchan, and Michael Rapé, among others, and provide further intellectual support, technical help with experiments and useful reagents/tools. Moreover, many UC Berkeley labs are at the forefront of technology innovation, providing the researchers in the two labs with an opportunity to take advantage of the best new methods in proteomics, computational, imaging, genomic editing, and structural analyses. In summary, the breadth and depth of the UC Berkeley scientific environment where the Zhou and Luo laboratories are located provide unparalleled opportunities for training and professional development for all the researchers working on this project.

How were the results disseminated to communities of interest?

The results from these studies have been summarized in two papes that have been published recently in Molecular Biology of the Cell and Nature Cell Biology. Dr. Luo has also publically discussed these results in scientific conferences.

What do you plan to do during the next reporting period to accomplish the goals?

Nothing to report

4. IMPACT:

What was the impact on the development of the principal discipline(s) of the project?

The successful completion of the project has not only established a new conceptual paradigm, but also have important clinical implications in halting breast cancer progression and metastasis. Specifically, our study has confirmed the components of the general transcription elongation machinery as an important factor to drive the metastasis of breast cancer. By employing a novel highly selective P-TEFb inhibitor in the proposed experiments, we have directly tested and validated the idea that targeting the P-TEFb network of complexes can be an effective strategy to treat metastatic breast cancer.

What was the impact on other disciplines?

Nothing to Report.

What was the impact on technology transfer?

Nothing to Report.

What was the impact on society beyond science and technology?

Nothing to Report.

5. CHANGES/PROBLEMS:

Changes in approach and reasons for change

Nothing to Report.

Actual or anticipated problems or delays and actions or plans to resolve them

Nothing to Report.

Changes that had a significant impact on expenditures

Nothing to Report.

Significant changes in use or care of human subjects, vertebrate animals, biohazards, and/or select agents

Nothing to Report.

6. PRODUCTS:

Publications, conference papers, and presentations

Two manuscripts:

1. Shao, H., Zhu, Q., Lu, H., Chang, A., Zhou, Q., and **Luo, K.** (2020) HEXIM1 promotes CDK9 maturation to regulate drug sensitivity in triple negative breast cancer. Molecular Biology of the Cell; In press.

2. Wu, T., Lu, Y., Gutman, O., Lu, H., Zhou, Q., Henis, Y., and **Luo, K.** (2019) Phase Separation of TAZ Compartmentalizes the Transcription Machinery to Promote Gene Expression. In review: Nature Cell Biology.

Oral presentation:

1. May 2019; AACR conference: The Hippo pathway: Signaling, Cancer and Beyond. By Kunxin Luo. Title of Talk: Regulation of Hippo and TAZ signaling in breast cancer.

2. November 2018; Harvey Lodish 50th Symposium, The Whitehead Institute for Biomedical Research, Cambridge, Massachusette. By Kunxin Luo, Title of talk: Transcription elongation machinery and breast cancer.

Other publications, conference papers, and presentations.

Nothing to Report.

Website(s) or other Internet site(s)

Nothing to Report.

Technologies or techniques

Nothing to Report.

Inventions, patent applications, and/or licenses

Nothing to Report.

Other Products

New breast cancer stable cell lines have been established. They will be freely shared with the scientific community upon request.

7. PARTICIPANTS & OTHER COLLABORATING ORGANIZATIONS

What individuals have worked on the project?

Name:	Kunxin Luo
Project Role:	Partnering PI
Researcher Identifier:	kluo (eCommon ID)
Nearest person month worked:	4
Contribution to Project:	Dr. Luo supervises, trains, recruits, and motivates all personnel on the project. She also coordinates and defines research directions for all specific aims together with Dr. Qiang Zhou, the initiating PI
Funding Support:	This award

Name:	Hengyi Shao
Project Role:	Postdoctoral researcher
Researcher Identifier:	Hengyishao (eCommon ID)
Nearest person month worked:	12
Contribution to Project:	Dr. Shao has performed various EMT assays to test whether activation of P-TEFb leads to EMT and metastasis of breast cancer cells and discovered Hsp90 as the associated protein of P-TEFb.
Funding Support:	This award
Name:	Qingwei Zhu
Project Role:	Postdoctoral researcher
Researcher Identifier:	qingweizhu (eCommon ID)
Nearest person month worked:	2
Contribution to Project:	Dr. Zhu continued the biochemical characterization of the Hsp90-P-TEFb complex and helped to finish the final set of experiments requested by the journal reviewers.
Funding Support:	This award

Name:	Huasong Lu
Project Role:	Postdoctoral researcher
Researcher Identifier:	Luhuasong (eCommon ID)
Nearest person month worked:	2
Contribution to Project:	Dr. Lu has participated in the generation of all the cell lines stably knocking out the components of various P-TEFb complexes and performed some of the biochemical experiments.
Funding Support:	NIH

Name:	Yi Lu
Project Role:	Visiting Scholar
Researcher Identifier:	yilu (eCommon ID)
Nearest person month worked:	2
Contribution to Project:	Mr. Lu has participated in the characterization of TAZ phase separation in breast cancer cells and identified the co-localization of CDK9, BRD4 and TAZ in the nuclear condensates for transcription.

Funding Support:	Berkeley Scholars program

Has there been a change in the active other support of the PD/PI(s) or senior/key personnel since the last reporting period?

Nothing to report

What other organizations were involved as partners? None.

8. SPECIAL REPORTING REQUIREMENTS:

An independent report will be submitted by the initiating PI Dr. Qiang Zhou.

9. APPENDICES:

Two publications.

nature cell biology

ARTICLES

https://doi.org/10.1038/s41556-020-0485-0

Phase separation of TAZ compartmentalizes the transcription machinery to promote gene expression

Yi Lu[1,4], Tiantian Wu[1,2,4], Orit Gutman[3], Huasong Lu[1], Qiang Zhou[1], Yoav I. Henis[3] and Kunxin Luo[1]✉

TAZ promotes growth, development and tumorigenesis by regulating the expression of target genes. However, the manner in which TAZ orchestrates the transcriptional responses is poorly defined. Here we demonstrate that TAZ forms nuclear condensates through liquid–liquid phase separation to compartmentalize its DNA-binding cofactor TEAD4, coactivators BRD4 and MED1, and the transcription elongation factor CDK9 for transcription. TAZ forms phase-separated droplets in vitro and liquid-like nuclear condensates in vivo, and this ability is negatively regulated by Hippo signalling through LATS-mediated phosphorylation and is mediated by the coiled-coil (CC) domain. Deletion of the TAZ CC domain or substitution with the YAP CC domain prevents the phase separation of TAZ and its ability to induce the expression of TAZ-specific target genes. Thus, we identify a mechanism of transcriptional activation by TAZ and demonstrate that pathway-specific transcription factors also engage the phase-separation mechanism for efficient and specific transcriptional activation.

The Hippo pathway is an evolutionarily conserved pathway that regulates cell proliferation, tissue homeostasis, organ size and tumorigenesis[1–4]. At the centre of this pathway is a kinase core that consists of the MST1 or MST2, LATS1 or LATS2 kinases, as well as two accessory molecules, SAV1 and MOB1 (refs. [5,6]). A variety of signals derived from cell–cell contact, cell polarity, mechanotransduction, cellular stress and metabolism activate the MST1/2 and LATS1/2 kinases. In turn, the activated LATS1/2 phosphorylates the key transcription effectors TAZ and YAP, leading to the increased cytoplasmic localization and subsequent inhibition of their transcription activity of TAZ and YAP[7–10]. Once Hippo signalling is inactivated, TAZ and YAP accumulate in the nucleus and bind to the DNA-binding cofactor TEAD as well as transcriptional coactivators BRD4 and MED1 (refs. [11,12]). Through these interactions, YAP and TAZ recruit these coactivators in addition to the transcription elongation complex to stimulate gene expression[11,13]. In normal tissues, the intact tissue architecture and cell–cell adhesion activate Hippo signalling to repress the activity of TAZ and YAP. In cancer in humans, in which tissue architecture is disrupted, the expression of TAZ and YAP is increased. In particular, TAZ is upregulated in more than 20% of breast cancer tissues[14], and these high levels of TAZ correlate with increased invasiveness and poorer outcomes for patients[15]. Furthermore, overexpression of TAZ, especially the constitutively active TAZ^{S89A}, which is resistant to inhibition by LATS1/2, promotes the expansion of cancer stem cell population and tumour invasion[15].

TAZ and YAP are paralogues with similar domain structures, partially overlapping functions[16] and are similarly regulated by Hippo kinases. Furthermore, YAP and TAZ double-knockout (KO) mice display a more severe phenotype than either of the single-KO mice[17,18], suggesting that there are some functional overlaps. However, YAP and TAZ are not redundant—TAZ KO mice are viable with defects in the kidney and lung, whereas YAP KO in mice is embryonically lethal with severe developmental defects[19,20]. These functional differences might arise from differential expression, localization and downstream target genes. TAZ and YAP both contain a TEAD-binding (TB) domain, a WW domain(s), a coiled-coil (CC) domain and a transcription activation (TA) domain, and can bind to the same transcription factors, including TEAD and Runx[21,22]. However, there are important differences in the sequences within these domains that enable them to bind to different transcription factors (for example, PPARγ and Pax3 for TAZ; ErbB4 and p73 for YAP)[23] and activate different target genes[16]. Although several mechanisms have been proposed to mediate transcriptional activation by both YAP or TAZ[11,12], the molecular mechanism that underlies the functional differences between the two has not been well defined.

Here we report that TAZ, but not YAP, forms liquid-like biomolecular condensates that compartmentalize and concentrate transcription coactivators and elongation machinery. The assembly of dynamic membraneless compartments through liquid–liquid phase separation (LLPS) is essential for temporal and spatial control of numerous biochemical processes. These LLPS condensates may function as scaffolds to concentrate proteins with similar functions, to insulate protein complexes that act in different signalling pathways to generate specificity, or to sequester proteins to facilitate or prevent inactivation. As such, these LLPS condensates are vital for many physiological processes, and their disruption may be associated with many pathological conditions[24]. Proteins that tend to undergo LLPS often contain intrinsically disordered regions (IDRs) or are involved in weak multivalent protein–protein or protein–RNA interactions. Other factors, such as temperature, pH, salt and protein concentrations, also influence the ability of proteins to undergo LLPS, and post-translational modifications can further

[1]Department of Molecular and Cell Biology, University of California, Berkeley, Berkeley, CA, USA. [2]State Key Laboratory of Cellular Stress Biology, School of Life Sciences, Xiamen University, Xiamen, China. [3]Department of Neurobiology, George S. Wise Faculty of Life Sciences, Tel Aviv University, Tel Aviv, Israel. [4]These authors contributed equally: Yi Lu, Tiantian Wu. ✉e-mail: kluo@berkeley.edu

regulate the ability of proteins to move in or out of these condensates, providing switch-like control.

Recently, LLPS has been shown to have a critical role in transcriptional control. The FET (FUS, EWS and TAF15) family of sequence-specific transcription factors, the transcription elongation factor P-TEFb as well as the super enhancers MED1 and BRD4 all form LLPS condensates to activate gene expression[13,25,26]. Given that TAZ and YAP can interact with the transcription elongation factors and function at the super enhancers together with BRD4 and MED1 (refs. [11,12]), we investigated whether TAZ and YAP also form LLPS condensates. We found that, in the absence of crowding agents, TAZ, but not YAP, undergoes LLPS through its CC domain, and these TAZ LLPS structures compartmentalize transcriptional cofactors and transcription elongation machinery to facilitate TAZ-specific gene expression. Thus, we identified a phase-separation mechanism that distinguishes between TAZ and YAP to efficiently engage the transcriptional machinery for specific expression of target genes.

Results

TAZ undergoes phase separation in vitro and in vivo. The full-length TAZ protein appears to be largely unfolded[27] and contains many IDRs (Fig. 1a, top) as well as several domains that are important for interactions with other proteins[2,28]. Given that proteins with extensive IDRs that are also involved in multivalent protein interactions tend to undergo LLPS[29,30], we investigated whether TAZ has the ability to undergo phase separation. Purified GFP–TAZ (Extended Data Fig. 1a) spontaneously formed microsized droplets in solutions (Fig. 1b), and the droplets were larger and more numerous at higher protein and salt concentrations and high temperatures (Fig. 1b–d), suggesting that hydrophobic interactions, rather than electrostatic interactions, are involved in this process. Consistent with this, droplet formation was substantially inhibited by 5% 1,6-hexanediol—a compound that putatively disrupts weak hydrophobic interactions (Fig. 1e)—and was completely abolished by treatment with heat or proteinase K (Extended Data Fig. 1b).

To test whether TAZ also undergoes LLPS in intact cells and tissues, we ectopically expressed GFP–TAZ in MCF-10A cells at a lower level than that of endogenous TAZ (Extended Data Fig. 1c) and found that GFP–TAZ formed discrete puncta in the nucleus, which could be disrupted by 5% 1,6-hexanediol (Fig. 1f). Ectopically expressed Flag–TAZ also formed nuclear puncta, excluding the possibility that the puncta were artificially formed by the GFP tag (Extended Data Fig. 1d). Importantly, endogenous TAZ also exhibited formation of nuclear puncta in both MCF-10A and HeLa cells (Fig. 1g). We also examined TAZ localization in a tissue array containing 27 normal breast samples and 294 invasive breast carcinoma samples. Compared with normal breast tissue samples, in which TAZ was expressed mainly in the cytoplasm at low levels, invasive breast cancer tissue samples showed significantly upregulated expression of TAZ that was localized in discrete nuclear puncta (Fig. 1h). Thus, TAZ forms phase-separated puncta in intact cells and breast cancer tissue samples.

YAP differs from TAZ in its ability to undergo LLPS. YAP is a paralogue of TAZ with extensive sequence similarities, including extensive IDRs (Fig. 1a, bottom). Interestingly, under the same experimental conditions as described for TAZ, YAP failed to form droplets in vitro over a wide range of protein and salt concentrations and temperatures (Fig. 1b–d, Extended Data Fig. 2a–d). YAP1–2α, an isoform of YAP1 that contains two WW domains also failed to form droplets in vitro (Extended Data Fig. 2e). Only in the presence of specific crowding agents such as PEG-8000, Ficoll or Dextran—but not glycerol, sucrose or bovine serum albumin—did YAP form droplets (Extended Data Fig. 2f,g). This is consistent with a recent paper that suggested that YAP can phase separate in the presence of PEG-8000 (ref. [31]). Ectopically expressed GFP–YAP did not form nuclear puncta in all of the cell lines tested in the absence of crowding agents (Fig. 1f, Extended Data Fig. 2h). Thus, YAP differs from TAZ in its ability to undergo LLPS.

TAZ puncta exhibit liquid-like properties. A spherical shape, an ability to fuse and recovery from photobleaching are some of the features of a liquid-like phase-separated structure[29,30]. Live-cell imaging showed that the TAZ nuclear condensates readily fused into larger structures over time (Fig. 2a). Fluorescence recovery after photobleaching (FRAP) beam-size analysis[32], using ×63 and ×40 objectives to generate two Gaussian laser beam sizes, was performed to examine the biophysical properties of the GFP–TAZ condensates[32]. If FRAP occurs by diffusion, τ (the characteristic fluorescence recovery time) is proportional to the bleached area ($\tau_D = \omega^2/4D$ where τ_D is the characteristic diffusion time, D the lateral diffusion coefficient and ω is the Gaussian radius of the laser beam). Thus, for recovery by lateral diffusion, the ratio between the τ values obtained with the two objectives, $\tau(\times40)/\tau(\times63)$, should equal the ratio between the bleached areas (2.28)[33]. If FRAP occurs by exchange with free fluorescent proteins, τ reflects the chemical relaxation time, which is independent of the bleached area, that is $\tau(\times40)/\tau(\times63) = 1$ (refs. [32,34]). Analysis of GFP–TAZ condensates with a diameter of ~3 μm showed that the $\tau(\times40)/\tau(\times63)$ ratio (2.23) is similar to that expected for recovery by lateral diffusion[33] (Fig. 2b–e). A similar value is expected for 3D diffusion in FRAP experiments involving fluorescence collection from a restricted confocal plane[35]. The calculated lateral diffusion coefficient (D) yields $0.11 \pm 0.01\ \mu m^2 s^{-1}$, which is in line with that of the RNA-binding protein hnRNPA1 (4.2 s recovery time, with high recovery)[36] and an RNA helicase (2.5 s, 80% recovery, with D of ~$0.3\ \mu m^2 s^{-1}$)[37] in nuclear LLPS droplets. By contrast, GFP–TAZ in the cytoplasm displays a much faster diffusion, with $D = 1.5\ \mu m^2 s^{-1}$ (Fig. 2d). Notably, bleaching whole, small GFP–TAZ organelles in the nuclei (diameter of ~1.2 μm, using the ×40 objective) yielded τ of about 2.8 s with a mobile fraction of above 70% (Fig. 2g–j) and $D = 0.12\ \mu m^2 s^{-1}$, in line with the results obtained on large organelles and with the reported recovery rates of RNA-binding proteins after bleaching whole droplets[36]. These data suggest that TAZ is highly dynamic, with rapid diffusion of molecules within the condensates as well as between the condensates and the surrounding nuclear contents, and that the TAZ nuclear condensates represent a separate liquid phase that is formed through LLPS.

The CC domain is necessary for TAZ LLPS. To identify the domains in TAZ that are required for phase separation, mutant GFP–TAZ with deletion of the TB, WW or CC domain individually, or the WW and the CC domains together (ΔWW+ΔCC) was purified (Extended Data Fig. 3a,b) and analysed using droplet-formation assays in vitro. Whereas the removal of the TB domain had little effects on TAZ LLPS, deletion of the WW or CC domain considerably reduced, but did not eliminate, droplet formation. Interestingly, deletion of both WW and CC domains abolished TAZ LLPS (Fig. 3a). Consistent with these results, deletion of the CC or WW domain individually substantially reduced LLPS and deletion of both abolished LLPS in cells (Fig. 3b, Extended Data Fig. 3c). Thus, the CC domain and—to a lesser extent—the WW domain are required for TAZ phase separation.

The CC domain distinguishes TAZ from YAP in their ability to undergo LLPS. Taking advantage of the difference in the ability of YAP and TAZ to undergo LLPS, we generated TAZ–YAP chimeric proteins in which the WW or CC domain of TAZ were swapped—either individually or together—with the WW or CC domains of YAP (Fig. 4a). In the in vitro droplet-formation assays (Fig. 4b,c), full-length TAZ and chimeric TAZ containing the YAP

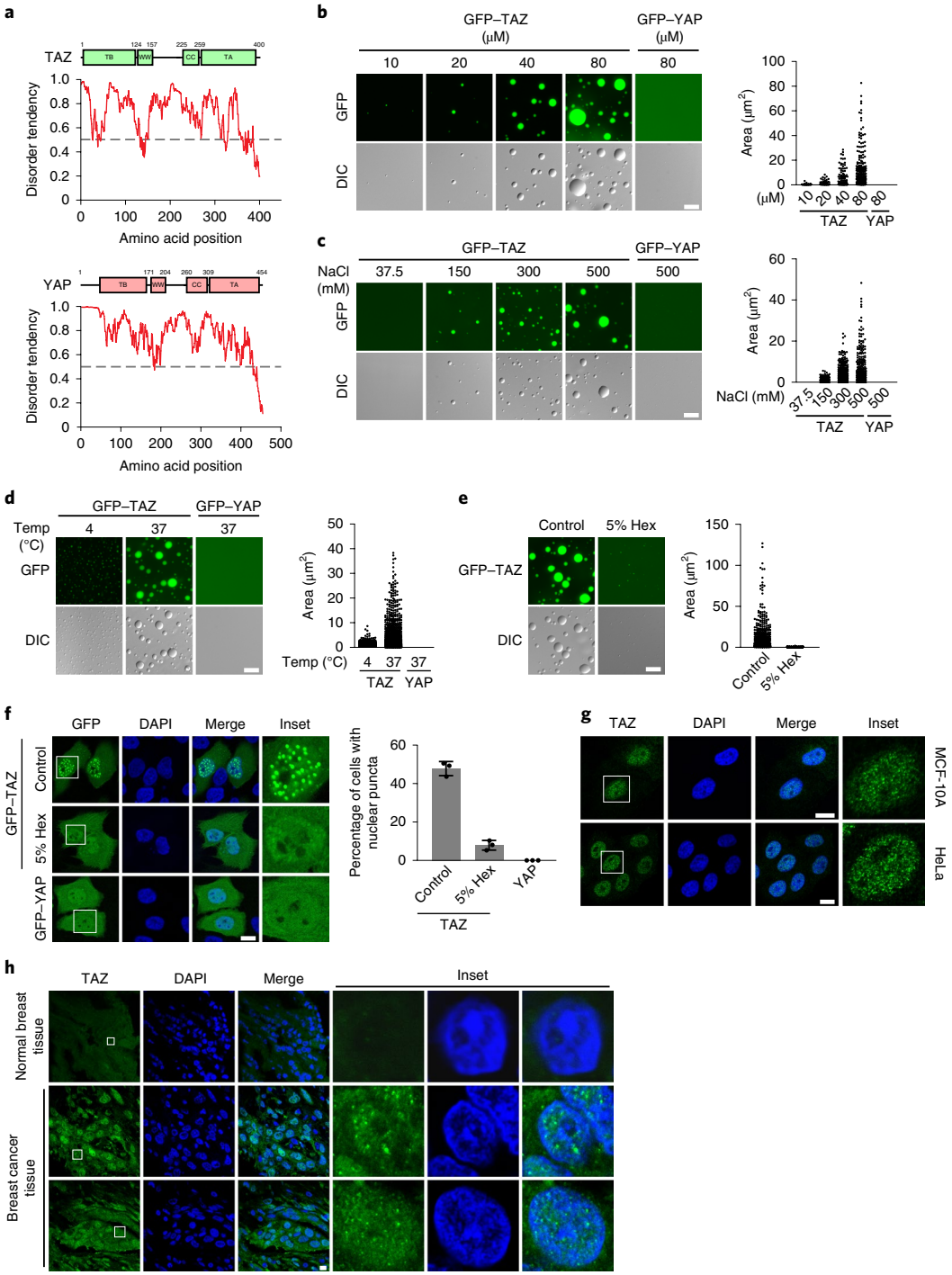

Fig. 1 | TAZ undergoes LLPS in vitro and in vivo. a, Domain structure and the intrinsically disordered tendency of TAZ (top) and YAP (bottom). IUPred assigned scores of disordered tendencies between 0 and 1 to the sequences (a score of more than 0.5 indicates disordered). **b**, GFP–TAZ and GFP–YAP were analysed for the formation of droplets at room temperature and 500 mM NaCl. **c**,**d**, GFP–TAZ or GFP–YAP (50 μM) was analysed using droplet-formation assays at room temperature with the indicated concentrations of NaCl (**c**) or at 4 °C or 37 °C with 150 mM NaCl (**d**). Temp, temperature. **e**, 1,6-hexanediol (Hex; 5%) disrupted droplet formation. GFP–TAZ (50 μM) was analysed at room temperature and with 500 mM NaCl with or without 5% Hex. For **b**–**e**, representative fluorescence and differential interference contrast (DIC) images of the droplets (left) and quantification of the size and number of droplets (right) are shown. Each dot represents a droplet. Data are mean ± s.e.m. Droplets in $n = 3$ fields ($166 \times 124\ \mu m^2$) in each group were quantified. **f**, GFP–TAZ formed nuclear puncta in MCF-10A cells. Cells transfected with GFP–TAZ or GFP–YAP were treated with or without 5% Hex for 1 min and imaged. Nuclei were stained with 4,6-diamidino-2-phenylindole (DAPI; blue). Inset: an enlarged view of the nuclear puncta magnified by 3.07, 3.47 and 2.96 times, respectively. Quantification of the percentage of cells that displayed nuclear puncta is shown on the right. Data are mean ± s.e.m.; 80 transfected cells in each group were quantified; $n = 3$ biologically independent samples. **g**, Endogenous TAZ showed nuclear puncta in the indicated cells. TAZ was stained with anti-TAZ antibodies (green). Insets, magnification by 2.56 and 3.04 times, respectively. **h**, TAZ formed nuclear puncta in tissues. The human breast cancer tissue array was stained with anti-TAZ antibodies (green), and representative images are shown. Insets, magnification by 13.34, 10.00 and 8.88 times, respectively. The experiments shown in **b**–**g** were repeated independently three times with similar results. The experiments shown in **h** were repeated independently twice with similar results. Source data are available online. For **b**–**h**, scale bars, 10 μm.

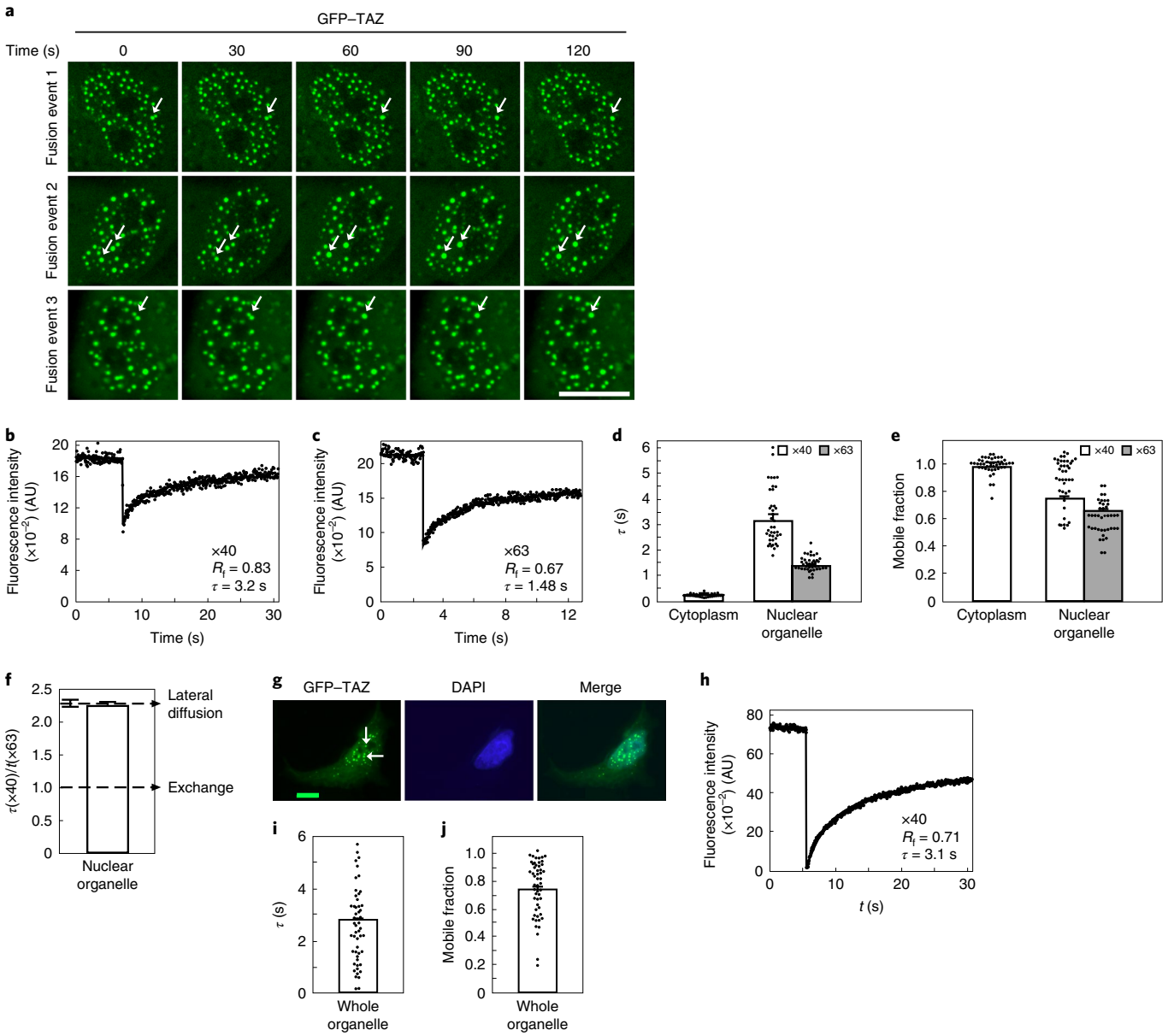

Fig. 2 | TAZ nuclear condensates display liquid-like properties. a, Live-cell imaging of MCF-10A cells expressing GFP–TAZ. The arrows indicate representative TAZ puncta that fused over time. This assay was performed three times (three independent transfections) with similar results. **b**,**c**, Typical FRAP curves with ×40 (**b**) or ×63 (**c**) objectives in organelles larger than the laser beam. The solid lines are a nonlinear regression best fit to the diffusion equation. **d**,**e**, Average values for the FRAP data shown in **b** and **c**. Data are mean ± s.e.m. of GFP–TAZ in the cytoplasm ($n = 45$ independent measurements) or nuclear puncta ($n = 40$ independent measurements). **f**, FRAP beam-size bootstrap analysis. The studies used ×40 and ×63 objectives, the beam size measurements of which ($n = 59$ independent measurements) yielded a $\omega^2(\times40)/\omega^2(\times63)$ ratio of 2.28 ± 0.05. A similar ratio for $\tau(\times40)/\tau(\times63)$ is expected for FRAP by lateral diffusion, whereas a τ ratio of 1 indicates recovery by exchange. The s.e.m. values of the τ ratios were calculated from the τ values shown in **d**, nuclear organelle ($n = 40$ for each objective), using bootstrap analysis (1,000 bootstrap resampling values). The $\tau(\times40)/\tau(\times63)$ ratio (2.26) of GFP–TAZ in the large organelles is similar to the 2.28 beam size ratio ($P = 0.44$, Student's two-tailed t-test), in line with FRAP by diffusion. Calculating D from the τ values yields $D = 0.11 \pm 0.01\,\mu m^2\,s^{-1}$, with $R_f = 0.65$–0.75. τ of GFP–TAZ in the cytoplasm (**d**), measured using a ×40 objective, is more than tenfold smaller (faster diffusion, $D = 1.5 \pm 0.07\,\mu m^2\,s^{-1}$). **g**, A fluorescence image of GFP–TAZ organelles in the nuclei (arrow) processed for whole-organelle bleach (150 ms) using a ×40 objective. The assay was repeated 40 times with similar images obtained. Scale bar, 10 µm. **h**, A typical FRAP curve of bleaching a whole small organelle. **i**,**j**, Average values (τ in **i**, mobile fraction in **j**) of FRAP (×40 objective) of whole organelles with a diameter of ~1.2 µm. Data are mean ± s.e.m. of $n = 52$ independent experiments. The τ and R_f values were very similar to those obtained by bleaching a spot on a large organelle (compare with **d** and **e**). On the basis of the estimated organelle diameter, the D value from these experiments is $0.12\,\mu m^2\,s^{-1}$. Source data are available online.

WW domain (WW^Y) readily formed droplets; by contrast, TAZ chimaeras containing the YAP CC domain (CC^Y) or the YAP WW and CC domains (WW^Y+CC^Y) failed to do so (Fig. 4c). Similarly, TAZ chimaeras that contained either the YAP CC domain alone or the YAP CC and WW domains did not form nuclear puncta in cells, but TAZ chimaeras that contained the YAP WW domain readily formed puncta, similar to wild-type TAZ (Fig. 4d, Extended Data Fig. 3d). The CC domain therefore distinguishes between TAZ and YAP in their ability to undergo LLPS. Interestingly, TAZ, but not YAP, could effectively homodimerize in vivo (Figs. 3c and 4e) and

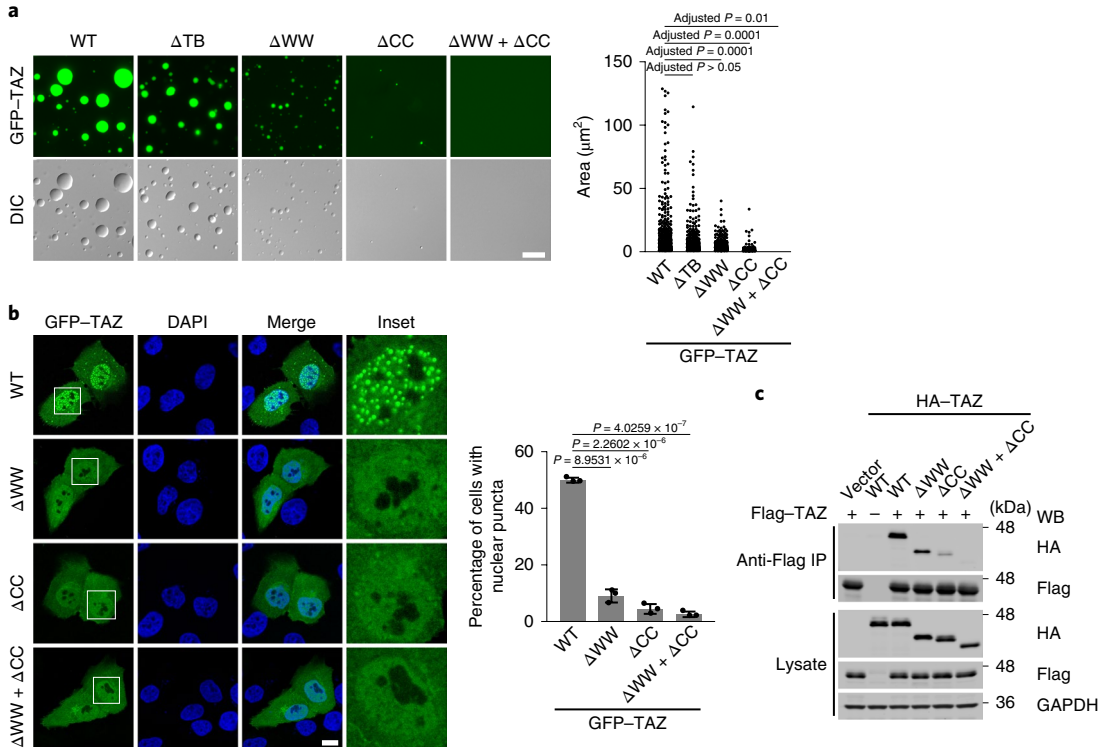

Fig. 3 | The WW domain and CC domain are required for TAZ LLPS. a, GFP–TAZ (WT), ΔTB, ΔWW, ΔCC and ΔWW+ΔCC proteins (50 μM) were analysed using droplet-formation assays at room temperature in the presence of 500 mM NaCl. Right, quantification of the droplets. Scale bar, 10 μm. Data are mean ± s.e.m. Statistical significance was evaluated using one-way ANOVA with Krusk–Wallis test. Droplets in $n = 3$ fields in each group were quantified. **b**, Confocal microscopy images of MCF-10A cells transfected with *GFP–TAZ* and various mutants (left). Scale bar, 10 μm. Right, quantification of the percentage of cells that showed nuclear puncta. Insets, magnification by 3.84, 3.84, 3.57 and 3.84 times, respectively. Data are mean ± s.e.m. *P* values were determined using unpaired two-tailed Student's *t*-tests; 80 transfected cells in each group were quantified; $n = 3$ biologically independent samples. **c**, HA-tagged WT or mutant *TAZ* was cotransfected into HEK293T cells together with Flag-TAZ. Dimerization of TAZ was analysed by immunoprecipitation (IP) with anti-Flag antibodies and detected using western blotting (WB) with anti-HA antibodies (top). The abundance of these proteins in the cell lysates was assessed using western blotting (bottom). GAPDH was used as a loading control. The experiments in **a**–**c** were repeated independently three times with similar results. Source data are available online.

in vitro (Extended Data Fig. 3e) through its CC domain. Deletion of the TAZ CC domain (Fig. 3c) or substituting it with the CC domain of YAP (Fig. 4e) impaired this oligomerization substantially. This differential ability to engage in homo-oligomerization between TAZ and YAP may contribute to their difference in LLPS.

Notably, we found that the TAZ WW domain also bound to TAZ itself, probably through the N-terminal regions (Extended Data Fig. 3e), and this could further enhance the multivalent interactions that are required for effective LLPS. This is why both the CC and WW domains are necessary for LLPS. In light of these data, we generated YAP chimeric proteins containing the TAZ WW and CC domains either individually or together (Extended Data Fig. 4a). In contrast to WT YAP, these chimeric proteins showed a substantially increased ability to phase separate in the presence of PEG (Extended Data Fig 4c–e) but could not undergo LLPS without PEG (Extended Data Fig. 4b), suggesting that, although the TAZ CC and WW domains are necessary for LLPS, they are not sufficient.

TAZ phase separation is negatively regulated by Hippo signalling and LATS1/2. To examine whether the TAZ LLPS is regulated by Hippo signalling, we treated the MCF10A (Fig. 5) or HeLa (Extended Data Fig. 5) cells with serum, lysophosphatidic acid (LPA), EGF[38] or fibronectin[39], or altered cell density, matrix stiffness or the actin cytoskeleton. After serum starvation, TAZ was diffusely localized in the cytoplasm, as described previously[40,41]. The addition of serum or LPA or EGF led to the accumulation of TAZ in the nucleus and, in particular, in the nuclear puncta (Fig. 5a,b, Extended Data Fig. 5a). At high cell density, TAZ was largely cytoplasmic or degraded[2,40], whereas, at low cell density, the stabilized TAZ was enriched in the nucleus and clearly formed nuclear condensates (Fig. 5c). Fibronectin also promoted TAZ localization in the nuclear puncta (Fig. 5d, Extended Data Fig. 5b). Furthermore, at high stiffness, TAZ accumulated in the nucleus and formed LLPS; by contrast, at low stiffness, TAZ was degraded (Fig. 5e, Extended Data Fig. 5c). Consistent with the notion that the actin cytoskeleton is essential for the regulation of TAZ and YAP by these mechanical and biochemical cues[6,42], disruption of the actin cytoskeleton by latrunculin B effectively blocked TAZ LLPS (Fig. 5f, Extended Data Fig. 5d). Thus, TAZ LLPS is inhibited by Hippo signalling and is sensitive to mechanical cues.

Ectopic expression of LATS2 either alone or together with MST2 inhibited TAZ LLPS, whereas the kinase-inactive $LATS2^{KD}$ failed to block this process (Fig. 6a), suggesting that phosphorylation of TAZ by LATS2 prevented LLPS. Consistent with this, knocking down LATS1 and LATS2 in cells in a high-density culture promoted TAZ LLPS (Fig. 6b). Furthermore, LATS2-expressing cells that were treated with the proteasome inhibitor MG132 retained most of the TAZ in the nucleus, but the phosphorylated TAZ did not form nuclear puncta (Fig. 6a), indicating that the lack of LLPS was not due to the degradation and nuclear export of phosphorylated

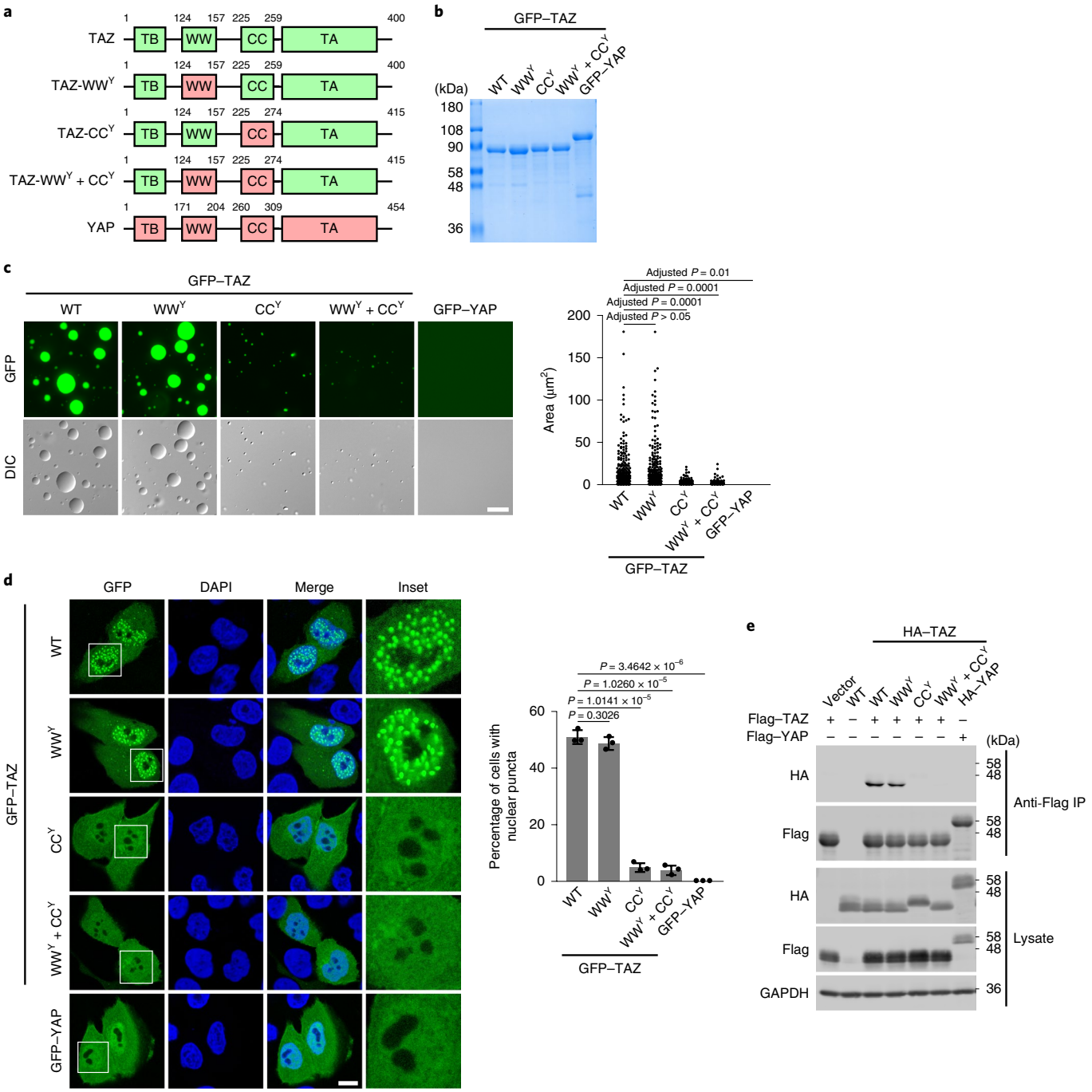

Fig. 4 | The differential ability of TAZ and YAP to undergo phase separation lies in the CC domain. a, Domain structure of TAZ chimaeras. **b**, Coomassie blue staining of various recombinant proteins purified from *Escherichia coli*. **c**, Droplet formation by TAZ chimaeras using the same conditions as described in Fig. 3a. Scale bar, 10 μm. Quantification of the droplets is shown on the right. Data are mean ± s.e.m. Statistical significance was evaluated using one-way ANOVA with Krusk–Wallis test. Droplets in $n = 3$ fields in each group were quantified. **d**, Confocal microscopy images of MCF-10A cells transfected with various chimaeras as indicated. Scale bar, 10 μm. Insets, magnified by 2.94, 2.94, 2.94 and 3.12 times, respectively. Right, quantification of the percentage of cells that displayed nuclear puncta. Data are mean ± s.e.m. *P* values were determined using unpaired two-tailed Student's *t*-tests; 80 transfected cells in each group were quantified; $n = 3$ biologically independent samples. **e**, Flag-tagged WT *TAZ* or *YAP* was cotransfected into HEK293T cells together with HA-tagged *TAZ* mutants or *YAP* as indicated. Dimerization of TAZ or YAP was evaluated using immunoprecipitation with anti-Flag antibodies and detected using western blotting with anti-HA antibodies (top). The abundance of these proteins in the cell lysates was assessed using western blotting (bottom). GAPDH was used as a loading control. The experiments in **b**–**e** were repeated independently three times with similar results. Source data are available online.

TAZ. Ectopic expression of NDR1 or NDR2—two Ser–Thr kinases of the NDR/LATS family that also phosphorylate TAZ[43]—also impaired the ability of TAZ to undergo LLPS (Fig. 6c). Finally, when GFP–TAZ was phosphorylated by LATS2 in an in vitro kinase assay, it exhibited a greatly reduced ability to form droplets in vitro (Fig. 6d). Moreover, the TAZ^{S89A} mutant, which is resistant to LATS2 phosphorylation, displayed moderately enhanced formation of condensates compared with wild-type TAZ (Fig. 6e). This mutant

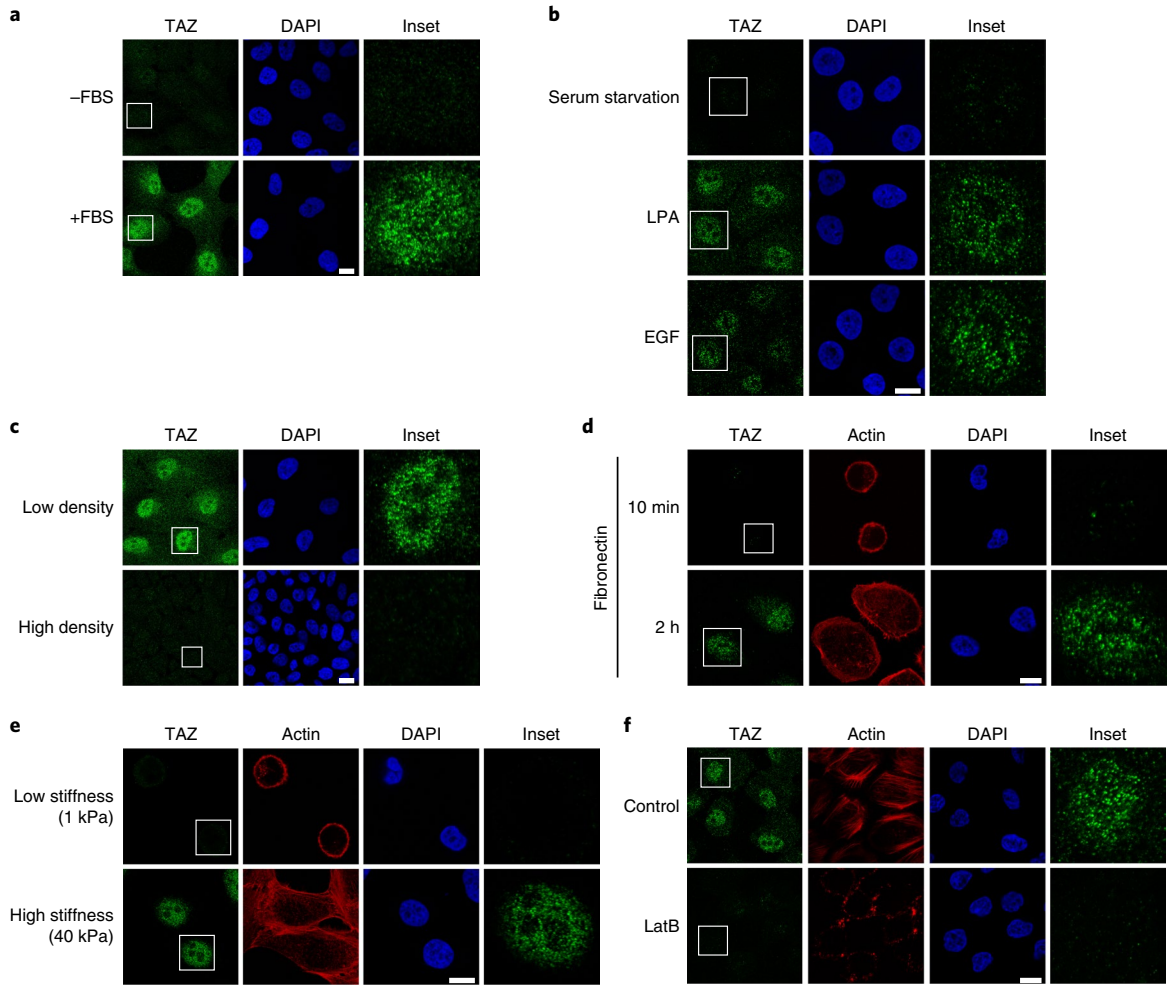

Fig. 5 | Hippo signalling negatively regulates TAZ phase separation. a,**b**, MCF-10A cells were serum-starved for 16 h, treated with 10% FBS (**a**) or 1 μM LPA or 50 ng ml^{-1} EGF (**b**) for 1 h and then analysed using immunostaining with anti-TAZ (green) antibodies. For **a** and **b**, scale bars, 10 μm. Insets, magnification by 4.70 (**a**) and 3.07 (**b**) times. **c**, MCF-10A cells cultured at low or high density were analysed using immunostaining with anti-TAZ antibodies (green). Scale bar, 10 μm. Insets magnification by 4.48 and 5.83 times, respectively. **d**, Serum-starved MCF-10A cells were seeded on fibronectin-coated coverslips for 10 min and 2 h in serum-free medium and were then analysed using immunostaining with anti-TAZ antibodies (green) and Alexa-Fluor-555-conjugated phalloidin (red) for F-actin. Scale bar, 10 μm. Insets, magnification by 4.00 and 3.07 times, respectively. **e**, MCF-10A cells grown on fibronectin-coated polyacrylamide hydrogels with a stiffness of 1 kPa and 40 kPa were analysed using immunostaining with anti-TAZ antibodies (green) and Alexa-Fluor-555-conjugated phalloidin (red) for F-actin. Scale bar, 10 μm. Insets, magnification by 3.33 times. **f**, MCF-10A cells treated with 1 μg ml^{-1} latrunculin B (LatB) for 1 h were analysed using immunostaining with anti-TAZ antibodies (green) and Alexa-Fluor-555-conjugated phalloidin (red) for F-actin. Scale bar, 10 μm. Insets, magnification by 4.00 times. The experiments shown in **a**–**f** were repeated independently three times with similar results.

also exhibited cytoplasmic puncta that colocalized with LATS2 (Extended Data Fig. 6a), suggesting that the cytoplasmic TAZ condensates could be the site of phosphorylation by LATS2. Taken together, these data indicate that the ability of TAZ to undergo LLPS can be inhibited by Hippo signalling through LATS/NDR-kinase-mediated phosphorylation.

TAZ compartmentalizes TEAD and other transcription cofactors in LLPS condensates. Colocalization studies indicated that TAZ condensates did not contain markers of promyelocytic leukemia (PML) bodies, nucleolus or Cajal bodies (Extended Data Fig. 7). We next examined whether the TAZ nuclear puncta contained its DNA-binding cofactor TEAD[8,44,45] and other transcriptional coactivators. When expressed alone, TEAD4 was evenly distributed in the nucleus and did not undergo LLPS either in vivo or in vitro, but was recruited to the TAZ condensates by the ectopically expressed GFP–TAZ (Fig. 7a,b). This recruitment is dependent on the interaction between TAZ and TEAD and the ability of TAZ to undergo LLPS. The TAZ^{S51A} mutant is defective in TEAD binding[46], yet the fraction of this mutant that localized in the nucleus[47] still underwent LLPS. When coexpressed with the TAZ^{S51A} mutant, TEAD was not recruited to the TAZ LLPS, suggesting the importance of the TAZ–TEAD interaction for the localization of TEAD to the TAZ puncta. Deletion of the WW and CC domains of TAZ (ΔWW+ΔCC) not only disrupted TAZ LLPS but also prevented localization of TEAD4 in these puncta, even though this TAZ mutant remained bound to TEAD4 in the nucleus (Fig. 7c), confirming the requirement of TAZ LLPS for recruiting TEAD4. Finally, activation of TAZ, either by serum stimulation or LATS1/2 knockdown, resulted in the recruitment of TEAD to the TAZ LLPS puncta (Fig. 7d, Extended Data Fig. 6b,c). Together, these data suggest that TAZ interacts with TEAD4 and recruits TEAD4 to the liquid droplets.

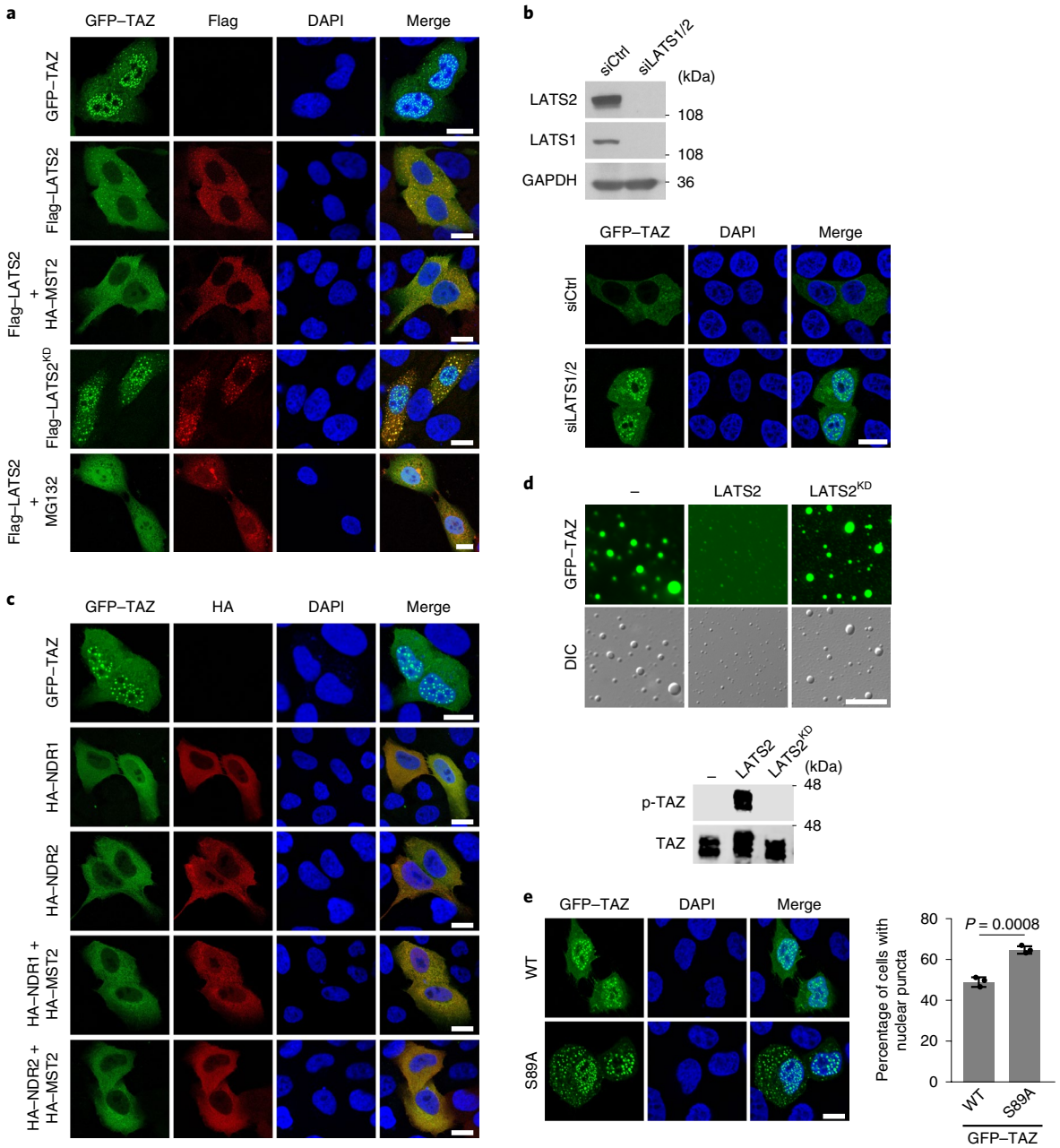

Fig. 6 | Hippo signalling negatively regulates TAZ phase separation through LATS2. a, GFP–TAZ (green) was cotransfected with Flag-tagged WT *LATS2*, either alone or together with *HA–MST2*, or with the kinase inactive *LATS2*^{KD} in the absence of presence of 40 μM MG132 for 6 h. LATS2 localization was detected by immunofluorescence using anti-Flag antibodies (red). Scale bars, 10 μm. **b**, MCF-10A cells transfected with siRNA control (siCtrl) or siRNA targeting *LATS1/2* (siLATS1/2) were analysed using western blotting (top). Localization of GFP–TAZ in these cells at high cell density was examined using confocal microscopy (bottom). Scale bar, 10 μm. **c**, GFP–TAZ (green) was cotransfected with WT *HA–NDR1* or *HA–NDR2*, either alone or together with *HA–MST2*. NDR1/2 localization was detected using immunofluorescence with anti-HA antibodies (red). Scale bars, 10 μm. **d**, In vitro phosphorylation and droplet formation. GFP–TAZ was phosphorylated in an in vitro kinase assay by WT or kinase-inactive LATS2 prepared from transfected HEK293T cells and analysed using a droplet-formation assay. Phosphorylation of TAZ was detected by western blotting using antibodies specific for phosphorylated TAZ (bottom). Top, representative fluorescence and differential interference contrast images of the droplets. Scale bar, 10 μm. **e**, Confocal images of MCF-10A cells transfected with *GFP–TAZ* or *GFP–TAZ*^{S89A}. Scale bar, 10 μm. Right, quantification of the percentage of cells that displayed nuclear puncta. Data are mean ± s.e.m. *P* values were determined using unpaired two-tailed Student's *t*-tests; 80 transfected cells in each group were quantified; $n = 3$ biologically independent samples. The experiments in **a**–**e** were repeated independently three times with similar results. Source data are available online.

The TAZ nuclear condensates were also enriched for components of the transcriptional elongation machinery, CDK9, super-enhancer markers BRD4 and MED1 (Fig. 7e), and the active RNA polymerase II phosphorylated at Ser 2 or Ser 5 of its C-terminal domain (CTD; Fig. 7f), suggesting that the TAZ LLPS puncta are sites of active transcription. Consistent with this, we detected H3K4me3—the actively transcribed chromatin mark—but not the transcriptionally repressive mark H3K9me3 in the TAZ condensates (Fig. 7g). These data support the model that TAZ forms LLPS condensates that are enriched for key transcription factors to enable gene expression.

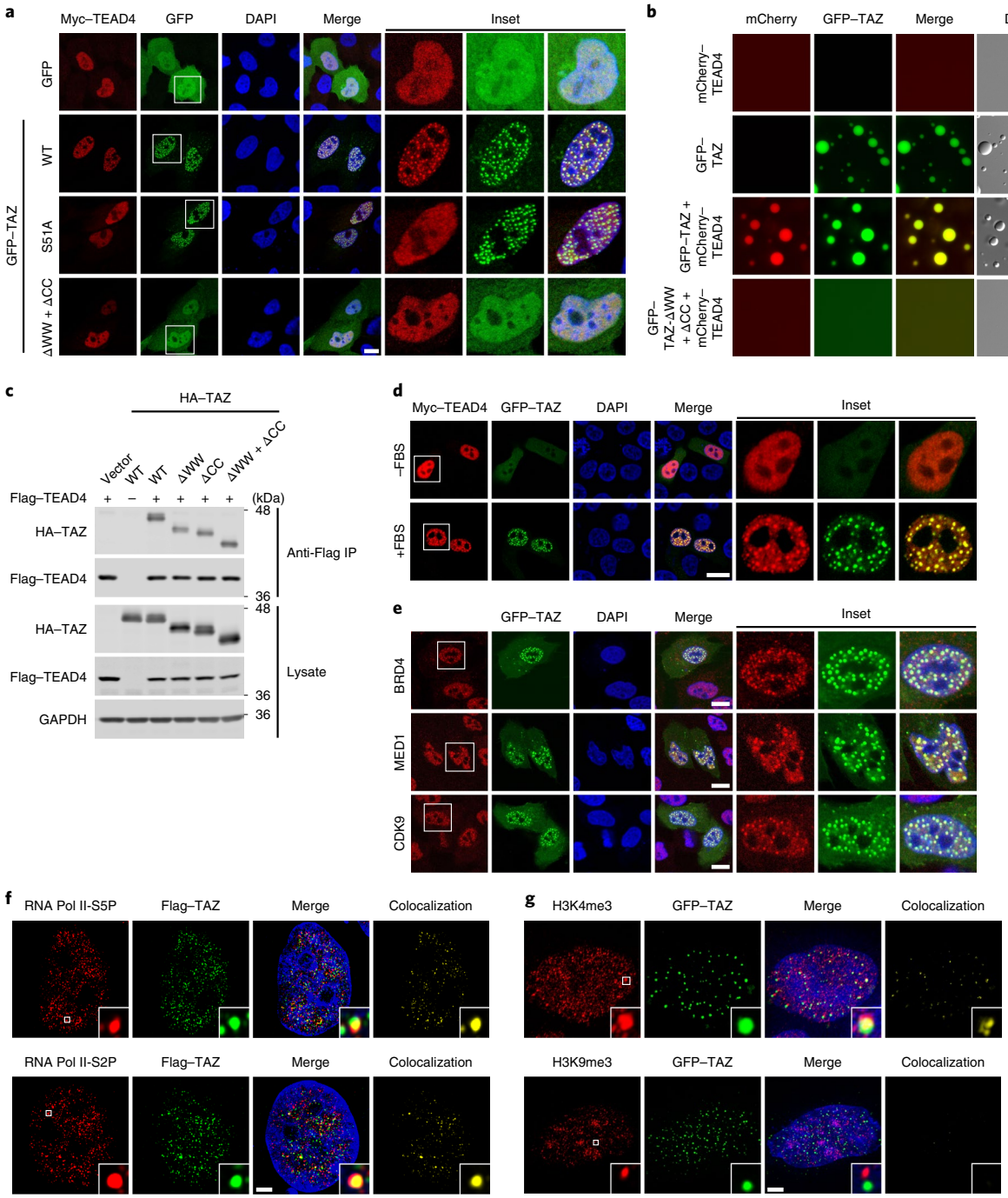

Fig. 7 | TAZ compartmentalizes TEAD and other transcriptional factors to the nuclear puncta. a, *Myc–TEAD4* was cotransfected into MCF-10A cells together with *GFP* vector or WT or mutant *GFP–TAZ* as indicated. TAZ and TEAD4 localization was monitored by GFP fluorescence and using immunofluorescence staining with anti-Myc antibodies (red), respectively. Scale bar, 10 μm. Insets, magnification by 2.96, 2.75, 2.75 and 2.75 times, respectively. **b**, In vitro droplet-formation assay. mCherry–TEAD4 (50 μM) either alone or mixed together with 50 μM WT GFP–TAZ or ΔWW+ΔCC was analysed using a droplet-formation assay under the same conditions as described in Fig. 3c. Scale bar, 10 μm. **c**, The ability of HA-tagged WT or mutant TAZ to interact with Flag–TEAD4 was examined using a co-immunoprecipitation assay with anti-Flag antibodies in the immunoprecipitation (IP), followed by western blotting with anti-HA antibodies (top). The abundance of these proteins in the cell lysates was assessed using western blotting (bottom). **d**, Serum-starved MCF-10A cells transfected with *Myc–TEAD4* and *GFP–TAZ* were treated with 10% FBS for 1 h and processed for immunofluorescence staining using anti-Myc antibodies (red). Scale bar, 10 μm. Inset, magnification by 3.02 times. **e**, Colocalization of BRD4, MED1 or CDK9 with GFP–TAZ in the nuclear puncta in MCF-10A cells. Localization of endogenous BRD4, MED1 and CDK9 was detected by indirect immunofluorescence (red). Scale bars, 10 μm. Insets, magnification by 2.85 times. **f**, Colocalization of active RNA Pol II with Flag–TAZ in the nuclear puncta in MCF-10A cells was detected using immunofluorescence staining with antibodies targeting either the active RNA Pol II, which is phosphorylated at Ser 5 (S5P) or Ser 2 (S2P) in its CTD (red), or Flag (green). The images were captured using super-resolution structured illumination microscopy. Colocalization (yellow) was analysed using Imaris. Scale bar, 2 μm. **g**, Localization of active or repressive histone marks in MCF-10A cells expressing GFP–TAZ was analysed using immunofluorescence staining with anti-H3K4me3 or anti-H3K9me3 antibodies (red). The images were captured using super-resolution structured illumination microscopy. Colocalization (yellow) was analysed using Imaris. Scale bar, 2 μm. The experiments in **a**–**g** were repeated independently three times with similar results. Source data are available online.

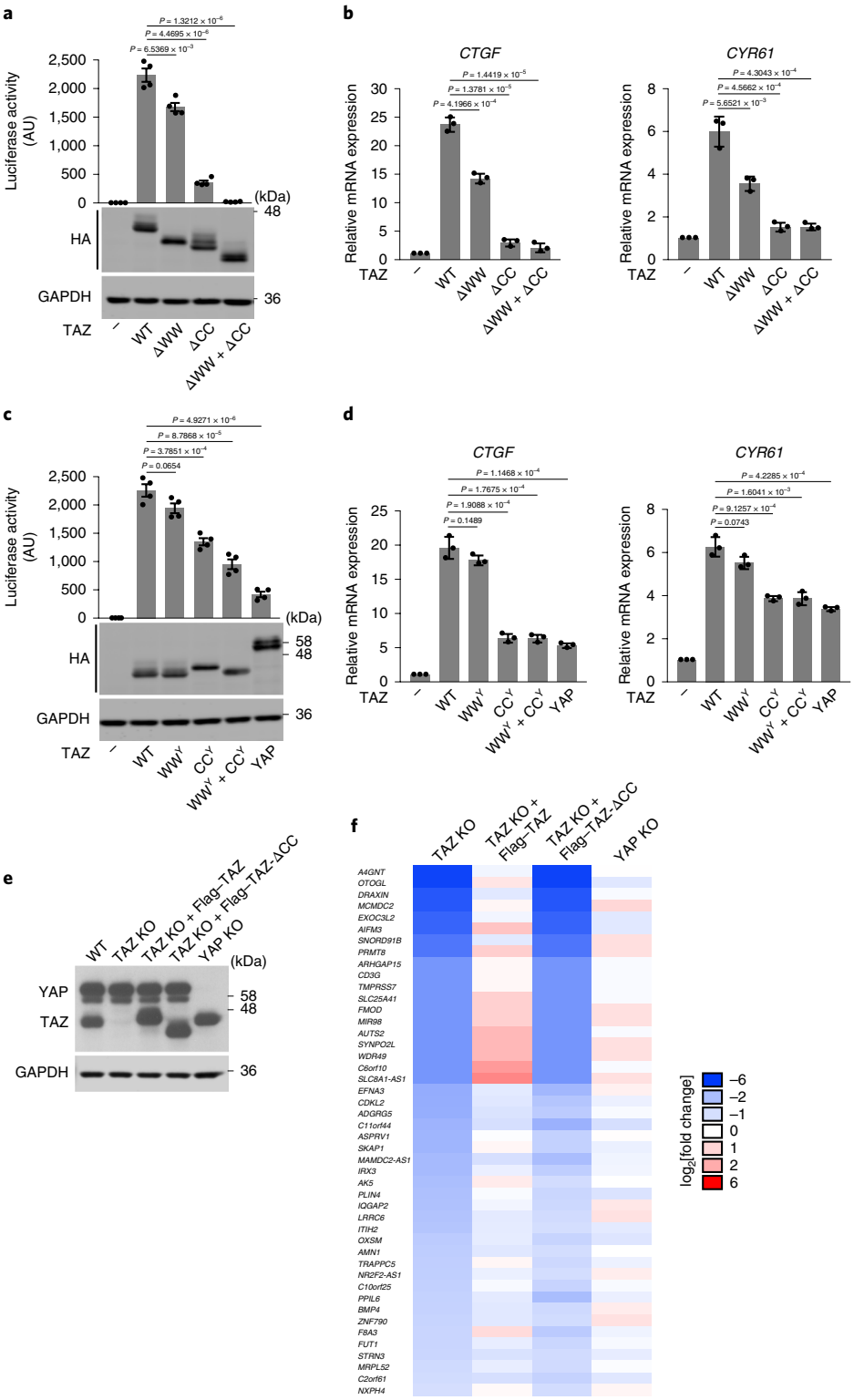

Fig. 8 | Phase separation of TAZ promotes transcription. a,**c**, TAZ-dependent luciferase activity was measured in HEK293T cells expressing 8×GT-IIC-δ51LucII and various TAZ mutants (**a**) or TAZ–YAP chimaeras (**c**). Data are mean ± s.e.m. *P* values were determined using unpaired two-tailed Student's *t*-tests; $n = 4$ biologically independent samples. **b**,**d**, Quantitative PCR with reverse transcription (RT–qPCR) analysis of *CTGF* and *CYR61* mRNA expression in HEK293T cells transfected with various *TAZ* mutants (**b**) or *TAZ–YAP* chimaeras (**d**). Data are mean ± s.e.m. *P* values were determined using unpaired two-tailed Student's *t*-tests; $n = 3$ biologically independent samples. **e**, Analysis of TAZ and YAP expression using western blotting in MDA-MB-231 cells with altered TAZ or YAP expression. GAPDH was used as a loading control. **f**, Heat map summarizing genes that are significantly downregulated in TAZ KO cells, but not in YAP KO cells, using RNA-seq. Genes with the most-reduced expression are indicated in blue, and genes with the most-induced expression are indicated in red. The expression levels of downregulated genes in TAZ KO cells were restored in cells re-expressing Flag–TAZ but not Flag–TAZ$^{\Delta CC}$. The experiments in **a** and **c** were repeated independently four times with similar results. The experiments in **b**, **d** and **e** were repeated independently three times with similar results. Statistical analyses were calculated on the basis of the average numbers from these independent experiments. Source data are available online.

Phase separation promotes transcriptional activation by TAZ. We next examined whether the ability of TAZ to undergo LLPS is required for the transcriptional activity of TAZ using the TAZ ΔCC mutant and TAZ CC^{Y} chimaera that do not form nuclear puncta but are still able to bind to TEAD4 and its regulator LATS2 (Fig. 7c, Extended Data Fig. 8). In both the TAZ-dependent luciferase reporter assay (Fig. 8a) and the experiments measuring the expression of two endogenous TAZ target genes, *CTGF* and *CYR61* (Fig. 8b), deletion of the WW domain alone had little effect on transcription, whereas deletion of the CC domain either individually or together with the WW domain significantly decreased the transcriptional activity of TAZ. Thus, the transcriptional activity of TAZ is correlated with its ability to undergo LLPS.

Under the same experimental conditions, YAP showed lower transcription activity than TAZ[27] (Fig. 8c,d). Interestingly, whereas TAZ-WW^{Y} activated transcription to a similar extent as TAZ, TAZ-CC^{Y} and TAZ-WW^{Y}+CC^{Y} displayed reduced transcriptional activity, similar to YAP (Fig. 8c,d). As YAP and TAZ-CC^{Y} have the ability to activate transcription, albeit at a lower level, we speculated that TAZ LLPS is probably not essential for the basal transcription, but more for insulating the TAZ-specific pathways from those of YAP to establish signalling specificity. To test this, we knocked out TAZ or YAP using CRISPR–Cas9 in MDA-MB-231 cells (Fig. 8e) and compared the gene expression profiles of these cells with the expression profiles of the parental cells using RNA sequencing (RNA-seq). We identified a panel of around 46 genes that are strongly dependent on TAZ, but not on YAP, for expression (Fig. 8f). Reintroduction of WT TAZ, but not of the TAZ ΔCC mutant defective in LLPS, in the TAZ KO cells fully restored expression of these genes (Fig. 8f), strongly supporting the idea that TAZ LLPS is required for TAZ-specific gene expression. Taken together, our data suggest that an important function of TAZ LLPS is to act as hubs for efficient and TAZ-specific transcriptional activation.

Discussion

TAZ and YAP activate the expression of many cellular genes in response to a wide variety of signals derived from cell–cell contact, cell polarity, mechano-transduction, cellular stress and metabolism[48–51]. How these broad-spectrum transcriptional coactivators orchestrate such a diverse array of signals to generate specific downstream outcomes is an important but unanswered question. Here we show that phase separation is an important mechanism that enables TAZ to activate transcription in an efficient and specific manner. Under natural conditions (no crowding agents), TAZ, but not YAP, forms liquid-like droplets both in vitro and in vivo, and these LLPS condensates function as hubs for TAZ to compartmentalize its partner TEAD4, coactivators and core machinery, including BRD4, MED1 and CDK9 to activate the transcription of target genes. This process is negatively regulated by Hippo signalling through phosphorylation by LATS/NDR kinases. Thus, we have identified that LLPS is an important mechanism by which TAZ efficiently engages the transcriptional machinery to stimulate specific gene expression.

YAP differs from TAZ in its ability to phase separate. Cai et al. showed recently that YAP can undergo LLPS in the presence of crowding agent PEG and that the nuclear YAP condensates may be the site of transcription[31]. We found that, under conditions in which TAZ readily phase separated, YAP failed to form LLPS both in vitro or in vivo. YAP was able to form droplets only in the presence of several crowding agents. LLPS is often driven by IDRs or CC domains that mediate oligomerization and/or facilitate multivalent interactions that are necessary for LLPS[52,53]. TAZ and YAP both contain large stretches of IDRs and a CC domain, and it is the CC domain that distinguishes TAZ from YAP in its ability to phase separate. Deleting this domain or substituting it with the YAP CC domain significantly impaired TAZ LLPS and downstream target gene expression. The TAZ CC domain is required for TAZ oligomerization and additional multivalent interactions with other proteins. These interactions probably involve hydrophobic residues, as TAZ LLPS is enhanced by increasing salt concentrations and temperature—conditions that favour hydrophobic interactions. The TAZ CC domain has been previously reported to mediate interaction with the Smad2/3–Smad4 complex to promote their nuclear translocation[54]. However, evidence for the role of the TAZ CC domain in transcriptional activation has been lacking. Here we demonstrated a role of the CC domain in transcriptional activation through the induction of LLPS.

The distinct ability of TAZ and YAP to undergo LLPS leads to important differences in the transcriptional outcomes. Gene expression profiling analyses have shown that, although many genes can be activated by both TAZ and YAP, a substantial subset of genes are differentially induced by either TAZ or YAP, often in a cell- or tissue-specific manner[16,55]. How TAZ and YAP achieve this transcription specificity has not been well defined. Kaan et al. suggest that, in contrast to the YAP–TEAD dimer, TAZ–TEAD can form a hetero-tetramer, and this unique structural feature may affect DNA-target selectivity and transcription of some target genes[27]. Our results suggest that phase separation could be an important mechanism that enables physical separation of TAZ-specific signalling pathways from those of YAP and, therefore, provides pathway specificity. Indeed, our RNA-seq results showing that a panel of TAZ-specific genes requires LLPS for activation strongly support this notion.

LLPS is emerging as a key mechanism for transcriptional regulation. General transcription elongation factor P-TEFb, transcription initiation factors TAF15 and FUS[56,57], stem-cell-specific transcription factors OCT4, MYC and SOX2[13], as well as transcription coactivators BRD4 and MED1[25] have all been shown to undergo phase separation to cluster in discrete membraneless condensates that function as hubs to enable efficient and dynamic regulation of transcription and RNA processing. Here we provide evidence that the signalling-pathway-specific transcription coactivator TAZ uses a similar LLPS mechanism through multivalent protein–protein interactions to regulate downstream gene expression. TAZ LLPS can achieve three goals. First, by concentrating TEAD4, BRD4 and MED1, and the general elongation factor P-TEFb in one compartment, TAZ LLPS enables more efficient transcription reactions. Second, TAZ LLPS physically sequesters the TAZ-specific pathway away from YAP to enable TAZ-specific downstream outcomes. Finally, TAZ LLPS spatially insulates TAZ from its upstream regulators LATS1 and LATS2 to prevent inactivation. As TAZ is a critical regulator of cell proliferation, survival, differentiation and transformation[12,58], and its upregulation in human cancers can promote transcriptional addiction, understanding the role of phase separation in its mechanism of action may provide therapeutic targets for cancer in humans.

Online content

Any methods, additional references, Nature Research reporting summaries, source data, extended data, supplementary information, acknowledgements, peer review information; details of author contributions and competing interests; and statements of data and code availability are available at https://doi.org/10.1038/s41556-020-0485-0.

Received: 28 May 2019; Accepted: 14 February 2020;
Published online: 23 March 2020

References

1. Pan, D. The Hippo signaling pathway in development and cancer. *Dev. Cell* **19**, 491–505 (2010).
2. Ma, S., Meng, Z., Chen, R. & Guan, K. L. The Hippo pathway: biology and pathophysiology. *Annu. Rev. Biochem.* **88**, 577–604 (2018).
3. Tapon, N. & Harvey, K. F. The Hippo pathway—from top to bottom and everything in between. *Semin. Cell Dev. Biol.* **23**, 768–769 (2012).

4. Badouel, C. & McNeill, H. SnapShot: the Hippo signaling pathway. *Cell* **145**, 484 (2011).
5. Schroeder, M. C. & Halder, G. Regulation of the Hippo pathway by cell architecture and mechanical signals. *Semin. Cell Dev. Biol.* **23**, 803–811 (2012).
6. Yu, F. X. & Guan, K. L. The Hippo pathway: regulators and regulations. *Genes Dev.* **27**, 355–371 (2013).
7. Dong, J. X. et al. Elucidation of a universal size-control mechanism in *Drosophila* and mammals. *Cell* **130**, 1120–1133 (2007).
8. Ota, M. & Sasaki, H. Mammalian Tead proteins regulate cell proliferation and contact inhibition as transcriptional mediators of Hippo signaling. *Development* **135**, 4059–4069 (2008).
9. Enderle, L. & McNeill, H. Hippo gains weight: added insights and complexity to pathway control. *Sci. Signal.* **6**, re7 (2013).
10. Shreberk-Shaked, M. & Oren, M. New insights into YAP/TAZ nucleo-cytoplasmic shuttling: new cancer therapeutic opportunities? *Mol. Oncol.* **13**, 1335–1341 (2019).
11. Galli, G. G. et al. YAP drives growth by controlling transcriptional pause release from dynamic enhancers. *Mol. Cell* **60**, 328–337 (2015).
12. Zanconato, F. et al. Transcriptional addiction in cancer cells is mediated by YAP/TAZ through BRD4. *Nat. Med.* **24**, 1599–1610 (2018).
13. Boija, A. et al. Transcription factors activate genes through the phase-separation capacity of their activation domains. *Cell* **175**, 1842–1855 (2018).
14. Chan, S. W. et al. A role for TAZ in migration, invasion, and tumorigenesis of breast cancer cells. *Cancer Res.* **68**, 2592–2598 (2008).
15. Cordenonsi, M. et al. The Hippo transducer TAZ confers cancer stem cell-related traits on breast cancer cells. *Cell* **147**, 759–772 (2011).
16. Plouffe, S. W. et al. The Hippo pathway effector proteins YAP and TAZ have both distinct and overlapping functions in the cell. *J. Biol. Chem.* **293**, 11230–11240 (2018).
17. Xin, M. et al. Hippo pathway effector Yap promotes cardiac regeneration. *Proc. Natl Acad. Sci. USA* **110**, 13839–13844 (2013).
18. Nishioka, N. et al. The Hippo signaling pathway components Lats and Yap pattern Tead4 activity to distinguish mouse trophectoderm from inner cell mass. *Dev. Cell* **16**, 398–410 (2009).
19. Morin-Kensicki, E. M. et al. Defects in yolk sac vasculogenesis, chorioallantoic fusion, and embryonic axis elongation in mice with targeted disruption of Yap65. *Mol. Cell. Biol.* **26**, 77–87 (2006).
20. Hossain, Z. et al. Glomerulocystic kidney disease in mice with a targeted inactivation of Wwtr1. *Proc. Natl Acad. Sci. USA* **104**, 1631–1636 (2007).
21. Passaniti, A., Brusgard, J. L., Qiao, Y. T., Sudol, M. & Finch-Edmondson, M. Roles of RUNX in Hippo pathway signaling. *Adv. Exp. Med. Biol.* **962**, 435–448 (2017).
22. Zhao, B. et al. TEAD mediates YAP-dependent gene induction and growth control. *Gene Dev.* **22**, 1962–1971 (2008).
23. Zhao, B., Tumaneng, K. & Guan, K. L. The Hippo pathway in organ size control, tissue regeneration and stem cell self-renewal. *Nat. Cell Biol.* **13**, 877–883 (2011).
24. Alberti, S., Gladfelter, A. & Mittag, T. Considerations and challenges in studying liquid-liquid phase separation and biomolecular condensates. *Cell* **176**, 419–434 (2019).
25. Sabari, B. R. et al. Coactivator condensation at super-enhancers links phase separation and gene control. *Science* **361**, eaar3958 (2018).
26. Lu, H., Liu, R. & Zhou, Q. Balanced between order and disorder: a new phase in transcription elongation control and beyond. *Transcription* **10**, 157–163 (2019).
27. Kaan, H. Y. K. et al. Crystal structure of TAZ-TEAD complex reveals a distinct interaction mode from that of YAP-TEAD complex. *Sci. Rep.* **7**, 2035 (2017).
28. Piccolo, S., Dupont, S. & Cordenonsi, M. The biology of Yap/Taz: Hippo signaling and beyond. *Physiol. Rev.* **94**, 1287–1312 (2014).
29. Hyman, A. A., Weber, C. A. & Juelicher, F. Liquid-liquid phase separation in biology. *Annu. Rev. Cell Dev. Biol.* **30**, 39–58 (2014).
30. Boeynaems, S. et al. Protein phase separation: a new phase in cell biology. *Trends Cell Biol.* **28**, 420–435 (2018).
31. Cai, D. et al. Phase separation of YAP reorganizes genome topology for long-term YAP target gene expression. *Nat. Cell Biol.* **21**, 1578–1589 (2019).
32. Henis, Y. I., Rotblat, B. & Kloog, Y. FRAP beam-size analysis to measure palmitoylation-dependent membrane association dynamics and microdomain partitioning of Ras proteins. *Methods* **40**, 183–190 (2006).
33. Eisenberg, S., Giehl, K., Henis, Y. I. & Ehrlich, M. Differential interference of chlorpromazine with the membrane interactions of oncogenic K-Ras and its effects on cell growth. *J. Biol. Chem.* **283**, 27279–27288 (2008).
34. Shvartsman, D. E. et al. Src kinase activity and SH2 domain regulate the dynamics of Src association with lipid and protein targets. *J. Cell Biol.* **178**, 675–686 (2007).
35. Wolfenson, H. et al. A role for the juxtamembrane cytoplasm in the molecular dynamics of focal adhesions. *PLoS ONE* **4**, e4304 (2009).
36. Molliex, A. et al. Phase separation by low complexity domains promotes stress granule assembly and drives pathological fibrillization. *Cell* **163**, 123–133 (2015).
37. Nott, T. J. et al. Phase transition of a disordered nuage protein generates environmentally responsive membraneless organelles. *Mol. Cell* **57**, 936–947 (2015).
38. Fan, R., Kim, N. G. & Gumbiner, B. M. Regulation of Hippo pathway by mitogenic growth factors via phosphoinositide 3-kinase and phosphoinositide-dependent kinase-1. *Proc. Natl Acad. Sci. USA* **110**, 2569–2574 (2013).
39. Kim, N. G. & Gumbiner, B. M. Adhesion to fibronectin regulates Hippo signaling via the FAK-Src-PI3K pathway. *J. Cell Biol.* **210**, 503–515 (2015).
40. Totaro, A., Panciera, T. & Piccolo, S. YAP/TAZ upstream signals and downstream responses. *Nat. Cell Biol.* **20**, 888–899 (2018).
41. Yu, F. X. et al. Regulation of the Hippo-YAP pathway by G-protein-coupled receptor signaling. *Cell* **150**, 780–791 (2012).
42. Panciera, T., Azzolin, L., Cordenonsi, M. & Piccolo, S. Mechanobiology of YAP and TAZ in physiology and disease. *Nat. Rev. Mol. Cell Biol.* **18**, 758–770 (2017).
43. Hergovich, A. The roles of NDR protein kinases in Hippo signalling. *Genes* **7**, 21 (2016).
44. Chan, S. W. et al. TEADs mediate nuclear retention of TAZ to promote oncogenic transformation. *J. Biol. Chem.* **284**, 14347–14358 (2009).
45. Noland, C. L. et al. Palmitoylation of TEAD transcription factors is required for their stability and function in Hippo pathway signaling. *Structure* **24**, 179–186 (2016).
46. Zhang, H. et al. TEAD transcription factors mediate the function of TAZ in cell growth and epithelial-mesenchymal transition. *J. Biol. Chem.* **284**, 13355–13362 (2009).
47. Rausch, V. et al. The Hippo pathway regulates caveolae expression and mediates flow response via caveolae. *Curr. Biol.* **29**, 242–255 (2019).
48. Misra, J. R. & Irvine, K. D. The Hippo signaling network and its biological functions. *Annu. Rev. Genet.* **52**, 65–87 (2018).
49. Zhang, L., Yue, T. & Jiang, J. Hippo signaling pathway and organ size control. *Fly* **3**, 68–73 (2009).
50. Gill, M. K. et al. A feed forward loop enforces YAP/TAZ signaling during tumorigenesis. *Nat. Commun.* **9**, 3510 (2018).
51. Richardson, H. E. & Portela, M. Tissue growth and tumorigenesis in *Drosophila*: cell polarity and the Hippo pathway. *Curr Opin. Cell Biol.* **48**, 1–9 (2017).
52. Zeng, M. et al. Phase transition in postsynaptic densities underlies formation of synaptic complexes and synaptic plasticity. *Cell* **166**, 1163–1175 (2016).
53. Fang, X. et al. *Arabidopsis* FLL2 promotes liquid-liquid phase separation of polyadenylation complexes. *Nature* **569**, 265–269 (2019).
54. Varelas, X. et al. TAZ controls Smad nucleocytoplasmic shuttling and regulates human embryonic stem-cell self-renewal. *Nat. Cell Biol.* **10**, 837–848 (2008).
55. Zhang, J. M. et al. YAP-dependent induction of amphiregulin identifies a non-cell-autonomous component of the Hippo pathway. *Nat. Cell Biol.* **11**, 1444–1450 (2009).
56. Kwon, I. et al. Phosphorylation-regulated binding of rna polymerase ii to fibrous polymers of low-complexity domains. *Cell* **155**, 1049–1060 (2013).
57. Kato, M. et al. Cell-free formation of RNA granules: low complexity sequence domains form dynamic fibers within hydrogels. *Cell* **149**, 753–767 (2012).
58. Hagenbeek, T. J. et al. The Hippo pathway effector TAZ induces TEAD-dependent liver inflammation and tumors. *Sci. Signal.* **11**, eaaj1757 (2018).

Methods

Plasmids, antibodies and reagents. The GFP–TAZ and GFP–YAP constructs were generated by PCR and sub-cloned into the pEGFP-C1 vector (Clontech) or pGFP-2×Strep vector, provided by Q. Zhou (University of California, Berkeley). Mutant GFP–TAZ containing various truncations and mutations in the TAZ molecule were generated using PCR and similarly cloned into the above vectors. The chimeric GFP–TAZ molecules containing the substituted YAP WW (WW^Y: amino acids 171–204), CC (CC^Y: amino acids 260–309), or both WW and CC domains (WW^Y+CC^Y) were generated by PCR based on GFP–TAZ. Chimeric GFP–YAP containing the substituted TAZ WW (WW^T, amino acids 124–157), CC (CC^T, amino acids 225–259), or both WW and CC domains (WW^T+CC^T) were generated by PCR based on GFP–YAP. The mCherry–TEAD4 construct was generated by PCR and subcloned into the pHis-mCherry vector provided by Q. Zhou (University of California, Berkeley). cDNAs of TAZ, YAP, LATS2, LATS2 KD, TEAD4 and MST2 were provided by K.-L. Guan (University of California, San Diego) and A. Mauviel (Curie Institute).

The following antibodies and reagents were purchased from commercial sources: anti-TAZ (BD Pharmingen, 560235, M2–616, 1:100); anti-GAPDH (Santa Cruz, sc-25778, FL-335, 1:1,000); anti-Myc (Cell Signaling Technology, 2276, 9B11, 1:200); anti-MED1 (Santa Cruz, sc-8998, M-255, 1:100); anti-PML (Santa Cruz, sc-966, PG-M3, 1:100); anti-coilin (Santa Cruz, sc-55594, F-7, 1:100); anti-fibrillarin (Santa Cruz, sc-377340, G-8, 1:100); anti-RNA Pol II-S2P (Millipore, 04–1571, 3E10, 1:200); anti-RNA Pol II-S5P (Millipore, 04–1572, 3E8, 1:200); anti-H3K4me3 (Active Motif, 39160, 1:400); anti-H3K9me3 (Active Motif, 39162, 1:400); anti-Flag (Sigma, F3165, M2, 1:100 or 1:1,000); anti-Flag (Sigma, F7425, 1:1,000), anti-YAP/TAZ (Santa Cruz, sc-101199, 63.7, 1:1,000); anti-LATS1 (Cell Signaling Technology, 3477, C66B5, 1:1,000); anti-LATS2 (Bethyl Laboratories, A300–479A, 1:1,000); anti-glutathione *S*-transferase (GST) (Cell Signaling Technology, 2624, 26H1, 1:1,000); Alexa Fluor 555 Phalloidin (Thermo Fisher Scientific, A34055, 1:100); MG-132 (Selleck); LPA (Tocris Bioscience); EGF (PeproTech); fibronectin (Sigma); 1,6-hexanediol (Sigma); polyacrylamide hydrogels of 1 kPa and 40 kPa stiffness (Matrigen); Ficoll (Grainger); dextran (Sigma); PEG-1000 (Sigma); PEG-8000 (Sigma); and BSA (Sigma).

Antibodies against HA (1:100 or 1:1,000), CDK9 (1:400) and BRD4 (1:400) were generated as described previously[59].

Protein expression and purification. Plasmids containing Strep-GFP-, His-mCherry- or GST-tagged genes were transformed into *E. coli* BL21 cells. After induction with isopropyl-β-D-thiogalactoside, bacteria lysates in buffer (50 mM Tris-HCl pH 7.5, 500 mM NaCl, 1 mM dithiothreitol (DTT) and 1% Triton X-100) were sonicated, and the Strep–GFP-fusion proteins were purified using the Strep-Tactin Superflow beads (IBA). The His–mCherry-fusion proteins were purified using a Ni-NTA column (Thermo Fisher Scientific). The GST and GST-fusion proteins were purified using Glutathione Sepharose beads (GE Healthcare). The eluted proteins were dialysed in 1 l dialysed buffer (20 mM Tris-HCl pH 7.5, 37.5 mM NaCl and 1 mM DTT) overnight at 4 °C and concentrated with Amicon Ultra Centrifugal Filters (Millipore).

Droplet-formation assay. Purified proteins were diluted to varying concentrations in buffer containing 20 mM Tris-HCl pH 7.5 and 1 mM DTT with the indicated salt concentrations. Protein solution (5 µl) was loaded onto a glass slide, covered with a coverslip and imaged using an AxioObserver Z1 inverted microscope (Zeiss). The sizes of the droplets in 3 166×124 µm^2 fields were quantified using ImageJ (NIH).

Cell culture, transfection, infection and RNA interference. HEK293T, HeLa and MDA-MB-231 cells were cultured in DMEM (Invitrogen) containing 10% FBS (HyClone) and 50 µg ml^{-1} penicillin–streptomycin (Pen–Strep). MCF10A cells were cultured in DMEM/F12 (Invitrogen) supplemented with 5% horse serum (Invitrogen), 20 ng ml^{-1} EGF, 0.5 µg ml^{-1} hydrocortisone, 10 µg ml^{-1} insulin, 100 ng ml^{-1} cholera toxin and 50 µg ml^{-1} Pen–Strep. All of the cell lines were authenticated at the UC Berkeley Cell Culture Facility by single-nucleotide polymorphism testing and were confirmed as negative for mycoplasma.

Transfection of cells was performed using Lipofectamine 3000 (Thermo Fisher Scientific) according to the manufacturer's instructions. The CRISPR–Cas9 system was used to delete TAZ or YAP in MDA-MB-231 cells as previously described[60], using lentiCRISPR v2 (Addgene plasmid 52961). The stable TAZ KO cells expressing Flag–TAZ or Flag–$TAZ^{ΔCC}$ were generated by retroviral infection as described previously[61]. RNA interference was performed using Lipofectamine RNAiMAX (Thermo Fisher Scientific) according to the manufacturer's instructions. The following siRNAs obtained from Dharmacon were used: siGENOME SMARTpool Human LATS2 (M-003865–02), siGENOME SMARTpool Human LATS1 (M-004632–00) and Accell Control Pool Non-Targeting (D-001910–10–05).

Immunofluorescence staining and live-cell imaging. Cells were seeded on glass coverslips, fixed with 4% paraformaldehyde PBS for 15 min, blocked in buffer containing 5% FBS and 0.3% Triton X-100 in PBS for 1 h and incubated with primary antibodies overnight at 4 °C. After washes, cells were incubated with Alexa-Fluor-488- or 555-conjugated secondary antibodies (Thermo Fisher Scientific) for 1 h at room temperature. The coverslips were mounted on glass slides in VECTASHIELD Antifade Mounting Medium with DAPI (Vector Laboratories) and sealed. To detect TAZ expression in human tissue samples, a paraffin-embedded human breast tissue array (US Biomax, BR6161) was deparaffinized, hydrated, heated in retrieval buffer (10 mM sodium citrate pH 6.0) for 10 min for antigen retrieval and then incubated with TAZ antibodies (Sigma, HPA007415, 1:100). Immunofluorescence was detected using a Zeiss LSM 710 confocal microscope or Zeiss Elyra PS1 super-resolution structured illumination microscope. Colocalization of green and red channels was performed using Imaris (Bitplane). The age, gender and diagnosis information of the patients is available at company's website: https://www.biomax.us/tissue-arrays/Breast/BR6161.

Live-cell imaging was performed as previously described[59]. In brief, MCF-10A cells transfected with *GFP–TAZ* construct were seeded on LabTek chambered slides (Nunc) and examined under a Nikon Spinning Disk confocal microscope. During image acquisition, cells were incubated in an equilibrated observation chamber at 37 °C with 5% CO_2. Images were acquired at intervals of 30 s and were analysed with ImageJ to identify fusion events.

FRAP and FRAP beam-size analysis. HeLa cells grown on glass coverslips in 6-well plates were transfected with 2 µg per well of *GFP–TAZ* and analysed through quantitative FRAP studies 24 h after transfection as described previously[32,62]. Measurements were performed at 22 °C in Hank's balanced salt solution supplemented with 20 mM HEPES pH 7.2. An argon-ion laser beam (Innova 70C; Coherent) was focused through a fluorescence microscope (Axio Imager.D1, Carl Zeiss MicroImaging) to a spot with a Gaussian radius (ω) of 0.77 ± 0.03 µm (plan apochromat ×63/1.4 NA oil-immersion objective) or 1.17 ± 0.05 µm (C apochromat ×40/1.2 NA water-immersion objective)[33]. The ratio between the bleach areas ($\omega^2(\times40)/\omega^2(\times63)$) was 2.28 ± 0.05 ($n = 59$; s.e.m. was calculated using bootstrap analysis as described below). After a brief measurement at monitoring intensity (488 nm, 1 µW), a 5 mW pulse (5–10 ms) bleached 60–75% of the fluorescence in the illuminated region, and recovery was followed by the monitoring beam. The characteristic fluorescence recovery time (τ) and mobile fraction (R_f) were extracted by nonlinear regression analysis, fitting to a lateral diffusion process[32]. The statistical differences between τ values measured with the same beam sizes were evaluated using Student's *t*-tests. To compare the ratio measurements ($\tau(\times40)/\tau(\times63)$ and $\omega^2(\times40)/\omega^2(\times63)$), we used bootstrap analysis, which is preferable for comparison between ratios[63], as described previously[62], using 1,000 bootstrap samples.

Immunoprecipitation, GST pull-down and immunoblotting. Immunoprecipitation, GST pull-down and immunoblotting were performed as previously described[61]. In brief, cells were lysed in lysis buffer (50 mM HEPES pH 7.5, 150 mM NaCl, 1 mM EDTA, 1% NP-40, 10 mM pyrophosphate, 10 mM glycerophosphate, 50 mM NaF, 1.5 mM Na_3VO_4, protease inhibitor cocktail (Roche) and 1 mM phenylmethylsulfonyl fluoride), and clarified cell lysates were analysed using immunoprecipitation with anti-Flag M2 agarose beads (Sigma). For GST pull-down assays, purified GST or GST-fusion proteins were incubated with clarified cell lysates at 4 °C for 4 h, followed by incubation with Glutathione Sepharose for an additional 2 h. Proteins bound to Glutathione Sepharose were eluted, resolved using SDS–PAGE and detected by western blotting.

In vitro kinase assay. Flag–LATS2 or Flag–$LATS2^{KD}$ was purified from transfected HEK293T cells, eluted as described previously[61] and incubated with GFP–TAZ immobilized on the Strep-Tactin Superflow beads in kinase buffer (10 mM $MgCl_2$, 50 Mm NaCl, 1 mM DTT, 50 mM HEPES pH 7.4) containing 5 mM ATP at room temperature for 12 h. After washing, the phosphorylated GFP–TAZ were eluted from the beads using 10 µl elution buffer (20 mM Tris-HCl pH 7.5, 37.5 mM NaCl, 1 mM DTT and 1 mM desthiobiotin).

Luciferase assay. A total of 2.5 µg DNA (including 50 ng of 8×GT-IIC-δ51LucII Luciferase reporter construct and the indicated plasmids) was transiently transfected into HEK293T cells using Lipofectamine 2000. The luciferase activity was measured at 36 h after transfection as described previously[61,64].

RNA extraction, reverse transcription and qPCR. Total RNA was extracted using TRIzol Reagent (Ambion). RNA (1 µg) was reverse-transcribed using the SuperScript III First-Strand Synthesis System (Thermo Fisher Scientific). The resulting cDNA was analysed using RT–qPCR using the DyNAmo HS SYBR Green qPCR Kits (Thermo Fisher Scientific) and the Bio-Rad real-time PCR system (Bio-Rad), with *β-actin* as a control. The following primers were used: *β-actin*, forward: GCCGACAGGATGCAGAAGGAGATCA, reverse: AAGCATTTGCGGTGGACGATGGA; *CTGF*, forward: CCAATGACAACGCCTCCTG, reverse: TGGTGCAGCCAGAAAGCTC; *CYR61*, forward: AGCCTCGCATCCTATACAACC, reverse: TTCTTTCACAAGGCGGCACTC.

RNA-seq and bioinformatics analysis. Total cellular RNAs were extracted using TRIzol, and cDNA libraries were prepared using high-quality RNA (RNA integrity number > 7). RNA-seq was performed by Novogene. In brief, the libraries were

individually barcoded and run on a single lane of an Illumina NovaSeq system yielding 150-bp paired-end (PE150) reads. The reads were aligned to the hg19 reference genome using STAR v.2.5 (ref. [65]). Only uniquely mapped reads were retained for further analysis. The number of reads for each gene was counted using HTSeq v.0.6.1 (ref. [66]) according to Gencode human annotation release 24. For each sequenced library, the read counts were adjusted using the edgeR program package through one scaling normalized factor. Differential expression analysis of two groups was performed using the edgeR v.3.16.5R package. The *P* values were adjusted using the Benjamini–Hochberg method. Genes with an adjusted $P < 0.005$ and absolute $\log_2$[fold change] > 1 were considered to be significantly differentially expressed.

Statistics and reproducibility. All data were derived from at least three independent experiments and are presented as means ± s.e.m. unless otherwise noted in the figure legend. Comparisons among groups were performed using one-way ANOVA with Krusk–Wallis test or Student's *t*-tests with GraphPad Prism 7. FRAP beam-size ratio measurements used bootstrap analysis—which is preferable for comparison between ratios[63], as described previously[6]—using 1,000 bootstrap samples. All attempts at replication were successful with similar results.

Reporting Summary. Further information on research design is available in the Nature Research Reporting Summary linked to this article.

Data availability

Source data for Figs. 1–4 and 6–8 and Extended Data Figs. 1, 3, 4 and 8 are available online. The RNA-seq data are available in the Gene Expression Omnibus (GEO) with the accession number GSE142474. All other data supporting the findings of this study are available from the corresponding author on reasonable request.

References

59. Lu, H. et al. Phase-separation mechanism for C-terminal hyperphosphorylation of RNA polymerase II. *Nature* **558**, 318–323 (2018).
60. Plouffe, S. W. et al. Characterization of Hippo pathway components by gene inactivation. *Mol. Cell* **64**, 993–1008 (2016).
61. Zhu, Q. et al. SnoN antagonizes the Hippo kinase complex to promote TAZ signaling during breast carcinogenesis. *Dev. Cell* **37**, 399–412 (2016).
62. Eisenberg, S. et al. Raft protein clustering alters N-Ras membrane interactions and activation pattern. *Mol. Cell. Biol* **31**, 3938–3952 (2011).
63. Efron, B. & Tibshirani, R. in *An Introduction to Bootstrap* (eds Cox, D. R. et al.) 124–130 (Chapman & Hall, 1993).
64. Rashidian, J. et al. Ski regulates Hippo and TAZ signaling to suppress breast cancer progression. *Sci. Signal.* **8**, ra14 (2015).
65. Dobin, A. et al. STAR: ultrafast universal RNA-seq aligner. *Bioinformatics* **29**, 15–21 (2013).
66. Anders, S., Pyl, P. T. & Huber, W. HTSeq–a Python framework to work with high-throughput sequencing data. *Bioinformatics* **31**, 166–169 (2015).

Acknowledgements

We thank K.-L. Guan and A. Mauviel for providing cDNAs of components of the Hippo pathway and H. Sasaki for the 8xGT-IIC-δ51LucII construct; J. He for technical assistance and Q. Zhu for helpful suggestions, discussions and help with experimental procedures; and D. Schichnes and S. Ruzin at the CNR biological imaging facility at the University of California, Berkeley for assistance with microscopy. This study was supported by DOD/US Army Medical Research And Materiel Command W81XWH-15-1-0068 (to K.L. and Q.Z.), a Tel Aviv University-University of California Berkeley collaborative research grant (to Y.I.H. and K.L.), and NIH R01AI41757 (to Q.Z.). Y.I.H. is an incumbent of the Zalman Weinberg Chair in Cell Biology. Y.L. is supported by the Berkeley Scholars program, and T.W. was supported by the China Scholarship Council.

Author contributions

Y.L., T.W. and K.L. designed the research. Y.L. performed in vivo experiments. T.W. performed in vitro experiments. Y.I.H. designed and O.G. performed FRAP experiments. Y.L., T.W., H.L., Y.I.H., Q.Z. and K.L. analysed data and wrote the paper. K.L. conceived and directed the project. All of the authors discussed the results and commented on the manuscript.

Competing interests

The authors declare no competing interests.

Additional information

Extended data is available for this paper at https://doi.org/10.1038/s41556-020-0485-0.

Supplementary information is available for this paper at https://doi.org/10.1038/s41556-020-0485-0.

Correspondence and requests for materials should be addressed to K.L.

Reprints and permissions information is available at www.nature.com/reprints.

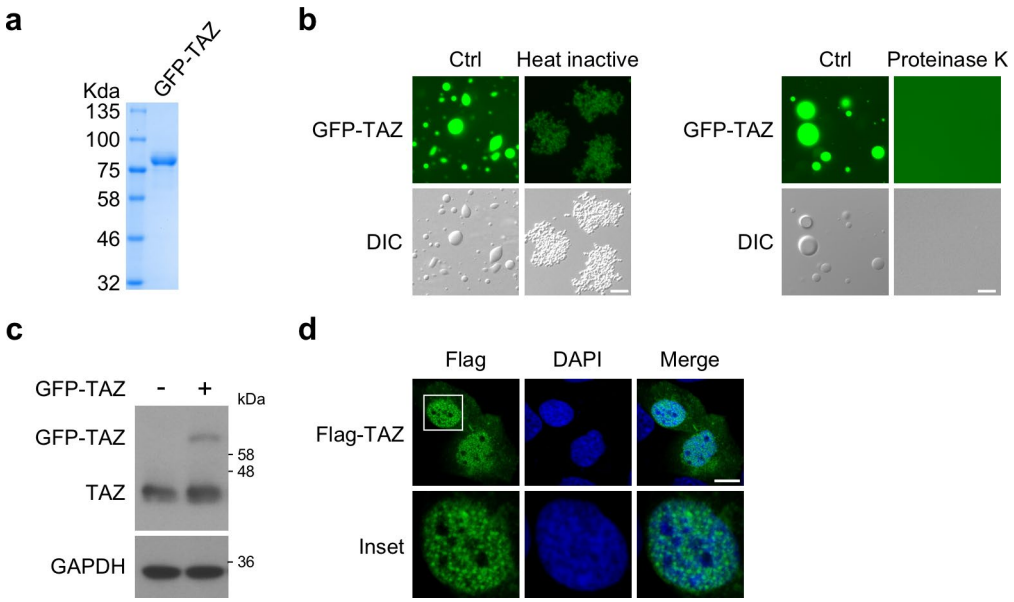

Extended Data Fig. 1 | Regulation of TAZ droplet formation *in vitro* and nuclear puncta formation *in vivo*. a, GFP-TAZ purified from *E. coil* were analysed by SDS-PAGE and visualized by Coomassie blue staining. **b**. 50 μM GFP-TAZ were heated-inactivated (5 min at 95 °C and immediately put on ice for 5 min) or treated with 100 μg/ml Proteinase K for 30 min at 40 °C, and then subjected to droplet formation assay *in vitro* in the presence of 500 mM NaCl at room temperature. **c**, Ectopically expressed GFP-TAZ was expressed at a lower level than endogenous TAZ in MCF-10A cells as shown by western blotting. GAPDH was used as a loading control. **d**, Flag-TAZ formed nuclear puncta when transfected into the MCF-10A cells, as detected by immunofluorescence staining with anti-Flag. Scale bar, 10 μm. Experiments in **a**–**d** were repeated independently three times with similar results. Unprocessed blots are provided in Unprocessed Blots Extended Data Fig. 1.

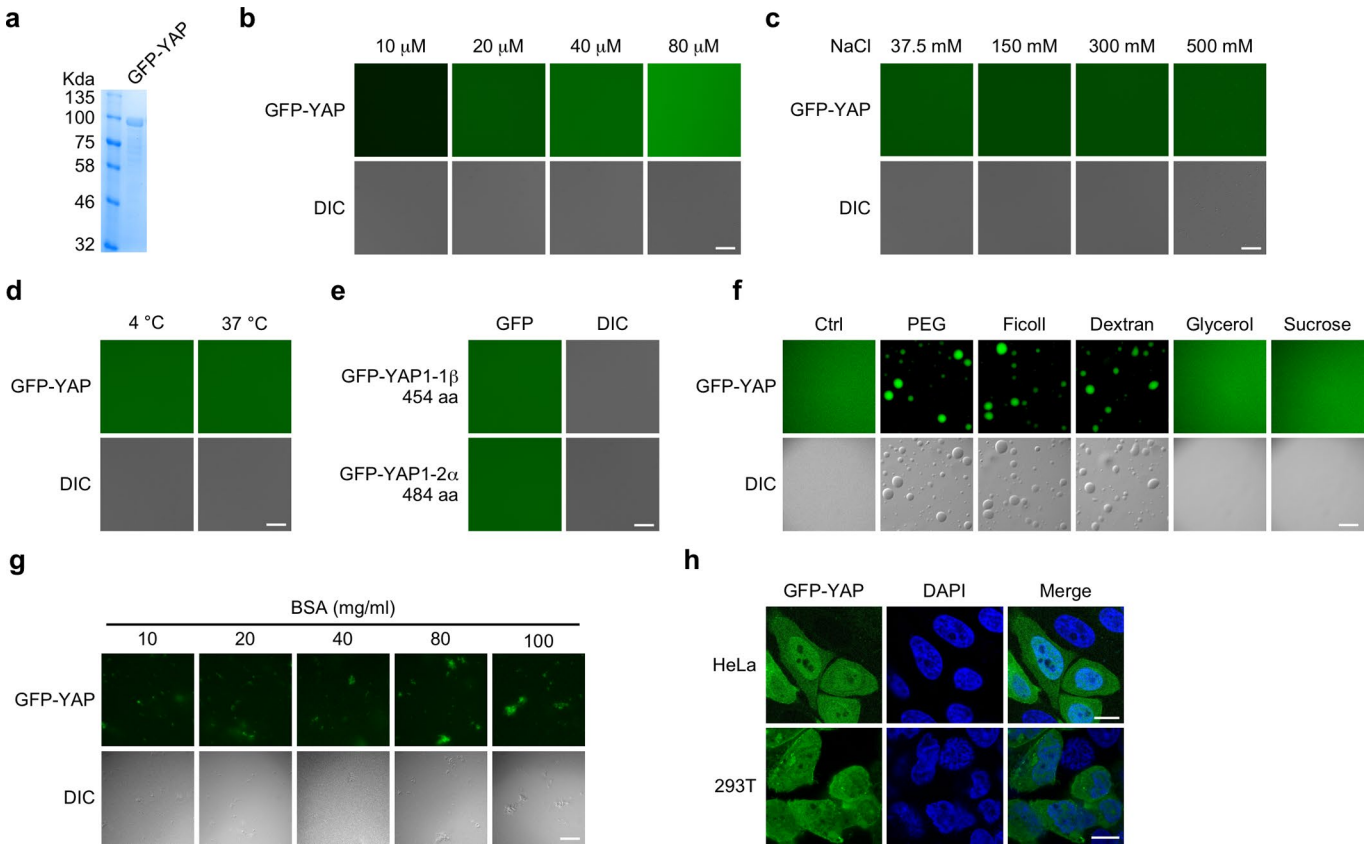

Extended Data Fig. 2 | YAP does not form droplets *in vitro* and *in vivo* in the absence of crowding agents. a, GFP-YAP purified from *E. coil* were analyzed by SDS-PAGE and visualized by Coomassie blue staining. **b**, GFP-YAP at varying concentrations was subjected to the droplet formation assay at room temperature and in the presence of 500 mM NaCl. **c**, 50 μM GFP-YAP was subjected to the droplet formation assay at room temperature in the presence of indicated salt concentrations. **d**, 50 μM GFP-YAP was subjected to droplet formation in the presence of 150 mM NaCl at 4 °C or 37 °C. **e**, Two YAP isoforms, GFP-YAP1–1β or GFP-YAP1–2α, did not form droplets (50 μM protein, 500 mM NaCl and room temperature). aa, amino acids. **f**, 50 μM GFP-YAP formed droplets in the presence of 10% PEG-8000, Ficoll or Dextran but not 10% glycerol or sucrose. Droplet formation assay was performed in the presence of 500 mM NaCl at room temperature. **g**, 50 μM GFP-YAP did not form droplets in the presence of BSA at varying concentrations. **h**, GFP-YAP did not form nuclear puncta in both HeLa cells and 293T cells. Scale bars, 10 μm. Experiments in **a**–**h** were repeated independently three times with similar results.

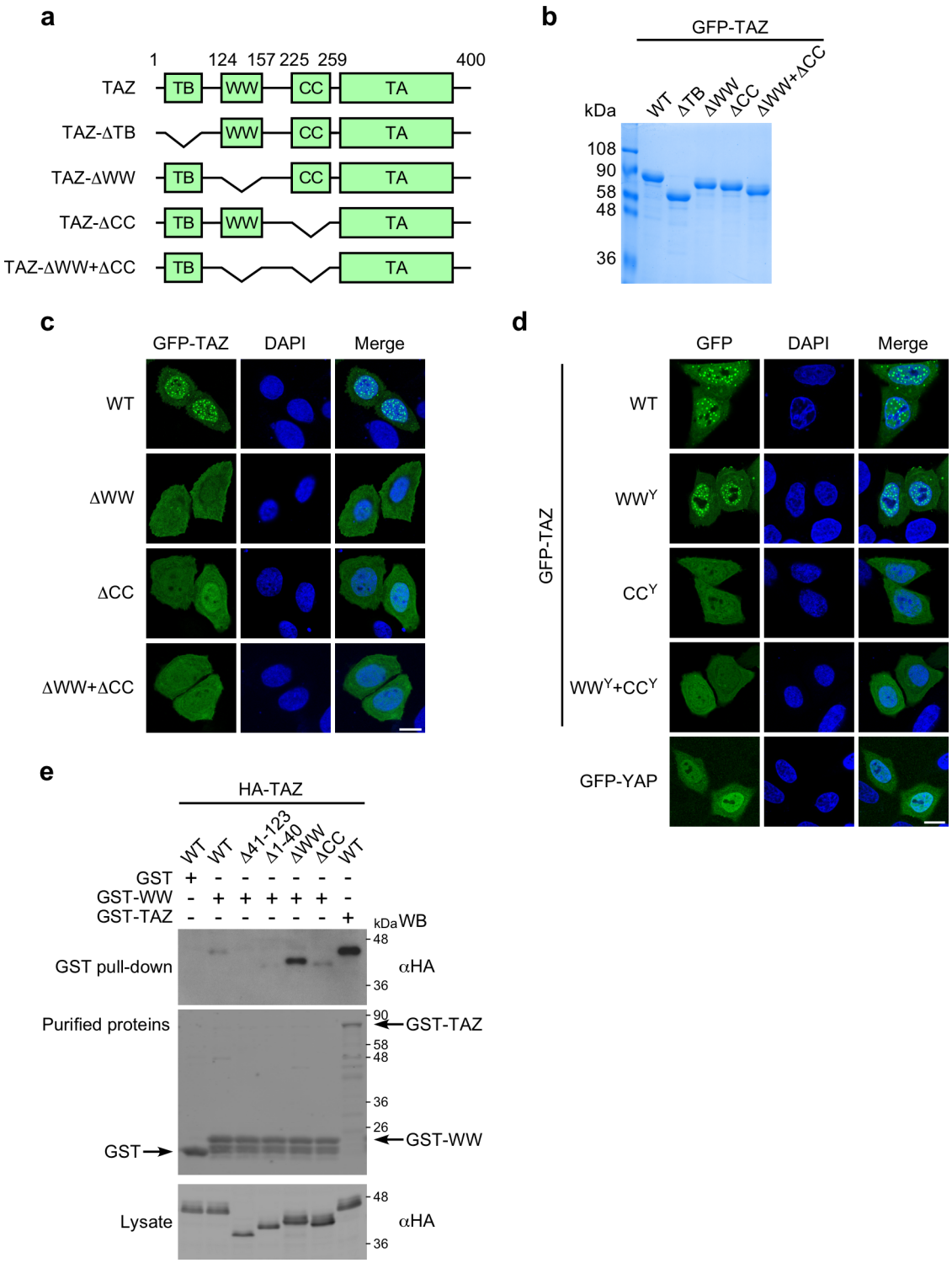

Extended Data Fig. 3 | The CC and WW domains are required for TAZ to form nuclear puncta. a, Domain structure of TAZ and TAZ truncations. The numbers above indicate the position of amino acid residues. **b**, Bacterially purified GFP-TAZ, ΔTB, ΔWW, ΔCC, and ΔWW+ΔCC proteins were analyzed by SDS-PAGE and detected by Coomasssie blue staining. **c**, Localization of GFP-TAZ and various mutants in HeLa cells. **d**, Localization of GFP-TAZ and various TAZ/YAP chimera in HeLa cells. Scale bars, 10 μm. **e**, A GST pull-down assay was performed by incubating immobilized GST fusion proteins with lysates of cells expressing HA-tagged WT or mutant TAZ, and the associated TAZ proteins were detected by western blotting with anti-HA (upper). GST fusion proteins were assessed by western blotting with anti-GST, and HA-TAZ proteins in the cell lysates were measured by western blotting (lower). Experiments in **b**–**e** were repeated independently three times with similar results. Unprocessed blots are provided in Unprocessed Blots Extended Data Fig. 3.

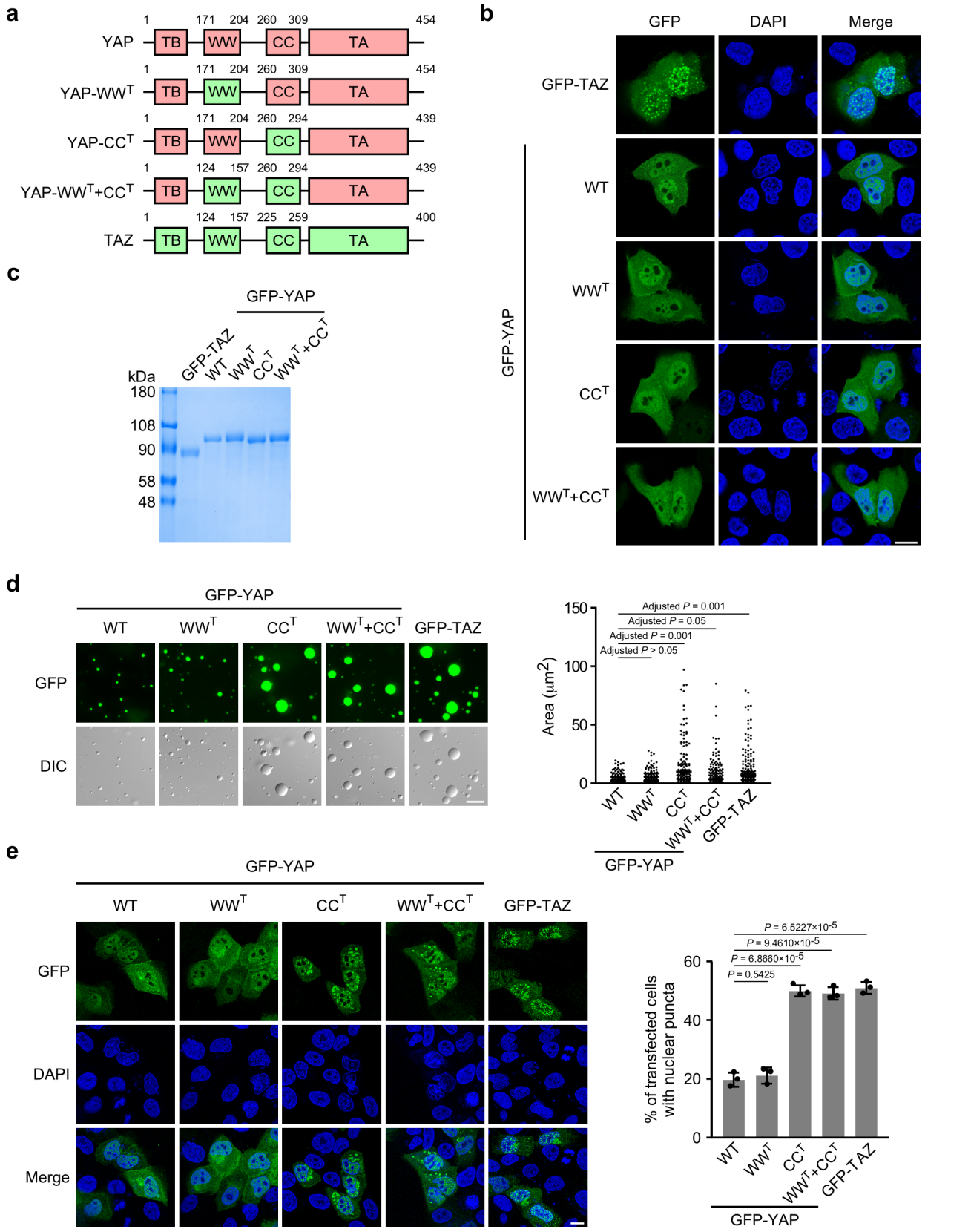

Extended Data Fig. 4 | See next page for caption.

Extended Data Fig. 4 | TAZ CC domain enhances YAP phase separation in the presence of PEG. a, Domain structure of YAP chimera. **b**, Substitution of the YAP CC and WW domains with that of TAZ is not sufficient to enable YAP to undergo LLPS in MCF10A cells in the absence of PEG. **c**, Coomasssie blue staining of various recombinant proteins purified from *E. coil*. **d**, 25 μM bacterially purified GFP-YAP chimera proteins were subjected to droplet formation assay in the presence of 10% PEG-8000. Quantification of the droplets is on the right. Scale bar, 10 μm. Data shown as the mean ± s.e.m. Statistical significance was evaluated using One-way ANOVA with Krusk-Wallis test. Droplets in n = 3 fields in each group were quantified. **e**, The TAZ CC and WW domains enhanced LLPS by GFP-YAP in transfected MCF10A cells in the presence of PEG as shown by confocal microscopy. Scale bar, 10 μm. Quantification of the percentage of cells that displayed nuclear puncta is shown on the right. Data shown as the mean ± s.e.m.. *P* value was determined by unpaired two-tailed Student's *t*-test. 80 transfected cells in each group were quantified. n = 3 biologically independent samples. Experiments in **b**, **c**, **e** were repeated independently three times with similar results. Experiments in **d** were repeated twice with similar results. Statistical source data for **d**, **e**, are provided in Statistical Source Date Extended Data Fig. 4.

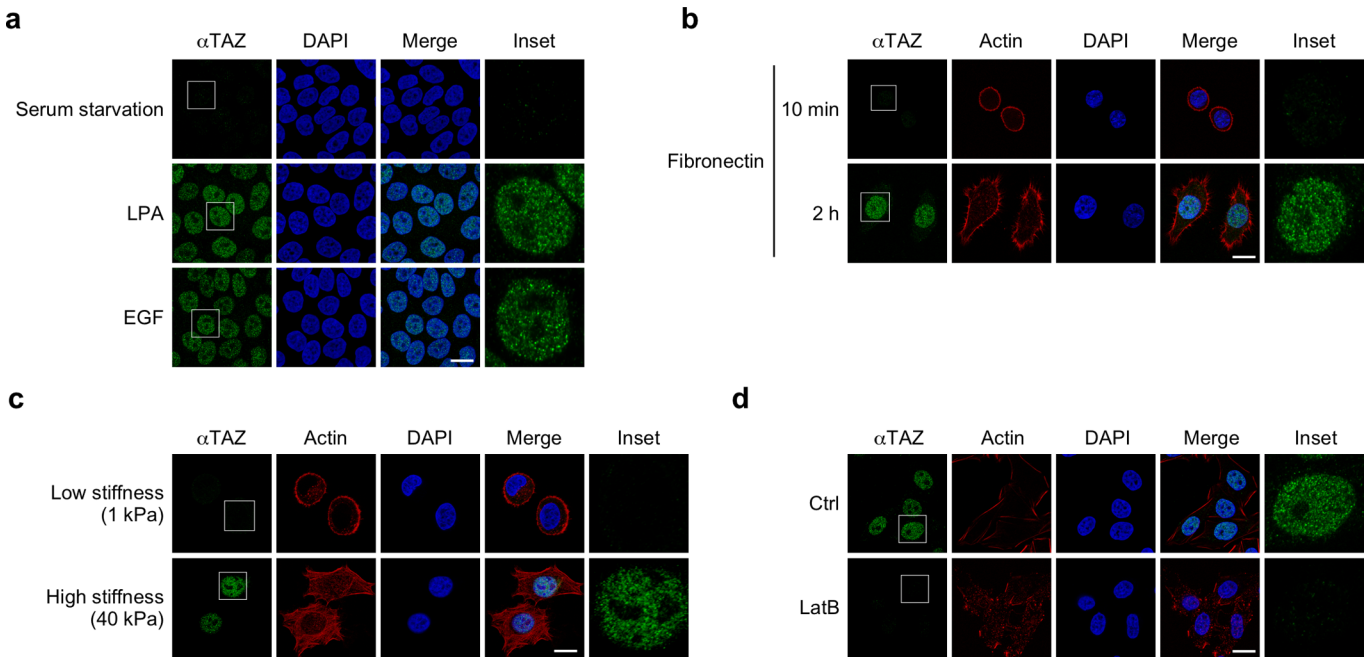

Extended Data Fig. 5 | Hippo signaling negatively regulates TAZ phase separation in HeLa cells. TAZ localization was examined by immunofluorescence staining with anti-TAZ (green) in HeLa cells that have been subjected to the following treatments: **a**, Serum-starved HeLa cells were treated with 1 μM LPA or 50 ng/ml EGF for 1 h. **b**, Serum-starved HeLa cells were seeded on fibronectin-coated coverslips for 10 min or 2 h in serum-free medium. **c**, HeLa cells were grown on fibronectin-coated polyacrylamide hydrogels of 1 kPa and 40 kPa stiffness. **d**, HeLa cells were treated with 1 μg/ml Latrunculin B for 1 h. Alexa Fluor 555-conjugated phalloidin (Red) staining was performed to detect F-actin in b-d. Scale bar, 10 μm. Experiments in **a**–**d** were repeated independently three times with similar results.

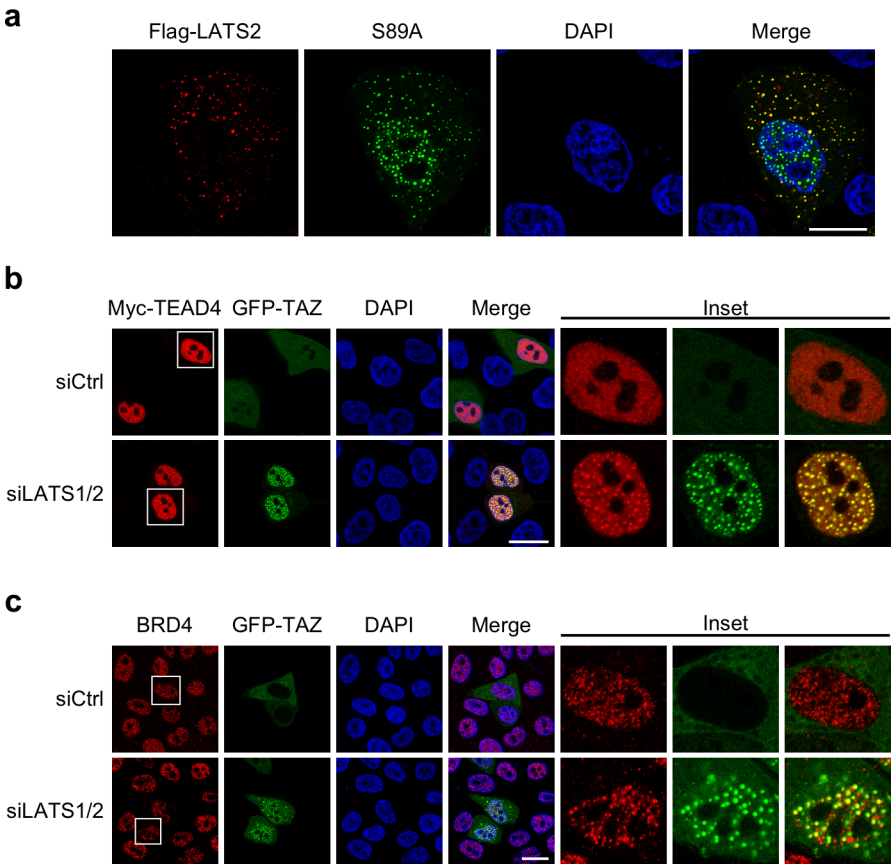

Extended Data Fig. 6 | LATS2 regulates TAZ LLPS and recruitment of TEAD4 and BRD4. a, MCF-10A cells transfected with GFP-TAZ-S89A and Flag-LATS2 were subjected to immunofluorescence staining with anti-Flag (Red). Scale bar, 10 μm. **b**, MCF-10A cells stably expressing siLATS1/2 were transfected with GFP-TAZ and Flag-TEAD4. TEAD localization at high cell density was detected by immunofluorescence staining with anti-Flag (Red). Scale bar, 10 μm. **c**, MCF-10A cells stably expressing siLATS1/2 were transfected with GFP-TAZ. Endogenous BRD4 localization was examined by immunofluorescence staining with anti-BRD4 (Red). Scale bar, 10 μm. All experiments were repeated independently three times with similar results.

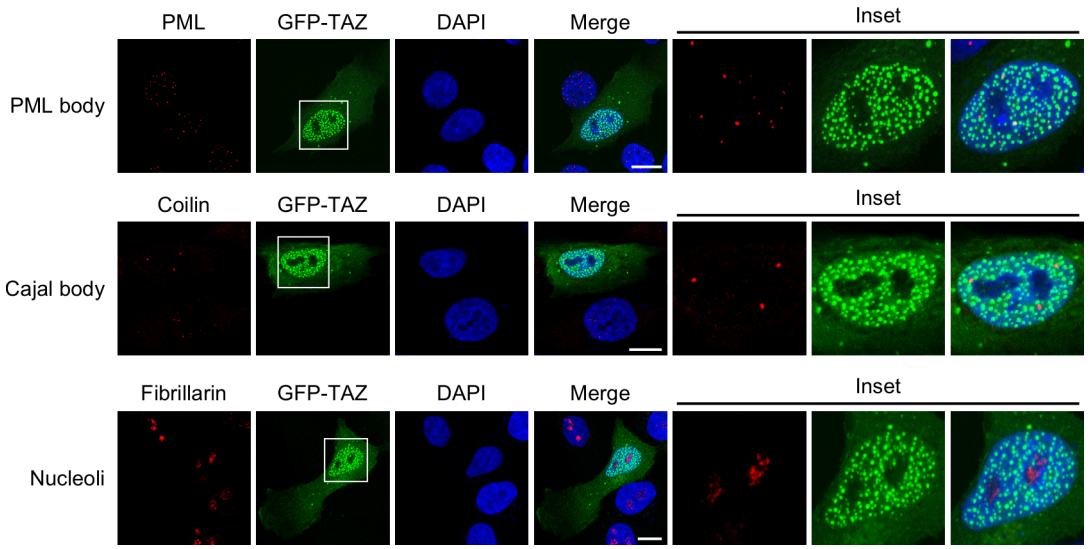

Extended Data Fig. 7 | TAZ nuclear condensates do not co-localize with the PML bodies, Cajal bodies or nucleoli. The PML nuclear bodies, Cajal Bodies and nucleoli in MCF-10A cells expressing GFP-TAZ (green) were detected by immunofluorescence staining with antibodies targeting PML, Coilin and Fibrillarin, respectively (red). Scale bar, 10 μm. Experiments were repeated independently three times with similar results.

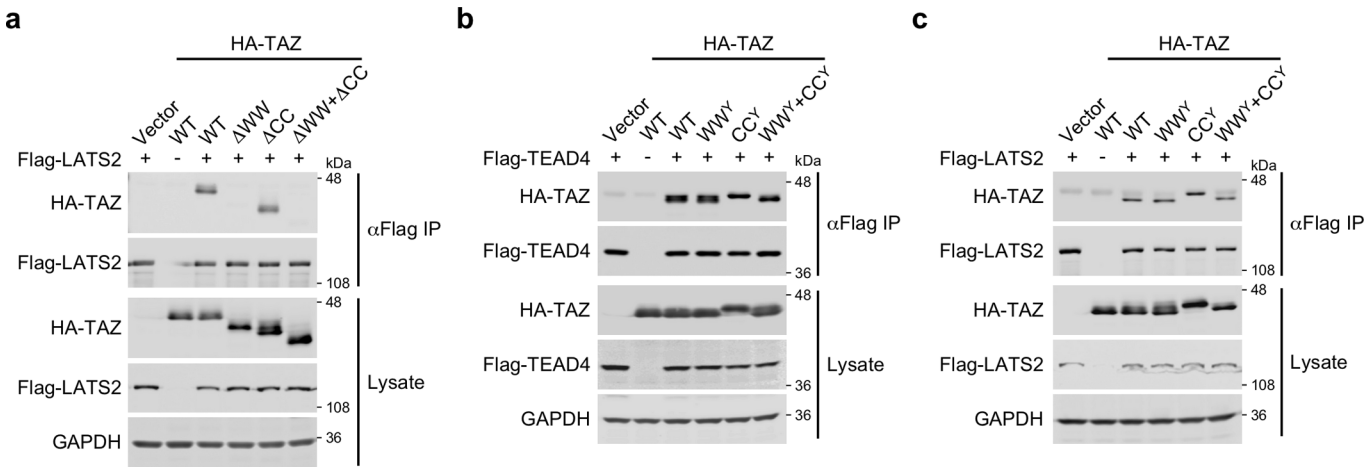

Extended Data Fig. 8 | TAZ mutants lacking the CC domain still bind to LAST2 and TEAD4. a, HA-tagged WT and mutant TAZ were co-transfected into 293T cells with Flag-LATS2. TAZ proteins associated with LATS2 were isolated by immunoprecipitation with anti-Flag and detected by western blotting with anti-HA antibodies (upper panels). The abundance of these proteins in the cell lysates was assessed by western blotting (lower panels). GAPDH was used as a loading control. **b**, Interaction of various TAZ mutants with Flag-TEAD4 was analyzed by co-IP assay as described in **a**. **c**, Interaction of various TAZ/YAP chimera with LATS2 was analyzed by co-IP as described in **a**. All experiments were repeated independently three times with similar results. Unprocessed blots are provided in Unprocessed Blots Extended Data Fig. 8.

HEXIM1 controls P-TEFb processing and regulates drug sensitivity in triple-negative breast cancer

Hengyi Shao[a,†], Qingwei Zhu[a,†], Huasong Lu[a], Amanda Chang[a], Carol Gao[a], Qiang Zhou[a,*], and Kunxin Luo[a,b,*]

[a]Department of Molecular and Cell Biology, University of California, Berkeley, CA 94720; [b]Life Sciences Division, Lawrence Berkeley National Laboratory, Berkeley, CA 94720

ABSTRACT **The positive transcription elongation factor b (P-TEFb), composed of CDK9 and cyclin T, stimulates transcriptional elongation by RNA polymerase (Pol) II and regulates cell growth and differentiation. Recently, we demonstrated that P-TEFb also controls the expression of EMT regulators to promote breast cancer progression. In the nucleus, more than half of P-TEFb are sequestered in the inactive-state 7SK snRNP complex. Here, we show that the assembly of the 7SK snRNP is preceded by an intermediate complex between HEXIM1 and P-TEFb that allows transfer of the kinase active P-TEFb from Hsp90 to 7SK snRNP for its suppression. Down-regulation of HEXIM1 locks P-TEFb in the Hsp90 complex, keeping it in the active state to enhance breast cancer progression, but also rendering the cells highly sensitive to Hsp90 inhibition. Because HEXIM1 is often down-regulated in human triple-negative breast cancer (TNBC), these cells are particularly sensitive to Hsp90 inhibition. Our study provides a mechanistic explanation for the increased sensitivity of TNBC to Hsp90 inhibition.**

Monitoring Editor
Carl-Henrik Heldin
Ludwig Institute for Cancer Research

Received: Dec 20, 2019
Revised: May 28, 2020
Accepted: Jun 2, 2020

INTRODUCTION

Altered gene expression is a hallmark of cancer and plays a key role in malignant progression. The transcription elongation machinery has been shown to control the expression of a large number of genes involved in cell growth, differentiation, and stem cell self-renewal (Zhou and Yik, 2006). For many such genes, RNA polymerase (Pol) II already exists in their promoter-proximal regions in a paused state bound by two negative factors, NELF and DSIF, before the full induction of expression; and the rate-limiting step for their activation is the release of Pol II from the pause. A central component of the transcription elongation machinery is the positive transcription elongation factor b (P-TEFb). Consisting of CDK9 and cyclin T (CycT), P-TEFb releases Pol II from promoter-proximal pausing by phosphorylating the C-terminal domain (CTD) of Pol II, as well as DSIF and NELF. This leads to the production of full-length mRNA transcripts (Zhou *et al.*, 2012).

P-TEFb can exist in at least three distinct major complexes that collectively constitute a functional network (Ott *et al.*, 2011; Zhou *et al.*, 2012). Most P-TEFb in cells are sequestered in an inactive form in the 7SK small nuclear ribonucleoprotein complex (7SK snRNP). Within this complex, 7SK small nuclear RNA (snRNA) serves as a central scaffold that is stabilized by LARP7 (La-related protein 7; He *et al.*, 2008; Krueger *et al.*, 2008) and MepCE (Methylphosphate capping enzyme) (Jeronimo *et al.*, 2007; Xue *et al.*, 2010). HEXIM1 (hexamethylene bisacetamide inducible protein 1) binds to the 7SK snRNA in the complex and inhibits the CDK9 kinase activity (Yik *et al.*, 2003). In response to a number of stress or growth-stimulating signals, P-TEFb is released from the 7SK snRNP and recruited to the chromatin templates by the bromodomain protein BRD4 to promote transcription of many cellular primary response genes such as *Myc, Fos*, and *JunB* (Jang *et al.*, 2005; Yang *et al.*, 2005). P-TEFb can also exist in a transcriptionally active form in the multisubunit super elongation complex (SEC), which contains mostly fusion partners (e.g., AFF1, AFF4, ELL1, ELL2, ENL, and AF9) of the mixed lineage leukemia (MLL) protein. The SEC is recruited by the HIV-1 Tat protein

This article was published online ahead of print in MBoC in Press (http://www.molbiolcell.org/cgi/doi/10.1091/mbc.E19-12-0704).

†These authors contributed equally to this work.

*Address correspondence to: Kunxin Luo (kluo@berkeley.edu); Qiang Zhou (qzhou@berkeley.edu).

[AQ 1] Abbreviations used:

or MLL-fusion proteins to greatly stimulate transcription of HIV and MLL-target genes, respectively (Mueller *et al.*, 2009; He *et al.*, 2010; Lin *et al.*, 2010; Sobhian *et al.*, 2010; Yokoyama *et al.*, 2010; Lu *et al.*, 2014). The latter leads to some of the most severe forms of childhood leukemia.

P-TEFb and its binding partners have been implicated in human cancer. In addition to the key role of the SEC in leukemogenesis (Mueller *et al.*, 2009; Lin *et al.*, 2010; Yokoyama *et al.*, 2010), BRD4, the chromatin adaptor for P-TEFb, has also been linked to many human cancers, including acute myeloid leukemia (AML), chronic myeloid leukemia (CML), and breast cancer (Blobel *et al.*, 2011; Dawson *et al.*, 2011; Zuber *et al.*, 2011; Winter *et al.*, 2012; Wedeh *et al.*, 2015; Ren *et al.*, 2018). BRD4 has been reported to regulate breast cancer progression by modulating Notch and Wnt5A signaling (Shi *et al.*, 2014; Andrieu *et al.*, 2016). The 7SK snRNP components have also been implicated in human breast cancer. For example, microsatellite instability (MSI)–induced LARP7 frame-shift mutations have been detected in ~35% of breast cancer samples characterized as MSI-high (Mori *et al.*, 2002). Further implying a key role of LARP7 in breast cancer progression, we reported that LARP7 is significantly down-regulated in aggressive human breast cancer tissues, and that this down-regulation resulted in increased breast cancer epithelial–mesenchymal transition (EMT) and metastasis (Ji *et al.*, 2014). Mechanistically, we showed that the decreased LARP7 expression reduced the 7SK snRNP level and redistributed P-TEFb to the SEC, leading to P-TEFb activation and increased transcription of EMT transcription factors to promote breast cancer EMT, invasion, and metastasis (Ji *et al.*, 2014).

Given the above results strongly suggesting that P-TEFb activation plays an important role in promoting breast cancer progression, we predict that other P-TEFb partners may also be implicated in breast cancer. Indeed, another 7SK snRNP subunit, HEXIM1, has also been reported to be down-regulated by estrogens and decreased in breast tumors (Wittmann *et al.*, 2003). HEXIM1 was originally identified as a protein that is induced in vascular smooth muscle cells by hexamethylene bisacetamide (HMBA; Ouchida *et al.*, 2003), an inducer of cell differentiation, and was later found to be a critical component of the 7SK snRNP (Yik *et al.*, 2003; Michels *et al.*, 2004). Overexpression of HEXIM1 in breast cancer cells was found to decrease cell proliferation and anchorage-independent growth (Wittmann *et al.*, 2003). Furthermore, in the murine Polyoma middle T (PyMT) transgenic model of breast cancer, HEXIM1 has been found to suppress metastasis (Ketchart *et al.*, 2013). Finally, HEXIM1 can be recruited to the estrogen receptor target gene promoters to cause repression of estrogen-induced gene expression by tamoxifen (Ketchart *et al.*, 2011). Thus, HEXIM1 is clearly implicated in breast cancer. However, its mechanism of action and in particular whether its effects in breast cancer are dependent on its inhibition of P-TEFb have not been determined.

In this study, we examined the role of HEXIM1 in breast cancer and found that HEXIM1 expression is down-regulated in human triple-negative breast cancer (TNBC). This down-regulation renders TNBC cells particularly sensitive to the inhibition of Hsp90. Hsp90, as a molecular chaperone, is essential for the folding, activation, and turnover of many key regulators of cell growth and survival, including protein kinases and steroid hormone receptors, and also plays an important role in oncogenesis (Whitesell and Lindquist, 2005). Advanced cancer cells often exhibit elevated requirement for Hsp90 function to facilitate tolerance of oncogenic mutations and survival of cancer cells under heightened stress conditions from the microenvironment. Tumor cells often display increased abundance of Hsp90, which subsequently promotes tumor cell survival and transformation through effects on Akt, TNFα, NF-κB, and other oncogene or tumor suppressors, and overexpression of Hsp90 in breast cancer correlates with poor prognosis (Sidera and Patsavoudi, 2014). Interestingly, cancer cells appear to be particularly sensitive to inhibitors of Hsp90. For example, Caldas-Lopes *et al.* have shown that TNBC cells are highly sensitive to Hsp90 inhibition (Caldas-Lopes *et al.*, 2009). Moreover, inhibitors of Hsp90 are in Phase II clinical trials for treatment of several solid tumors including breast cancer, melanoma, prostate cancer, and myeloma (Beliakoff *et al.*, 2003; Solit *et al.*, 2008; Suzuki *et al.*, 2010). However, the molecular mechanism underlying this heightened sensitivity to Hsp90 inhibition has not been defined. Our study showed that the sensitivity of breast cancer cells to Hsp90 inhibition correlates with the levels of HEXIM1 and its ability to regulate CDK9 processing. HEXIM1 forms a complex with P-TEFb that serves as an intermediate to transfer the active P-TEFb from Hsp90 to the 7SK snRNP for its suppression. Down-regulation of HEXIM1 locks CDK9 in the immature state in the Hsp90 complex, rendering cells highly sensitive to Hsp90 inhibitors. Our study has provided a molecular basis for the sensitivity of TNBC to Hsp90 inhibition.

RESULTS

HEXIM1 expression level is reduced in TNBC

To investigate the role of HEXIM1 in breast cancer, we first performed data-mining of two publicly accessible datasets, from which HEXIM1 mRNA levels in different cancer types were derived and analyzed. Analysis of the Cancer Genome Atlas (TCGA) dataset demonstrated that the HEXIM1 level is lower in estrogen receptor (ER)– or progesterone receptor (PR)–negative breast cancers, but is not affected by the HER2 status (Figure 1A). Consistently, HEXIM1 expression was down-regulated in TNBC samples (Figure 1B). Analysis of the Oncomine dataset also indicated that HEXIM1 expression was reduced in TNBC (Figure 1C). Similarly, in a variety of human breast cancer cell lines, when they were normalized to the nontransformed mammary epithelial MCF10A cell line, the HEXIM1 mRNA levels were mostly lower in the TNBC cell lines (e.g., MDA-MB-468, MDA-MB-231, and BT549) than in the non-TNBC cells (Figure 1D). Finally, immunohistochemistry staining of a tissue array containing 71 non-TNBC and 66 TNBC samples of human malignant breast cancer showed that HEXIM1 protein level was also markedly reduced in human TNBC tissues (Figure 1E). These analyses suggest that HEXIM1 is down-regulated in human TNBC.

HEXIM1 KD moderately promotes proliferation and migration of breast cancer cells

We next asked whether reducing the HEXIM1 levels in untransformed mammary epithelial cells would promote transformation and malignant progression. To this end, we knocked down HEXIM1 in MCF10A cells by stably expressing a HEXIM1-specific shRNA (Figure 2A) and examined its effect on cell proliferation, morphological differentiation, and cell migration. HEXIM1 knockdown (KD) had little effect on the proliferation or apoptosis of MCF10A cells (Supplemental Figure S1). When cultured in the three-dimensional (3D) laminin-rich extracellular matrix (lrECM), the control MCF10A cells proliferated and underwent morphological differentiation to form multicellular acinar-like structures with well-defined borders and polarity. The HEXIM1 KD cells also formed acinar structures with proper apical and basolateral polarity, but these acini were much larger and contained a larger number of cells on the average (Figure 2B). This increase in the size of HEXIM1 KD acini was readily reversed by the reintroduction of HEXIM1-HA (Supplemental Figure S2, A and B). These data suggest that depletion of HEXIM1 leads to

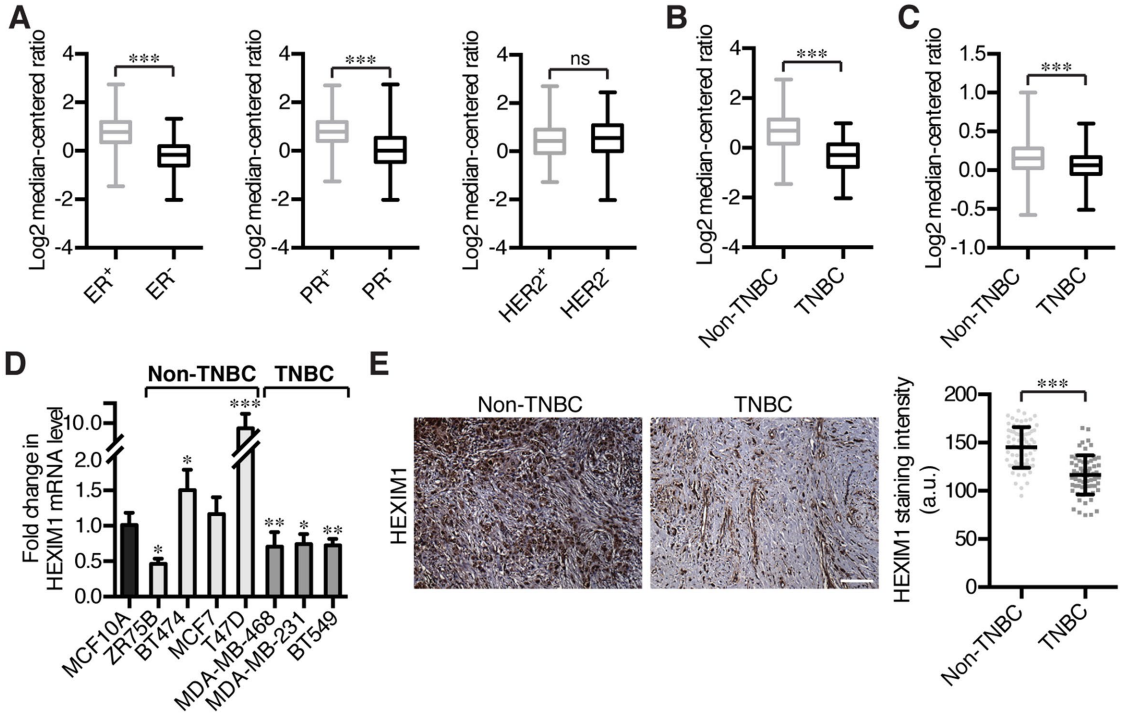

FIGURE 1: HEXIM1 is down-regulated in TNBC. (A) HEXIM1 expression levels in breast cancer of different ER (left), PR (middle), and HER2 (right) status in the TCGA database. ns: not significant, ***$p < 0.001$, Mann–Whitney test. (B, C) Box plots showed the decreased levels of HEXIM1 in TNBC from TCGA, B, and Oncomine, C, databases. ***$p < 0.001$, Mann–Whitney test. (D) HEXIM1 mRNA levels in human breast cancer cell lines as measured by qRT-PCR. PCR values were normalized to that of GAPDH. The HEXIM1 level in the nontransformed MCF10A cells was set as 1. **$p < 0.01$, ***$p < 0.001$, Student's *t* test. (E) Human breast cancer tissue arrays consisting of malignant non-TNBC samples ($n = 71$) and TNBC samples ($n = 66$) were subjected to IHC staining using anti-HEXIM1. Quantitation of the HEXIM1 level was shown in the graph to the right. Data are shown as means ± SD. ***$p < 0.001$, Student's *t* test. Scale bar: 100 μm.

an increase in the proliferative potential of cells. This increased proliferation in the 3D culture was not sufficient for oncogenic transformation, as the HEXIM1 KD cells failed to form soft-agar colonies (He *et al.*, 2008).

In both noninvasive T47D and invasive MDA-MB-231 breast cancer cells, HEXIM1 KD moderately enhanced cell motility and migration (Figure 2, C–E), but had little effect on the transforming activity of these cells in vitro as measured by the soft-agar assay for anchorage-independent growth (Figure 2F). Thus, HEXIM1 KD promoted breast cancer cell proliferation and migration, but did not significantly affect the transforming activity of these cells in vitro.

Down-regulation of HEXIM1 sensitizes malignant breast cancer cells to Hsp90 inhibitors

We next examined whether HEXIM1 affected the response of malignant MDA-MB-231 breast cancer cells to chemotherapeutic or other anti-cancer drugs using a colony formation assay to measure cell proliferation and survival in vitro. As shown in Figure 3A, HEXIM1 KD did not change the sensitivity to three chemotherapy drugs, [AQ 3] doxorubicin, 5-fluorouracil, and ~~Taxol~~, which are frequently used in breast cancer treatment. However, the sensitivity to geldanamycin (GA), an Hsp90 inhibitor, was significantly increased. While 4 nM GA only mildly inhibited the colony-forming ability of control MDA-MB-231 cells, it completely suppressed this ability of the two HEXIM1 KD clones (Figure 3B) and caused apoptosis of the treated cells (Figure 3C). Importantly, this enhanced sensitivity to GA in HEXIM1 KD cells could be efficiently reversed by overexpression of an shRNA-resistant HEXIM1-HA cDNA (Supplemental Figure S3, A and B). In addition, the HEXIM1 KD cells showed similarly increased sensitivity to another Hsp90 inhibitor, Radicicol (RD) (Figure 3D). These results suggest that down-regulation of HEXIM1 enhanced the sensitivity of MDA-MB-231 breast cancer cells to Hsp90 inhibition.

A potential correlation between the HEXIM1 levels and the sensitivity to Hsp90 inhibitors seen in MDA-MB-231 cells prompted us to test this correlation further in other breast cancer cell lines. To this end, a panel of breast cancer cell lines expressing varying levels of HEXIM1 was treated with GA and their viability was then assessed. Interestingly, several ER-positive luminal breast cancer cell lines with relatively high expression of HEXIM1, including BT474, MCF7, and T47D, were more resistant to GA than the TNBC cell lines MDA-MB-468 and BT549, which have lower levels of HEXIM1 expression (Figure 3E). One exception is MDA-MB-231, which was more resistant to GA than other TNBC cell lines. We found that although the HEXIM1 mRNA level was low in MDA-MD-231 cells (Figure 1D), the HEXIM1 protein level was relatively high and at a level comparable to those in the ER-positive cell lines (Supplemental Figure S3C). Yet reducing HEXIM1 expression rendered MDA-MD-231 more sensitive to GA (Figure 3, B and C). Consistently, increasing HEXIM1 expression in the HEXIM1-low BT549 cell line rendered the cells less sensitive to GA (Supplemental Figure S3, D and E). Thus, the HEXIM1 level appears to correlate negatively with the sensitivity of metastatic breast cancer cells to Hsp90 inhibitors. This result is in agreement with a previous report suggesting that TNBCs are particularly sensitive to inhibition of Hsp90 due to an unknown reason (Caldas-Lopes *et al.*, 2009).

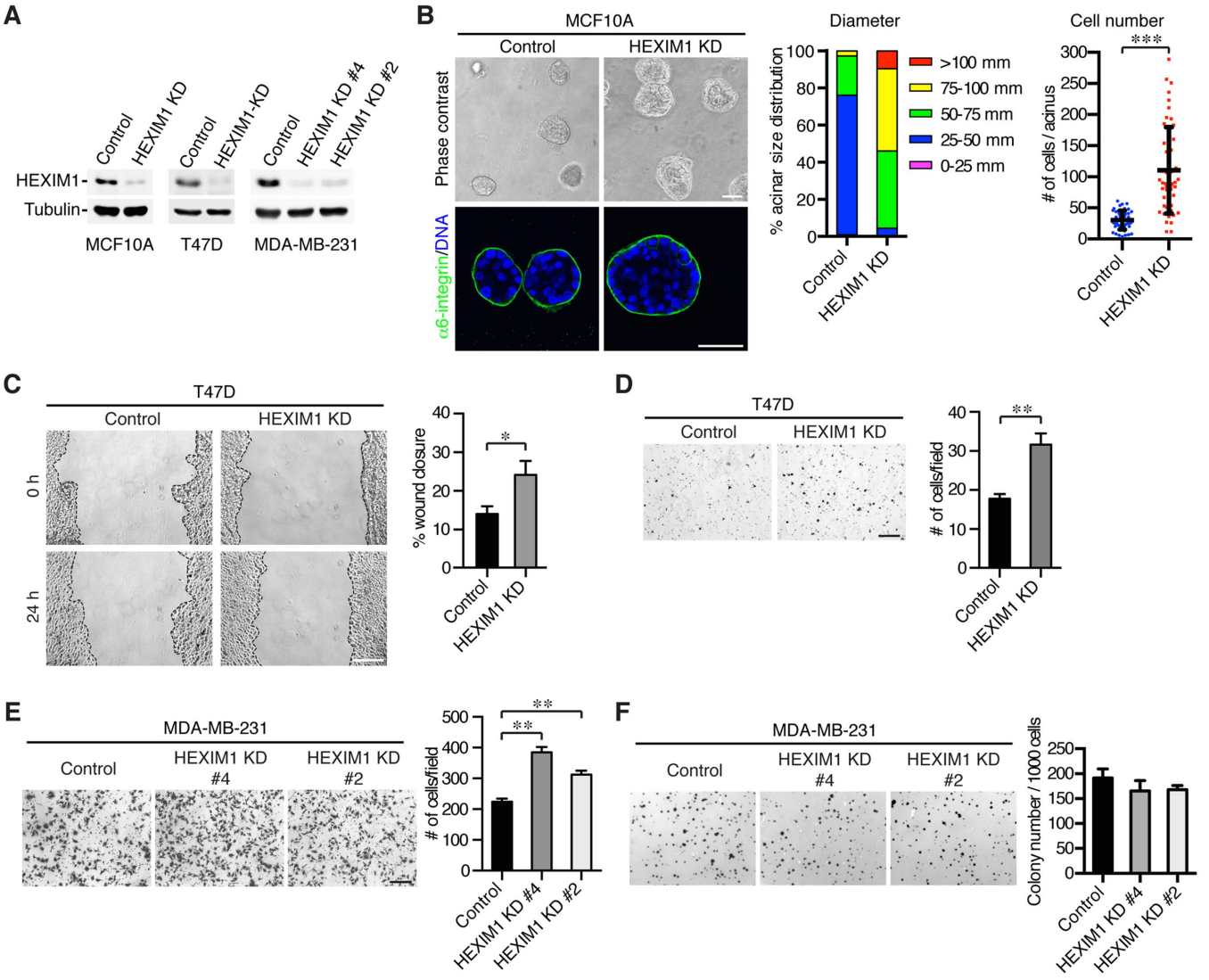

FIGURE 2: HEXIM1 KD moderately promotes breast cancer cell proliferation and migration. (A) Western blotting showing the efficiency of stable HEXIM1 knockdown by shHEXIM1 in MCF10A, T47D, and MDA-MB-231 cells. Tubulin was used as a loading control. (B) Representative phase contrast (top panel) and confocal (bottom panel) images of MCF10A control and HEXIM1 KD cells cultured on lrECM for 7 d. Blue, DAPI; green, α6-integrin. Scale bars: 50 μm. Quantitative analyses of acinar size distribution (middle graph; $n = 110$) and the average cell number per acinus (right graph; $n = 50$) are shown in the graphs. ***$p < 0.001$, Student's t test. (C) Wound healing assay. Wound closure was monitored by phase contrast microscopy and quantified. Data are presented as means ± SEM from four independent assays. *$p < 0.05$, Student's t test. Scale bar: 20 μm. (D, E) Cell migration assay. Transwell assays were performed for 24 h (T47D) or 4 h (MDA-MB-231), and migrated cells were stained and counted. Data are shown as means ± SEM derived from four independent experiments. **$p < 0.01$, Student's t test. Scale bar: 20 μm. (F) Anchorage-independent growth of MDA-MB-231 control or HEXIM1 KD cells was measured by a soft agar assay. The number of colonies was quantified and is shown in the graph to the right.

HEXIM1 KD sensitizes xenografted MDA-MB-231 tumors to GA in vivo

Because HEXIM1 KD rendered MDA-MB-231 cells more sensitive to killing by GA, we predicted that GA might also inhibit the oncogenic potential of these cells. Indeed, treatment of MDA-MB-231 HEXIM1 KD cells with GA led to a significant inhibition of the anchorage-independent growth, whereas the same treatment only had a very minor effect on the parental MDA-MB-231 cells (Figure 4A). To examine the effect of GA on tumor growth in a xenograft mouse model in vivo, we injected control MDA-MB-231 cells and their HEXIM1 KD derivative subcutaneously into the nude mice. The HEXIM1 KD was found to promote tumor development markedly, resulting in bigger tumors and an elevated tumor burden (Figure 4, B and C). This is consistent with the model that HEXIM1 has tumor suppressor activities (Wittmann *et al.*, 2003; Ogba *et al.*, 2010; Ketchart *et al.*, 2013; Tan *et al.*, 2016). After the tumors reached a measurable size, the mice were administered GA or vehicle (PBS) for three additional weeks. While GA had little effect on the control tumors, it inhibited growth of the HEXIM1 KD tumors (Figure 4, B and C). Consistently, HEXIM1 KD tumors exhibited a significantly higher level of apoptosis upon GA treatment than control tumors (Figure 4D). Thus, similarly to the observations in vitro, down-regulation of HEXIM1

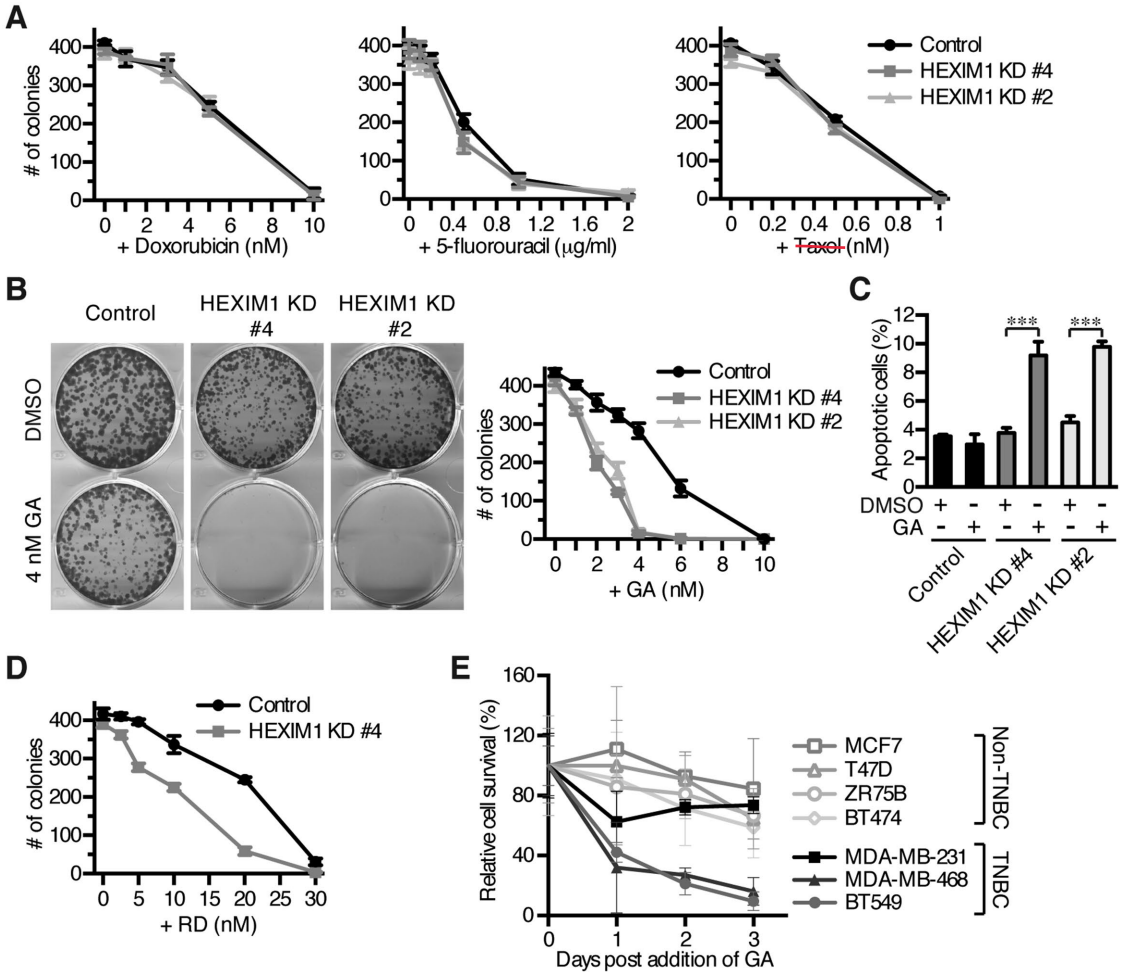

FIGURE 3: HEXIM1 KD increases the sensitivity of metastatic breast cancer cells to Hsp90 inhibitors. (A, B, D) Clonogenic growth assays. MDA-MB-231 control or HEXIM1 KD cells were treated with various concentration of doxorubicin, 5-fluorouracil, or ~~Taxol~~, as indicated in A, GA in B, and RD in D. Representative images of the colony-forming assay are shown in B, and quantitations of the colonies formed are shown in the graphs in A, B, D. (C) Flow cytometric analysis of the apoptotic cells. Cells were treated with GA or DMSO for 48 h, followed by propidium iodide staining and flow cytometric analysis. Data are presented as means ± SD in triplicates. ***$p < 0.001$, Student's t test. (E) Viability of various breast cancer cell lines upon treatment with 40 nM GA. The relative cell survival was calculated by comparing the number of cells in GA-treated group to that of DMSO controls. Data represent the average values from three independent assays.

increased the sensitivity of malignant MDA-MB-231 tumors to Hsp90 inhibition in vivo.

HEXIM1 KD increases binding of CDK9 to Hsp90

We next investigated the mechanism underlying the altered sensitivity of HEXIM1 KD breast cancer cells to Hsp90 inhibitors. Because HEXIM1 is a critical member of the 7SK snRNP that maintains P-TEFb in the inactive state (Yik *et al.*, 2003; Michels *et al.*, 2004), we examined whether the depletion of HEXIM1 redistributed P-TEFb from 7SK snRNP to the active BRD4 or SEC complexes. CDK9 and its associated proteins were isolated by immunoprecipitation with anti-CDK9 antibodies from nuclear extracts of control MDA-MB-231 or HEXIM1 KD cells and analyzed by Western blotting with antibodies targeting different P-TEFb partners. As expected, HEXIM1 KD significantly impaired the assembly of the 7SK snRNP and reduced association of P-TEFb to a key 7SK snRNP component LARP7 (Figure 5A). Surprisingly, HEXIM1 KD also decreased the binding of P-TEFb to the SEC components, including AFF4, ELL2, and to a certain extent ENL, while had little effect on the BRD4-P-TEFb interaction (Figure 5A).

Because there is no free P-TEFb in the cells, and P-TEFb is thought to be maintained in a functional equilibrium among the 7SK snRNP, BRD4-P-TEFb, and SEC complexes, destruction of one such complex is expected to result in P-TEFb's redistribution into the remaining complexes. However, the HEXIM1 KD reduced the bindings of P-TEFb to both 7SK snRNP and the SEC, but did not change the BRD4-P-TEFb interaction. This suggests the possible existence of other protein(s) that may bind to the released P-TEFb.

To determine whether the released CDK9 in HEXIM1 KD cells associated with another cellular protein, we performed affinity purification to identify the CDK9-associated proteins in the HeLa-based F1C2 cell line that stably expresses shHEXIM1 and the FLAG-tagged CDK9 (Yang *et al.*, 2001). Similar to the observation in MDA-MB-231 cells, HEXIM1 KD in F1C2 cells also decreased the presence of CDK9 in both the 7SK snRNP and SEC but not in the BRD4 complex (Figure 5B). CDK9-FLAG and its associated factors immunoprecipitated from

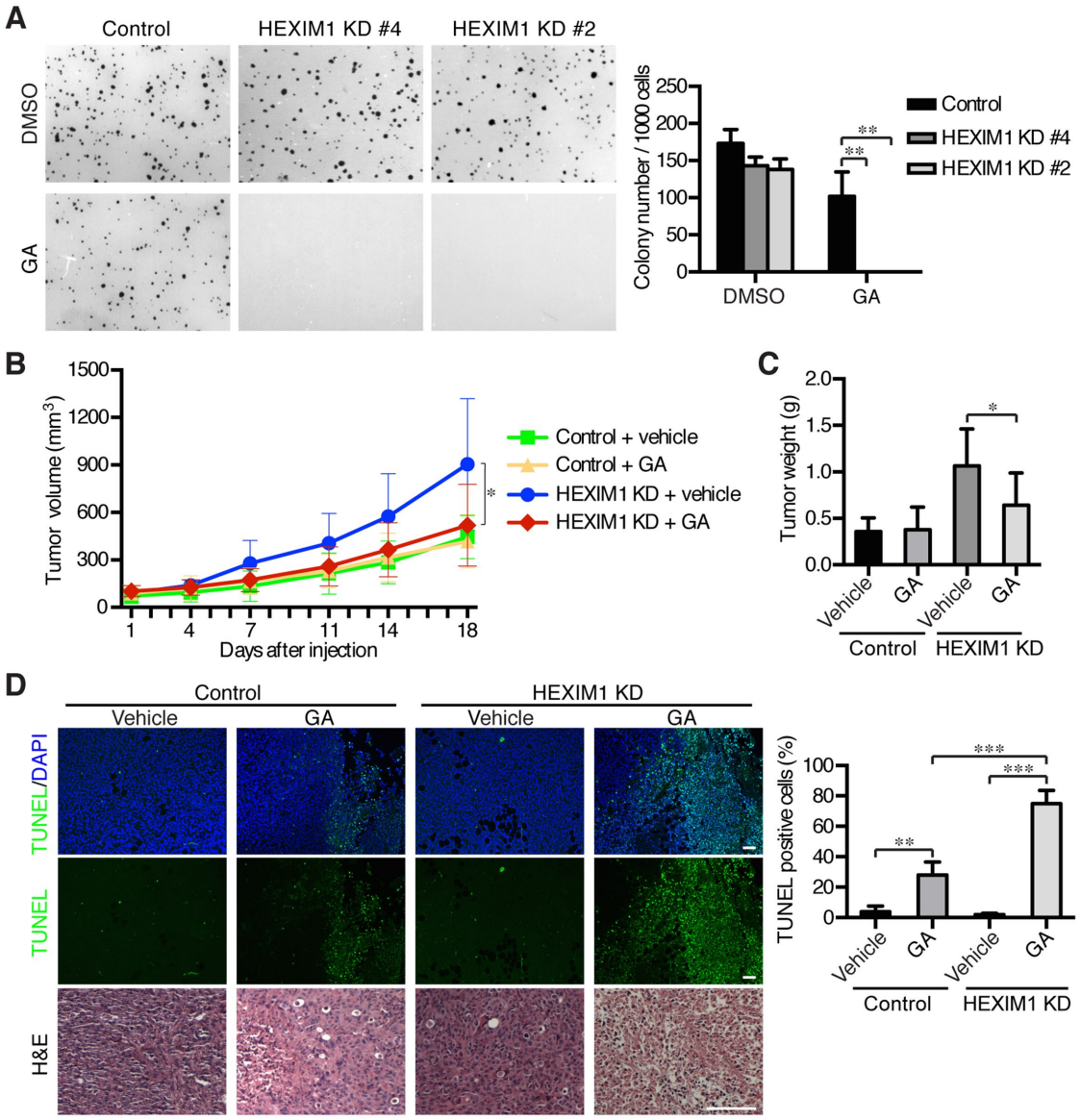

FIGURE 4: HEXIM1 KD sensitizes TNBC tumors to GA in vivo. (A) Soft agar assay. MDA-MB-231 control or HEXIM1 KD cells were grown on soft agar in the presence of 30 nM GA or DMSO. The soft-agar colonies were stained with MTT and quantified and are shown in the right graph. Data are presented as means ± SD in triplicates. $^{**}p < 0.01$, Student's *t* test. (B, C) Effects of GA on breast cancer growth in vivo using the xenograft mouse model. Control or HEXIM1 KD tumors were injected into the nude mice and allowed to grow to approximately 100 mm^3. GA was then injected intraperitoneally twice per week, and tumor volume was measured continuously, B. Tumors were harvested 3 wk later, and tumor weight was measured at the endpoint, C. $^{*}p < 0.05$, Student's *t* test. (D) Tumor sections were subjected to the TUNEL assay and H&E staining. The apoptotic index was calculated as a ratio of the number of apoptotic cells to that of the total cells (right graph). Data are presented as the mean ± SD by Student's *t* test. $^{**}p < 0.01$, $^{***}p < 0.001$. Scale bars: 50 μm.

control and the HEXIM1 KD cells were resolved by electrophoresis and visualized by silver staining (Figure 5C). Interestingly, a protein of approximately 90 kDa was found to interact significantly more with CDK9-FLAG in the KD cells. Mass spectrometry analysis identified this protein as Hsp90. We further confirmed the increased binding of CDK9 to Hsp90 upon HEXIM1 KD using coimmunoprecipitation followed by anti-Hsp90 Western blotting in both MDA-MB-231 and F1C2 background (Figure 5D and Supplemental Figure S4A). Consistent with this, in TNBC cells with a lower HEXIM1 level (MDA-MB-468 and BT549), a notable increase in the CDK9-Hsp90 interaction was detected (Supplemental Figure S4B).

HEXIM1 plays a key role in P-TEFb assembly into the 7SK snRNP

We have previously reported that the newly synthesized CDK9 interacts sequentially with two chaperone proteins in the cytoplasm, Hsp70 and Hsp90, which allows proper folding and assembly of CDK9 into the active CDK9-CycT1 heterodimer of P-TEFb (O'Keeffe *et al.*, 2000). We showed that inactivation of Hsp90 by GA prevented the generation of active P-TEFb, leading to rapid degradation of the free and unprotected CDK9 (O'Keeffe *et al.*, 2000). To examine whether the increased interaction of CDK9 with Hsp90 upon HEXIM1 KD could be disrupted by GA, the interaction in cells

treated with GA or DMSO was assessed by the coimmunoprecipitation assay. As shown in Supplemental Figure S4C, GA abolished the CDK9–Hsp90 interaction in both the HEXIM1 KD and control F1C2 cells, suggesting that the interaction depended on the activity of Hsp90. Consistently, HEXIM1 KD in MDA-MB-231 cells also led to an increase in the CDK9–Hsp90 interaction, which was abolished by GA (Figure 5D). Importantly, this nuclear CDK9-Hsp90 complex is free of Cdc37, which is only detected in the cytoplasmic complex with Hsp90 and CDK9 in transfected 293T cells (O'Keeffe *et al.*, 2000), but not breast cancer cells or Hela cells (Supplemental Figure S4D).

One important question is whether CycT1 is part of the CDK9–Hsp90 complex and whether this Hsp90-bound CDK9 is active as a kinase. The sequential immunoprecipitation assay confirmed that the CDK9–CycT1–Hsp90 complex existed in the HEXIM1 KD cells (Figure 5E), suggesting that the P-TEFb complex is formed in the presence of Hsp90. Furthermore, in an in vitro kinase assay, the Hsp90-bound P-TEFb showed kinase activity comparable ~~TO~~ or even higher than that in the CDK9–CycT1 heterodimer, suggesting that the CDK9–CycT1–Hsp90 complex is an active form of P-TEFb (Figure 5F). This explains why in the HEXIM1 KD cells, although the levels of the known SEC-bound P-TEFb complex are decreased, the cells still exhibit active transcription and moderately enhanced oncogenic transformation and invasion. Because P-TEFb is locked into the Hsp90 complex in HEXIM1 KD cells, disruption of this complex by GA results in the accumulation of ~~immature and~~ unprotected CDK9 that is quickly degraded, leading to the depletion of essential P-TEFb from the cells. This could be the underlying mechanism of the observed increased sensitivity of breast cancer cells to the Hsp90 inhibitors. The observation that P-TEFb is stuck in the Hsp90 complex upon HEXIM1 KD also suggests that HEXIM1 is normally required at a step after Hsp90 but before P-TEFb is assembled into the 7SK snRNP for its suppression. Thus, HEXIM1 may form an intermediate complex with CDK9–CycT1 that is required to stabilize and transfer P-TEFb from Hsp90 to the 7SK snRNP. Our study has thus identified the precise step of HEXIM1 action in P-TEFb maturation and suppression.

HEXIM1 KD increases the sensitivity of breast cancer cells to inhibition of CDK9

The above model makes two predictions. First, if the CDK9–CycT1–Hsp90 and CDK9–CycT1–HEXIM1 complexes are necessary key intermediates for P-TEFb maturation before P-TEFb is assembled into the 7SK snRNP, a complete disruption of the Hsp90–P-TEFb complex by GA should result in a decrease in the binding of CDK9 with HEXIM1, as well as its assembly into the 7SK snRNP, even in cells without the HEXIM1 KD. Indeed, when treated with increasing concentrations of GA, a gradual decrease in the associations of CDK9 with HEXIM1 and another key 7SK snRNP component, LARP7, was detected (Figure 5G).

Second, because HEXIM1 KD resulted in an increase of the active Hsp90-P-TEFb complex, these cells should also become sensitive to the inhibition of CDK9. To test this, we treated control and HEXIM1 KD MDA-MB-231 cells with increasing concentrations of iCDK9, a highly selective CDK9 inhibitor (Lu *et al.*, 2015) and examined the inhibitory effects on cell proliferation and survival with the colony formation assay. As shown in Figure 5H, the KD cells exhibited an elevated sensitivity to iCDK9 compared with the control cells. Moreover, a low concentration of iCDK9 (0.02 μM), although by itself it had a very minor effect on the colony formation ability of the cells, caused a slight but consistent enhancement of the suppressive effect of GA on the KD cells (Figure 5I), confirming that the heightened sensitivity of the HEXIM1 KD cells to Hsp90 inhibition is dependent on CDK9 and that the KD sensitizes cells to drugs targeting the P-TEFb–Hsp90 complex.

DISCUSSION

HEXIM1 was previously known as a key component of the 7SK snRNP that functions to inhibit the kinase activity of P-TEFb (Yik *et al.*, 2003; Zhou and Yik, 2006). Here, we show that HEXIM1 is essential for the assembly of P-TEFb into the 7SK snRNP by forming an intermediate complex with P-TEFb that allows transfer of P-TEFb from Hsp90 to 7SK snRNP (Figure 5J). Our data indicate that P-TEFb kinase activation occurs in the Hsp90 complex, and HEXIM1 acts at a step after this activation to enable the assembly of P-TEF into the 7SK snRNP to suppress its kinase activity. Depletion of HEXIM1 not only disrupted the 7SK snRNP, but more importantly, prevented P-TEFb from assembling into the 7SK snRNP and caused accumulation of active P-TEFb in the Hsp90 complex. These active P-TEFb-Hsp90 complexes can activate transcription to promote malignant progression of HEXIM1 KD breast cancer cells and at the same time render these cells more sensitive to the inhibitors of both Hsp90 and CDK9. This model explains well the observed different effects of the KD of LARP7 versus that of HEXIM1 on P-TEFb's kinase activity. LARP7 KD does not affect the earlier steps of P-TEFb maturation and processing, but releases P-TEFb from the 7SK snRNP to form more active SEC and BRD4 complexes (Ji *et al.*, 2014). In contrast, HEXIM1 KD prevented P-TEFb from incorporating into the 7SK snRNP and all the subsequent complexes (SEC and BRD4), and thus locked P-TEFb into the Hsp90 complex. While LARP7-low malignant breast cancer cells are sensitive to CDK9 and BRD4 inhibitors, HEXIM1-low TNBC are more prone to inhibition by Hsp90 and CDK9 inhibitors. Thus, our studies have suggested different treatment options for highly malignant breast cancer with different mutations in the P-TEFb pathway.

Previously, it has been reported that TNBCs are particularly sensitive to inhibition of Hsp90. In addition, PU-H71, another Hsp90 inhibitor that has entered Phase I clinical trial, was shown to be more active in the TNBC than non-TNBC models (Caldas-Lopes *et al.*, 2009). However, the mechanism for this heightened sensitivity has not been defined clearly. Hsp90 is known to affect the activities of many client oncogenic proteins, including PI3K/Akt, JAK/STAT, RAS/ERK, NF-κB, and CDKs, that are involved in various key signaling pathways (Sidera and Patsavoudi, 2014). Thus, the inhibition of Hsp90 could affect tumor proliferation and apoptosis through these pathways. However, these pathways are not unique to TNBC and thus cannot fully explain why TNBC is particularly sensitive to Hsp90 inhibition. Our study here has suggested that the reduced HEXIM1 levels in TNBC and its impact on CDK9 processing and regulation may underlie this sensitivity. We showed that HEXIM1 is down-regulated in TNBC and that this down-regulation results in accumulation of CDK9 in the Hsp90 complex and a significant decrease in the known P-TEFb complexes (SEC and 7SK snRNP) in cells. Hsp90 inhibitors block maturation of CDK9 by disrupting the CDK9–CycT1–Hsp90 complex and thus produce high levels of immature and unprotected CDK9 that are quickly degraded, leading to the depletion of the critically needed P-TEFb in cells, resulting in cell death. Our study has thus provided a mechanistic link between the generally low HEXIM1 levels in TNBC and the heightened sensitivity of these cells to Hsp90 inhibitors. More importantly, combinatory treatment with both Hsp90 and CDK9 inhibitors show higher efficiency of suppression of TNBC. Thus, our study has revealed a potentially novel and promising therapy for TNBC using the combination of CDK9 with Hsp90 inhibitors. [AQ 4]

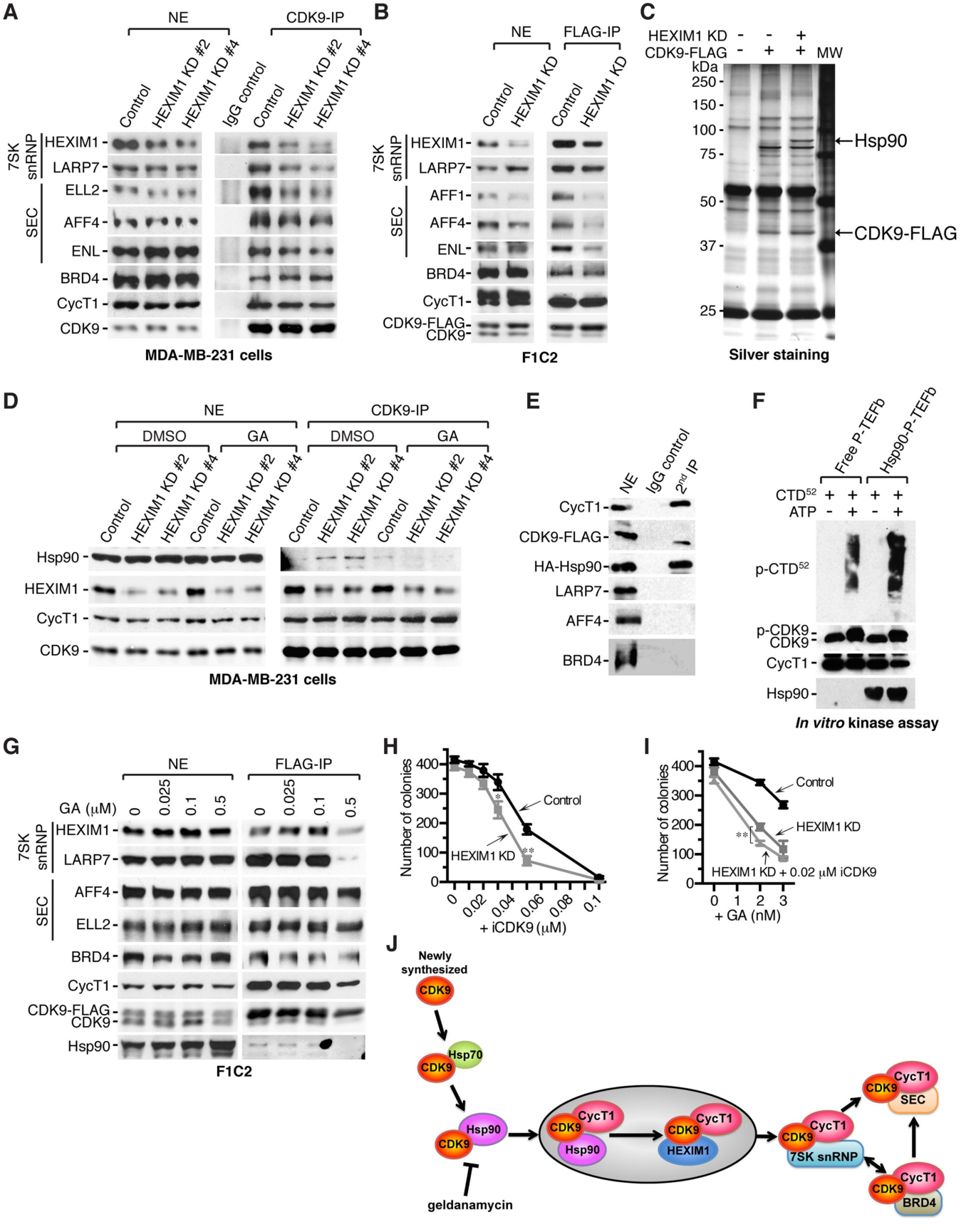
A
NE
CDK9-IP
Control
HEXIM1 KD #2
HEXIM1 KD #4
IgG control
7SK snRNP
SEC
HEXIM1
LARP7
ELL2
AFF4
ENL
BRD4
CycT1
CDK9
MDA-MB-231 cells
B
NE
FLAG-IP
Control
HEXIM1 KD
AFF1
CDK9-FLAG
F1C2
C
HEXIM1 KD
CDK9-FLAG
MW
kDa
250
150
100
75
50
37
25
Hsp90
CDK9-FLAG
Silver staining
D
DMSO
GA
MDA-MB-231 cells
E
NE
IgG control
2nd IP
HA-Hsp90
F
Free P-TEFb
Hsp90-P-TEFb
CTD52
ATP
p-CTD52
p-CDK9
In vitro kinase assay
G
GA (μM)
0
0.025
0.1
0.5
F1C2
H
Number of colonies
Control
HEXIM1 KD
+ iCDK9 (μM)
I
HEXIM1 KD + 0.02 μM iCDK9
+ GA (nM)
J
Newly synthesized
Hsp70
Hsp90
geldanamycin
7SK snRNP
SEC
BRD4

In addition to its functions in P-TEFb processing and regulation, HEXIM1 has also been reported to play a role in DNA-mediated innate immune response by binding to the NEAT1 long non-coding RNA and forming a multi-subunit RNA-protein complex that includes DNA-PK and other para-speckle factors (Morchikh *et al.*, 2017). It is not clear whether this P-TEFb-independent function of HEXIM1 is related to its role in human cancer, as these HEXIM1-containing RNA–protein complexes are mostly involved in anti-microbial and autoimmune responses and have not been linked to solid human tumors. In contrast, the ability of HEXIM1 to regulate P-TEFb has been implicated in many human cancers, including melanoma (Tan *et al.*, 2016) and breast cancer (Ogba *et al.*, 2010; Ketchart *et al.*, 2011). Thus, the increased sensitivity of TNBC cells to Hsp90 inhibition caused by down-regulation of HEXIM1 is very likely a P-TEFb-dependent process, which also explains the sensitivity of these cells to iCDK9. Because HEXIM1 has also been found to be down-regulated in malignant melanoma (Tan *et al.*, 2016), these tumor cells could also become hypersensitive to inhibitors of Hsp90 and/or CDK9. Indeed, Hsp90 inhibitors have been found to inhibit melanoma proliferation and survival (Yeramian *et al.*, 2016; Calero *et al.*, 2017), enhance immunotherapy (Mbofung *et al.*, 2017), and help overcome the resistance of metastatic melanoma cells to BRAF inhibitors (Paraiso *et al.*, 2012; Smyth *et al.*, 2014). Thus, the HEXIM1-mediated sensitivity to Hsp90 inhibition may be a general phenomenon that can be exploited for the treatment of other metastatic human cancers in addition to TNBC. Our work also implies that the combinatory inhibition of both Hsp90 and CDK9 is a highly effective therapy for treating TNBC and other metastatic tumors.

MATERIALS AND METHODS

Cell lines

The MCF10A mammary epithelial cells were cultured in DMEM-F12 supplemented with 5% horse serum, 20 ng/ml EGF, 10 μg/ml insulin, 0.5 μg/ml hydrocortisone, 100 ng/ml cholera toxin, and 1% penicillin/streptomycin. T47D, BT474, ZR75B, and BT549 cells were maintained in RPMI-1640 media containing 10% FBS. MDA-MB-231, MDA-MB-468, MCF7, and HeLa cells were cultured in DMEM plus 10% FBS. The F1C2 cell line is a HeLa-based cell line stably expressing Flag-tagged CDK9 (Yang *et al.*, 2001).

Antibodies

The antibodies against CDK9, LARP7, HEXIM1 and BRD4 were generated as previously described (Yang *et al.*, 2001, 2005; Yik *et al.*, 2003; He *et al.*, 2008). Anti-AFF1 and ENL antibodies were purchased from Bethyl Laboratories (Montgomery, TX), anti-AFF4 and Hsp90 antibodies from Abcam (Cambridge, UK), CycT1 antibody from Santa Cruz Biotechnology, α6-integrin antibody from Zymed, anti-tubulin from Calbiochem (San Diego, CA), and anti-Flag (M2) from Sigma-Aldrich (St. Louis, MO). Horseradish peroxidase (HRP)–conjugated anti-rabbit and anti-mouse antibodies were from Jackson ImmunoResearch Laboratories and Alexa 488-conjugated anti-rat antibody was from Invitrogen.

Transfection and infection

shRNA targeting human HEXIM1 (sequence: 5′-AAACAGAGCCTTCGAGCTTC-3′) or an shRNA-resistant human HEXIM1-HA (sequence: 5′-AAACAGAGCTTGAGAGCTTC-3′) was introduced into breast cancer cell lines by retroviral infection as described previously (Zhu *et al.*, 2007). Briefly, shHEXIM1 in pSUPER.retro.puro vector or HEXIM1-HA in pBabe.puro vector was transfected together with retroviral packaging vectors into 293T cells, and viral supernatant was used to infect the breast cancer cells. Single colonies of infected cells were selected in the presence of puromycin and analyzed.

Quantitative RT-PCR (qRT-PCR)

qRT-PCR was performed with ABI 7300 (Applied Biosystem) and a DyNAmo HS SYBR Green qPCR kit (Fisher Scientific) according to the manufacturers' instructions. The gene-specific primers used in qRT-PCR are HEXIM1, forward 5′-CCAGCCTCAAACTAGCAACTG-3′ and reverse 5′-CGCTCTCGATTGCCACCTAC-3′; GAPDH, forward 5-AGCCACATCGCTCAGACAC-3′ and reverse 5′-GCCCAATACGACCAAATCC-3′. All PCR reactions were performed in triplicates.

Immunoprecipitation and Western blotting

Nuclear extracts (NEs) were prepared from cultured cells, and immunoprecipitation and Western blotting were performed as previously described (Lu *et al.*, 2014). Briefly, NEs were incubated with specific antibodies coupled to protein A beads at 4°C for from 2 h to overnight. After being washed with buffer D (20 mM HEPES-KOH, pH 7.9, 15% glycerol, 0.2 mM EDTA, 0.1% NP-40, 1 mM DTT, and 0.5 mM PMSF) containing 0.3 M KCl, the proteins of interest

FIGURE 5: HEXIM1 is required for the assembly of P-TEFb into the 7SK snRNP. (A, B) Nuclear extracts (NE) were prepared from control or HEXIM1 KD MDA-MB-231, A, or F1C2, B, cells and subjected to immunoprecipitation with anti-CDK9 antibodies. The 7SK snRNP, SEC, and BRD4 associations were examined by Western blotting. (C) CDK9 was isolated from control or HEXIM1 KD F1C2 cells with anti-FLAG, and CDK9-associated proteins were visualized by silver staining. (D) Control or HEXIM1 KD MDA-MB-231 cells were treated with 0.05 μM GA for 24 h. Binding of CDK9 to Hsp90 and HEXIM1 was analyzed by immunoprecipitation with anti-CDK9 followed by Western blotting. (E) CDK9, CycT1, and Hsp90 exist in the same complex. F1C2 HEXIM1 KD cells expressing HA-Hsp90 were subjected to sequential immunoprecipitation: first with anti-FLAG antibody (for CDK9-FLAG) and then with anti-HA. CycT1 that associates with both CDK9 and Hsp90 was detected by Western blotting. (F) In vitro kinase assays. The free P-TEFb was isolated from the F1C2 nuclear extract by immunoprecipitation with anti-FLAG under the high-salt condition (1 M KCl + 1% NP-40). The Hsp90-associated P-TEFb was isolated with anti-HA-Hsp90 from HEXIM1 KD F1C2 cells. The CDK9 levels in the two complexes were normalized before the complexes were subjected to an in vitro kinase assay. p-CTD[52], phospho-CDK9 (p-CDK9), CDK9, CycT1, and Hsp90 were detected by Western blotting. (G) F1C2 cells were treated for 24 h with varying concentrations of GA as indicated. CDK9 was isolated from NE by immunoprecipitation with anti-FLAG, and CDK9-associated proteins were detected by Western blotting with the indicated antibodies for the 7SK snRNP, SEC, and BRD4 complexes. (H, I) Clonogenic growth of breast cancer cells was inhibited by iCDK9 treatment either alone, H, or together with GA, I. Data are presented as means ± SD in triplicates. *$p < 0.05$, **$p < 0.01$, Student's *t* test. (J) A model of HEXIM1 function in P-TEFb maturation and processing. CDK9–CycT1–Hsp90 and CDK9–CycT1–HEXIM1 complexes are necessary intermediates that allow transfer of CDK9 from Hsp90 to the 7SK snRNP.

were eluted with 0.1 M glycine (pH 2.0) and analyzed by Western blotting with the indicated antibodies.

In vitro kinase assay

The P-TEFb complexes were isolated by immunoprecipitation, and the immune complex immobilized on antibody beads was incubated with 100 ng GST-CTD[52] at 30°C for 30 min in a 25-μl reaction buffer containing 10 mM $MgCl_2$, 50 mM NaCl, 50 mM HEPES pH 7.4, 1 mM DTT, and ±50 μM ATP. The kinase reaction was stopped by the addition of 10 μl of 4× SDS loading buffer and boiled at 95°C for 10 min.

Three-dimensional culture

Culture of mammary epithelial cells in the 3D laminin-rich extracellular matrix (Matrigel) was done as described previously (He *et al.*, 2008). Briefly, cells were seeded in growth factor–reduced Matrigel (BD Biosciences) in the wells in an eight-well chamber slide and fed every 4 days. Drug treatment was performed at day 4. Cells were fixed on day 7 and stained for α6-integrin as a basal–lateral marker. Microscopy was performed on a Zeiss LSM710 confocal microscope at the Berkeley Biological Imaging Facility.

Wound healing assay and cell migration

Cells were cultured in 12-well plates to confluence. A plastic tip was used to generate a wound across the cell monolayer. The wound closure was measured after 24 h. Migration assays were performed in Transwell chambers (Corning). In medium containing 1% FBS, 1×10^5 cells were seeded onto membranes in top chambers and allowed to migrate toward the bottom chambers filled with medium containing 10% FBS. Migrated cells were stained with 0.1% crystal violet in methanol.

The soft agar assay

Five thousand cells were suspended in 1.2 ml medium containing 0.375% Bacto Agar (BD) and overlaid on the hardened bottom layer containing 0.66% agar in a well of a six-well plate. Fresh medium (1.2 ml) containing 0.375% agar was added to each well once a week for 3 wk. The colonies were visualized by staining with 0.5 mg/ml 3-(4,5-dimethylthiazol-2-yl)-2,5-diphenyl tetrazolium bromide (MTT) (Sigma) for 4 h at 37°C.

Proliferation, colony formation, and survival assays

Thirty thousand cells were seeded in triplicate in six-well plates for 24 h and treated with drugs or DMSO at varying concentrations. Proliferation of cells were scored by cell counting at day 3–5 and normalized to the control DMSO-treated group. For colony formation assay, 1×10^3 cells were seeded in a well in 6-well plates in triplicates for 24 h and treated with drugs. Cell colonies were fixed with 4% paraformaldehyde for 10 min and stained with 0.1% crystal violet for 15 min at room temperature. To evaluate apoptosis or cell survival, 1×10^6 cells were seeded in a well of six-well plates and then treated with 0.05 μM GA for an additional 48 h. Cells were stained with 50 μg/ml propidium iodide (BD, Cat# 550825) and analyzed by flow cytometry.

In vivo xenograft assay

Female nude mice (6 wks old) were obtained from Jackson Lab. MDA-MB-231 control and HEXIM1 KD cells (2×10^6 cells) were injected subcutaneously to induce tumor formation. Tumor growth was monitored by measurement of tumor diameters with a caliper, and the tumor volume was calculated using the following formula: volume = $0.52 \times (\text{length} \times \text{width}^2)$. After tumors reached a measurable size (~100 mm^3), GA (20 mg/kg) was injected intraperitoneally twice per week for three additional weeks. The solid tumors were then removed and weighed.

Histology and TUNEL assay

Tumors were fixed in 4% formalin and paraffin embedded. The embedded tissues were sectioned and stained with hematoxylin and eosin (H&E) according to a standard protocol using Shandon Gemini Varistain ES Automated Slide Stainer (Thermo Fisher Scientific). The tumor sections were subjected to the TUNEL assay using the TUNEL immunofluorescence kit (Promega) according to the manufacturer's instructions. The level of apoptosis was quantified by comparing the number of apoptotic cells to that of the total cells.

Immunohistochemistry

Immunohistochemistry was performed on a breast cancer tissue array (BR1503b, US Biomax) using the Tyramide Signal Amplification Biotin System Kit (NEL700A001KT, Akoya Biosciences) with anti-HEXIM1 antibodies (1:200, ab245494, abcam), following the manufacturer's instructions. Images were captured using the Zeiss AxioImager M1 microscope, and the relative signal intensity was quantified by ImageJ software. The average intensity per pixel was measured on each image of the stained slide.

Database analysis

We examined the expression profile of HEXIM1 in two human cancer datasets from the Cancer Genome Atlas (TCGA) (https://cancergenome.nih.gov) and Oncomine (www.oncomine.org), using the threshold search criteria as previously described (Ji *et al.*, 2014). The Mann–Whitney test was used to evaluate the significance of differences in HEXIM1 expression between the cancer and normal control groups.

Statistical analysis

Data are presented as mean values from at least three biological replicates, with error bars denoting standard deviations. Comparisons between two groups were analyzed using the two-tailed Student's *t* test. The significance level was set at *p* values $*p < 0.05$, $**p < 0.01$, $***p < 0.001$. Statistical analyses were conducted using ImageJ and the Graphpad Prism software.

ACKNOWLEDGMENTS

This study is supported by DOD/U.S. Army Medical Research and Materiel Command W81XWH-15-1-0068 to K.L. and Qiang Z. and NIH/NIAID R01 AI041757 to Qiang Z. We thank Kartoosh Heydari and the Flow Cytometry Facility at UC Berkeley for technical assistance. We thank Steve Ruzin and Denise Schichnes at the CNR biological imaging facility at UC Berkeley for operation of microscopy and assistance with IHC experiments. We also thank Armann Andaya from the Campus Mass Spectrometry Facilities at UC Davis for assistance with mass spectrometry protein identification.

REFERENCES

Andrieu G, Tran AH, Strissel KJ, Denis GV (2016). BRD4 regulates breast cancer dissemination through Jagged1/Notch1 signaling. Cancer Res 76, 6555–6567.

Beliakoff J, Bagatell R, Paine-Murrieta G, Taylor CW, Lykkesfeldt AE, Whitesell L (2003). Hormone-refractory breast cancer remains sensitive to the antitumor activity of heat shock protein 90 inhibitors. Clin Cancer Res 9, 4961–4971.

Blobel GA, Kalota A, Sanchez PV, Carroll M (2011). Short hairpin RNA screen reveals bromodomain proteins as novel targets in acute myeloid leukemia. Cancer Cell 20, 287–288.

Caldas-Lopes E, Cerchietti L, Ahn JH, Clement CC, Robles AI, Rodina A, Moulick K, Taldone T, Gozman A, Guo Y, *et al.* (2009). Hsp90 inhibitor PU-H71, a multimodal inhibitor of malignancy, induces complete responses in triple-negative breast cancer models. Proc Natl Acad Sci USA 106, 8368–8373.

Calero R, Morchon E, Martinez-Argudo I, Serrano R (2017). Synergistic antitumor effect of 17AAG with the PI3K/mTOR inhibitor NVP-BEZ235 on human melanoma. Cancer Lett 406, 1–11.

Dawson MA, Prinjha RK, Dittmann A, Giotopoulos G, Bantscheff M, Chan WI, Robson SC, Chung CW, Hopf C, Savitski MM, *et al.* (2011). Inhibition of BET recruitment to chromatin as an effective treatment for MLL-fusion leukaemia. Nature 478, 529–533.

He N, Jahchan NS, Hong E, Li Q, Bayfield MA, Maraia RJ, Luo K, Zhou Q (2008). A La-related protein modulates 7SK snRNP integrity to suppress P-TEFb-dependent transcriptional elongation and tumorigenesis. Mol Cell 29, 588–599.

He N, Liu M, Hsu J, Xue Y, Chou S, Burlingame A, Krogan NJ, Alber T, Zhou Q (2010). HIV-1 Tat and host AFF4 recruit two transcription elongation factors into a bifunctional complex for coordinated activation of HIV-1 transcription. Mol Cell 38, 428–438.

Jang MK, Mochizuki K, Zhou M, Jeong HS, Brady JN, Ozato K (2005). The bromodomain protein Brd4 is a positive regulatory component of P-TEFb and stimulates RNA polymerase II-dependent transcription. Mol Cell 19, 523–534.

Jeronimo C, Forget D, Bouchard A, Li Q, Chua G, Poitras C, Therien C, Bergeron D, Bourassa S, Greenblatt J, *et al.* (2007). Systematic analysis of the protein interaction network for the human transcription machinery reveals the identity of the 7SK capping enzyme. Mol Cell 27, 262–274.

Ji X, Lu H, Zhou Q, Luo K (2014). LARP7 suppresses P-TEFb activity to inhibit breast cancer progression and metastasis. Elife 3, e02907.

Ketchart W, Ogba N, Kresak A, Albert JM, Pink JJ, Montano MM (2011). HEXIM1 is a critical determinant of the response to tamoxifen. Oncogene 30, 3563–3569.

Ketchart W, Smith KM, Krupka T, Wittmann BM, Hu Y, Rayman PA, Doughman YQ, Albert JM, Bai X, Finke JH, *et al.* (2013). Inhibition of metastasis by HEXIM1 through effects on cell invasion and angiogenesis. Oncogene 32, 3829–3839.

Krueger BJ, Jeronimo C, Roy BB, Bouchard A, Barrandon C, Byers SA, Searcey CE, Cooper JJ, Bensaude O, Cohen EA, *et al.* (2008). LARP7 is a stable component of the 7SK snRNP while P-TEFb, HEXIM1 and hnRNP A1 are reversibly associated. Nucleic Acids Res 36, 2219–2229.

Lin C, Smith ER, Takahashi H, Lai KC, Martin-Brown S, Florens L, Washburn MP, Conaway JW, Conaway RC, Shilatifard A (2010). AFF4, a component of the ELL/P-TEFb elongation complex and a shared subunit of MLL chimeras, can link transcription elongation to leukemia. Mol Cell 37, 429–437.

Lu H, Li Z, Xue Y, Schulze-Gahmen U, Johnson JR, Krogan NJ, Alber T, Zhou Q (2014). AFF1 is a ubiquitous P-TEFb partner to enable Tat extraction of P-TEFb from 7SK snRNP and formation of SECs for HIV transactivation. Proc Natl Acad Sci USA 111, E15–E24.

Lu H, Xue Y, Yu GK, Arias C, Lin J, Fong S, Faure M, Weisburd B, Ji X, Mercier A, *et al.* (2015). Compensatory induction of MYC expression by sustained CDK9 inhibition via a BRD4-dependent mechanism. Elife 4, e06535.

Mbofung RM, McKenzie JA, Malu S, Zhang M, Peng W, Liu C, Kuiatse I, Tieu T, Williams L, Devi S, *et al.* (2017). HSP90 inhibition enhances cancer immunotherapy by upregulating interferon response genes. Nat Commun 8, 451.

Michels AA, Fraldi A, Li Q, Adamson TE, Bonnet F, Nguyen VT, Sedore SC, Price JP, Price DH, Lania L, *et al.* (2004). Binding of the 7SK snRNA turns the HEXIM1 protein into a P-TEFb (CDK9/cyclin T) inhibitor. EMBO J 23, 2608–2619.

Morchikh M, Cribier A, Raffel R, Amraoui S, Cau J, Severac D, Dubois E, Schwartz O, Bennasser Y, Benkirane M (2017). HEXIM1 and NEAT1 long non-coding RNA form a multi-subunit complex that regulates DNA-mediated innate immune response. Mol Cell 67, 387–399.e385.

Mori Y, Sato F, Selaru FM, Olaru A, Perry K, Kimos MC, Tamura G, Matsubara N, Wang S, Xu Y, *et al.* (2002). Instabilotyping reveals unique mutational spectra in microsatellite-unstable gastric cancers. Cancer Res 62, 3641–3645.

Mueller D, Garcia-Cuellar MP, Bach C, Buhl S, Maethner E, Slany RK (2009). Misguided transcriptional elongation causes mixed lineage leukemia. PLoS Biol 7, e1000249.

O'Keeffe B, Fong Y, Chen D, Zhou S, Zhou Q (2000). Requirement for a kinase-specific chaperone pathway in the production of a Cdk9/cyclin T1 heterodimer responsible for P-TEFb-mediated tat stimulation of HIV-1 transcription. J Biol Chem 275, 279–287.

Ogba N, Doughman YQ, Chaplin LJ, Hu Y, Gargesha M, Watanabe M, Montano MM (2010). HEXIM1 modulates vascular endothelial growth factor expression and function in breast epithelial cells and mammary gland. Oncogene 29, 3639–3649.

Ott M, Geyer M, Zhou Q (2011). The control of HIV transcription: keeping RNA polymerase II on track. Cell Host Microbe 10, 426–435.

Ouchida R, Kusuhara M, Shimizu N, Hisada T, Makino Y, Morimoto C, Handa H, Ohsuzu F, Tanaka H (2003). Suppression of NF-kappaB-dependent gene expression by a hexamethylene bisacetamide-inducible protein HEXIM1 in human vascular smooth muscle cells. Genes Cells 8, 95–107.

Paraiso KH, Haarberg HE, Wood E, Rebecca VW, Chen YA, Xiang Y, Ribas A, Lo RS, Weber JS, Sondak VK, *et al.* (2012). The HSP90 inhibitor XL888 overcomes BRAF inhibitor resistance mediated through diverse mechanisms. Clin Cancer Res 18, 2502–2514.

Ren C, Zhang G, Han F, Fu S, Cao Y, Zhang F, Zhang Q, Meslamani J, Xu Y, Ji D, *et al.* (2018). Spatially constrained tandem bromodomain inhibition bolsters sustained repression of BRD4 transcriptional activity for TNBC cell growth. Proc Natl Acad Sci USA 115, 7949–7954.

Shi J, Wang Y, Zeng L, Wu Y, Deng J, Zhang Q, Lin Y, Li J, Kang T, Tao M, *et al.* (2014). Disrupting the interaction of BRD4 with diacetylated Twist suppresses tumorigenesis in basal-like breast cancer. Cancer Cell 25, 210–225.

Sidera K, Patsavoudi E (2014). HSP90 inhibitors: current development and potential in cancer therapy. Recent Pat Anticancer Drug Discov 9, 1–20.

Smyth T, Paraiso KHT, Hearn K, Rodriguez-Lopez AM, Munck JM, Haarberg HE, Sondak VK, Thompson NT, Azab M, Lyons JF, *et al.* (2014). Inhibition of HSP90 by AT13387 delays the emergence of resistance to BRAF inhibitors and overcomes resistance to dual BRAF and MEK inhibition in melanoma models. Mol Cancer Ther 13, 2793–2804.

Sobhian B, Laguette N, Yatim A, Nakamura M, Levy Y, Kiernan R, Benkirane M (2010). HIV-1 Tat assembles a multifunctional transcription elongation complex and stably associates with the 7SK snRNP. Mol Cell 38, 439–451.

Solit DB, Osman I, Polsky D, Panageas KS, Daud A, Goydos JS, Teitcher J, Wolchok JD, Germino FJ, Krown SE, *et al.* (2008). Phase II trial of 17-allylamino-17-demethoxygeldanamycin in patients with metastatic melanoma. Clin Cancer Res 14, 8302–8307.

Suzuki Y, Kondo Y, Hara S, Kimata R, Nishimura T (2010). Effect of the hsp90 inhibitor geldanamycin on androgen response of prostate cancer under hypoxic conditions. Int J Urol 17, 281–285.

Tan JL, Fogley RD, Flynn RA, Ablain J, Yang S, Saint-Andre V, Fan ZP, Do BT, Laga AC, Fujinaga K, *et al.* (2016). Stress from nucleotide depletion activates the transcriptional regulator HEXIM1 to suppress melanoma. Mol Cell 62, 34–46.

Wedeh G, Cerny-Reiterer S, Eisenwort G, Herrmann H, Blatt K, Hadzijusufovic E, Sadovnik I, Mullauer L, Schwaab J, Hoffmann T, *et al.* (2015). Identification of bromodomain-containing protein-4 as a novel marker and epigenetic target in mast cell leukemia. Leukemia 29, 2230–2237.

Whitesell L, Lindquist SL (2005). HSP90 and the chaperoning of cancer. Nat Rev Cancer 5, 761–772.

Winter GE, Rix U, Carlson SM, Gleixner KV, Grebien F, Gridling M, Muller AC, Breitwieser FP, Bilban M, Colinge J, *et al.* (2012). Systems-pharmacology dissection of a drug synergy in imatinib-resistant CML. Nat Chem Biol 8, 905–912.

Wittmann BM, Wang N, Montano MM (2003). Identification of a novel inhibitor of breast cell growth that is down-regulated by estrogens and decreased in breast tumors. Cancer Res 63, 5151–5158.

Xue Y, Yang Z, Chen R, Zhou Q (2010). A capping-independent function of MePCE in stabilizing 7SK snRNA and facilitating the assembly of 7SK snRNP. Nucleic Acids Res 38, 360–369.

Yang Z, Yik JH, Chen R, He N, Jang MK, Ozato K, Zhou Q (2005). Recruitment of P-TEFb for stimulation of transcriptional elongation by the bromodomain protein Brd4. Mol Cell 19, 535–545.

Yang Z, Zhu Q, Luo K, Zhou Q (2001). The 7SK small nuclear RNA inhibits the CDK9/cyclin T1 kinase to control transcription. Nature 414, 317–322.

Yeramian A, Vea A, Benitez S, Ribera J, Domingo M, Santacana M, Martinez M, Maiques O, Valls J, Dolcet X, *et al.* (2016). 2-phenylethynesulphonamide (PFT-mu) enhances the anticancer effect of the novel hsp90 inhibitor NVP-AUY922 in melanoma, by reducing GSH levels. Pigment Cell Melanoma Res 29, 352–371.

Yik JH, Chen R, Nishimura R, Jennings JL, Link AJ, Zhou Q (2003). Inhibition of P-TEFb (CDK9/Cyclin T) kinase and RNA polymerase II transcription by the coordinated actions of HEXIM1 and 7SK snRNA. Mol Cell 12, 971–982.

Yokoyama A, Lin M, Naresh A, Kitabayashi I, Cleary ML (2010). A higher-order complex containing AF4 and ENL family proteins with P-TEFb facilitates oncogenic and physiologic MLL-dependent transcription. Cancer Cell 17, 198–212.

Zhou Q, Li T, Price DH (2012). RNA polymerase II elongation control. Annu Rev Biochem 81, 119–143.

Zhou Q, Yik JH (2006). The yin and yang of P-TEFb regulation: implications for human immunodeficiency virus gene expression and global control of cell growth and differentiation. Microbiol Mol Biol Rev 70, 646–659.

Zhu Q, Krakowski AR, Dunham EE, Wang L, Bandyopadhyay A, Berdeaux R, Martin GS, Sun L, Luo K (2007). Dual role of SnoN in mammalian tumorigenesis. Mol Cell Biol 27, 324–339.

Zuber J, Shi J, Wang E, Rappaport AR, Herrmann H, Sison EA, Magoon D, Qi J, Blatt K, Wunderlich M, *et al.* (2011). RNAi screen identifies Brd4 as a therapeutic target in acute myeloid leukaemia. Nature 478, 524–528.

ETOC:

HEXIM1 is often down-regulated in human triple-negative breast cancer (TNBC), and these cancer cells are highly sensitive to Hsp90 inhibitors. However, the mechanistic link between the two has not been determined. Our study provides a mechanistic explanation for the increased sensitivity of TNBC to Hsp90 inhibition.

Author Queries

[AQ 1]: Please provide list of abbreviations used along with their definitions.
[AQ 2]: Please provide omitted letters/symbols represented by square boxes.
[AQ 3]: The other two drugs are called by generic names; should Taxol be referred to as paclitaxel for consistency?
[AQ 4]: Please insert appropriate letter or symbol.